2016

Dynamic Model and Adaptive Control of a Transcritical Organic Rankine Cycle

Samiuddin, Jilan

UNIVERSITY OF CALGARY

Dynamic Model and Adaptive Control of a Transcritical Organic Rankine Cycle

by

Jilan Samiuddin

A THESIS

SUBMITTED TO THE FACULTY OF GRADUATE STUDIES

IN PARTIAL FULFILLMENT OF THE REQUIREMENTS FOR THE

DEGREE OF MASTER OF SCIENCE

GRADUATE PROGRAM IN ELECTRICAL ENGINEERING

CALGARY, ALBERTA

SEPTEMBER, 2016

Abstract

The Transcritical Organic Rankine Cycle (TORC) is a non-linear time-varying heat recovery system for small-scale power generation. It is similar to a boiler-turbine system but uses organic fluid as the primary heat carrier instead of H_2O and works in both subcritical and supercritical regions. The heat source can be either renewable energy or industrial waste-heat. In order for the TORC to work efficiently, it is essential the control system tracks the set points as closely as possible while remaining robust to disturbances; the control system design treats the heat source as a time-varying disturbance. To achieve this goal, this thesis presents a design of an adaptive Cerebellar Model Articulation Controller (CMAC) which uses a single-input-single-output strategy by pairing the controlled variables (CVs) to the manipulated variables (MVs) using Relative Gain Array (RGA) analysis of the system. The CMAC improves performance and robustness compared to a traditional PI control.

Acknowledgements

First and above all, I praise and thank The Almighty Allah for blessing me with the opportunity and granting me the capability to advance in my journey of life successfully. Several people need to be acknowledged for their help and encouragement throughout my journey preparing for this thesis, and I sincerely apologize for any negligence while I will try my best to give them their dues.

I would like to express my sincere gratitude to my supervisor Dr. Chris J.B. Macnab for his patience, support, advice and guidance from the very beginning of this research. Above all and most needed, he provided an excellent and a friendly environment to work in which was an essential for me for my success. I am also very thankful to my co-supervisor Dr. Jeff Pieper for providing constant support and feedback throughout the research. At the same time, I am thankful to my colleagues, Babak Badkoubeh, Mahsa Sadeghassadi and Rachael L'Orsa, for providing a friendly and pleasant working atmosphere in the office during the last two years period. Many thanks to Genalta Power Inc. for financing this thesis and providing support to their best of capabilities.

I wish to express my gratitude towards my family who has been a constant source of support and care, mainly my mother, without whom it would have been very difficult to pursue such higher education. Overwhelming love from my family has always been a source of inspiration for me in my journey to the completion of my thesis. Last but not the least, I am grateful to my friends, mainly Abiola Adebayo, Ismail Kamal and Munif Sakib, for making my stay in Canada for the last two years away from home a fantastic experience.

Table of Contents

Abstract ii

Acknowledgements iii

Table of Contents iv

List of Figures vii

List of Tables ix

List of Symbols, Abbreviations and Nomenclature x

1 Introduction **1**

1.1 Background 1

1.2 Applications 2

1.3 System description 3

1.4 Modelling of ORC systems 5

1.5 Working fluid selection and performance analysis 9

1.6 Control design for ORC 16

1.7 Cerebellar Model Articulation Controller (CMAC) 17

1.8 Thesis contribution 20

1.9 Summary 20

2 Modelling **22**

2.1 Modelling 22

2.2 Thermodynamic properties and CoolProp 23

2.3 Structure of the heat exchangers 24

2.4 Some important terminology for ORC modelling . . . 26
2.4.1 Average Void Fraction ($\overline{\gamma}$) . . . 26
2.4.2 Heat Transfer Coefficient (α) . . . 28
2.4.2.1 Single-phase flow for the inner tube . . . 28
2.4.2.2 Two-phase flow for the inner tube . . . 29
2.4.2.3 Single-phase flow for the outer tube . . . 29
2.4.2.4 Heat-transfer coefficient of air in the condenser . . . 30
2.5 Slow dynamics components . . . 31
2.5.1 Condenser . . . 31
2.5.1.1 Superheated region . . . 34
2.5.1.2 Two-phase region . . . 36
2.5.1.3 Sub-cooled region . . . 38
2.5.2 Evaporator . . . 43
2.5.3 Recuperator . . . 48
2.6 Fast dynamics components . . . 52
2.6.1 Pump . . . 52
2.6.2 Expander . . . 54
2.6.3 Valve . . . 55
2.7 Model validation . . . 56
2.8 Summary . . . 59

3 Control development **60**
3.1 Control Strategy for determining set-points . . . 60
3.2 Relative Gain Array (RGA) analysis . . . 65
3.3 Proportional, Integral, Derivative (PID) control . . . 67
3.3.1 IMC technique for first-order process . . . 68
3.4 Cerebellar Model Articulation Controller (CMAC) . . . 71
3.4.1 CMAC structure and methodology . . . 71

3.4.2 CMAC adaptive control 76
3.4.3 Stability Proof 77
3.5 Summary 80

4 Results **81**

4.1 Disturbance rejection 81
4.2 Set-point tracking 86
4.3 Step-disturbance rejection 90
4.4 Summary 93

5 Conclusion **95**

5.1 Conclusion 95
5.2 Future work 96

List of Figures

1.1 Typical ORC 3

1.2 ORC with the addition of a recuperator 4

1.3 Temperature vs Entropy for SORC and TORC 5

2.1 Cross-view of a concentric annular tube heat exchanger 24

2.2 Side-view of concentric annular tube heat exchanger - parallel flow and counter flow and their temperature profiles 26

2.3 Moving boundary model for condenser 32

2.4 Control volume for each region 33

2.5 Design inputs and outputs for the condenser 42

2.6 Schematic of the evaporator 44

2.7 Design inputs and outputs for the evaporator 47

2.8 Schematic of the recuperator 49

2.9 Design inputs and outputs for the recuperator 52

2.10 Design inputs and outputs for the pump 54

2.11 Design inputs and outputs for the expander 55

2.12 Design inputs and output for the valve 56

2.13 Step change in μ from 0.4 to 0.45 57

2.14 Step change in X_{pp} from 0.4 to 0.45 58

2.15 Step change in N_{fan} from $300rpm$ to $500rpm$ 59

3.1 Changes in $T_{\text{ev,opt}}$ with respect to changes in T_{sf} for a SORC 62

3.2 $\dot{W}_{\text{net}}$ against changes in T_{sf} for TORC 63

3.3 P_{ev} against changes in T_{sf} for TORC 63
3.4 $T_{out,ev}$ against changes in T_{sf} for TORC 64
3.5 $T_{out,c}$ against changes in T_{sf} for TORC 64
3.6 Closed-loop PID control 67
3.7 Closed-loop control response for each pairing 70
3.8 CMAC structure ($Q = 3, m = 3, n = 2$) 71
3.9 CMAC methodology with two input variables 73
3.10 Mapping for CMAC with two-inputs 74
3.11 Basis function operating in hypercube for the first layer 74

4.1 Variation in heat source temperature 82
4.2 Set-point tracking under the influence of disturbance 83
4.3 Variation in MVs under the influence of disturbance 83
4.4 Net power output for disturbance rejection test 84
4.5 RMS error convergence for disturbance rejection test 85
4.6 Behavior of weights in CMAC for disturbance rejection 85
4.7 Change in set-points of the CVs 87
4.8 $T_{out,ev}$ channel zoomed 87
4.9 Variation in MVs for set-point tracking 88
4.10 Net power for set-point tracking 88
4.11 RMS error convergence for set-point tracking test 89
4.12 Behavior of weights in CMAC for the set-point tracking 89
4.13 Step changes in T_{sf} 90
4.14 Set-point tracking under the influence of step disturbance 91
4.15 Variation in MVs under the influence of step disturbance 91
4.16 Net power for step-disturbance rejection 92
4.17 RMS error convergence for step-disturbance rejection test 92
4.18 Behavior of weights in CMAC for the step-disturbance rejection 93

List of Tables

1.1 Thermal efficiency of an ideal recuperated ORC for different working fluids 10

1.2 ASHRAE safety classification 10

1.3 Properties of R134a 15

2.1 Rules for heat exchanger modelling 23

2.2 Design parameters of condenser 43

2.3 Design parameters of evaporator 48

2.4 Design parameters of recuperator 52

2.5 Design parameters of pump 54

3.1 Transfer functions estimated using MATLAB showing relations between the MVs and CVs 65

3.2 Percentage fit to estimation data between MVs and CVs 66

3.3 K_p and K_i for control pairings 70

3.4 Nominal operation condition 77

4.1 RMS error for P_{ev} (Pa) 94

4.2 RMS error for $T_{\text{out,ev}}(^{\text{o}}\text{C})$ 94

4.3 RMS error for $T_{\text{out},c}$ ($^{\text{o}}$C) 94

4.4 Net energy (MJ) comparison between adaptive CMAC and PI controller 94

List of Symbols, Abbreviations and Nomenclature

Symbol	Description
ξ	Inverse of the slope of a temperature-entropy diagram
T	Temperature (K)
P or p	Pressure (Pa)
A	Cross sectional area (m^2)
r_i	Internal radius of internal pipe (m)
r_o	External radius of internal pipe (m)
R_i	Internal radius of external pipe (m)
$\triangle T_m$	Log mean temperature difference
$\bar{\gamma}$	Average void fraction
S	Slip ratio/Channel flow area (m^2)
ρ	Density (kg/m^3)
x	Quality of fluid/States
Re	Reynold's number
$\dot{m}$	Mass flow rate (kg/s)
Pr	Prandtl number
η	Dynamic viscosity $(kg/m.s)$
ξ_m	Moody friction factor
c	Specific heat capacity $(J/kg.K)$
λ	Thermal conductivity $(W/m.K)$/ Eigenvalue
Nu	Nusselt number
α	Heat transfer coefficient $(W/m^2.K)$
l	Hydraulic mean diameter (m)

St	Stanton number
d or D	Diameter (m)
v	Mean velocity (m/s)
L or z_l	Length (m)
z	Error vector
h	Specific enthalpy (J/kg)
s	Specific entropy $(J/kg.K)$
q	Heat flux per unit area/length $(W/m^2$ or $W/m)$
V	Volume (m^3)
t	Time (s)
$\dot{Q}$	Heat transferred (J/s)
X_{pp}	Capacity fraction of pump
$\dot{V}$	Volumetric flow rate (m^3/s)
η_{pump}	Pump efficient coefficient
$\dot{W}$	Work/ Power (J/s)
ε	Isentropic effectiveness of expander
μ	Opening of valve
β_v	Coefficient of valve
N	Rotation speed (rpm)
$\dot{I}$	Irreversibility rate (J/s)
Λ	RGA Matrix
K	Gain
e	Error
λ_f	Filter coefficient
τ_p	Process time constant (s)
k_p	Process gain
Γ	CMAC activation function output

w, w	Weight, weight vector
z	Error vector
ν	Adaptive constant
u	Control input
V	Lyapunov function
Subscript	
c	cold side/condenser
ev	evaporator
r	recuperator
h	hot side
out	outlet
in	inlet
i	inner/cell number
o	outer
crit	critical parameter
wf	working fluid
w	wall
s	surface
A	position
B	position
g	saturated vapor
l	saturated liquid
int1	interface between superheated region and two-phase region
int2	interface between two-phase region and sub-cooled region

Chapter 1

Introduction

1.1 Background

In recent decades, with technological advancements followed by great demand of energy, global energy consumption has increased significantly [5][78]. Environmental constraints and pollution from the use of fossil fuels have brought forward a number of concerns among which global warming is a major one. Moreover, fossil fuels will eventually be depleted [3]. To try and solve these problems researchers are looking at both exploiting renewable energy sources and increasing energy efficiency. Organic Rankine Cycle (ORC) systems transform heat into electricity with much lower input temperatures than traditional boiler-turbine systems, and thus can be applied to both these problems. Renewable systems like solar plants, geothermal sources, and biomass produce heat that is typically not hot enough to drive H_2O-based boiler-turbine systems. In industrial plants, ORCs can be utilized to create electricity from the relatively low-temperature waste heat, increasing the overall efficiency of the plant. Researchers have become interested in ORC technology in recent decades as this technology opens an alternative door for industry to produce clean and environmental friendly power. Successful implementations of technologies like ORC can lead the world to a largely carbon-free economy with its associated benefits.

1.2 Applications

Among many possible ORC applications, waste heat recovery (WHR) seems to have the most potential. According to United States Department of Energy, energy losses in industrial processes can be anywhere between 20-50%, including both waste heat and other means [38]. ORC is an ideal technology suitable for recovering some of the energy from waste heat or exhaust heat, and producing clean usable energy. WHR using ORC is growing within industry due to escalating demands to reduce energy consumption, operational costs and carbon emissions.

Another major application of ORC is heat recovery from geothermal sources. Geothermal heat sources can range from as low as 50^{o}C to as high as 200^{o}C or even more [46]. Although high temperature geothermal sources can be integrated with steam generators, however, low temperature geothermal sources (especially in the range of $50-100^{o}$C) are definitely insufficient for steam generators. According to the Canadian Geothermal Energy Association, the technical generation potential for geothermal sources in Alberta varies from 4,200MW to 250,000MW where the lowest bound corresponds to a 5% recovery at 2500m depth and the highest bound corresponds to a 20% recovery at 5500m depth [1]. Currently very little is being done to extract this potential. Biomass heat recovery is another application of ORC technology and has become one of the most commonly used renewable sources of energy. According to Natural Resources Canada, biomass contributes 1.4% to Canada's electricity generation with a total installed capacity of 2,043 MW (at the end of 2014) and ranks 5th highest in the world in terms of world biofuels production [23]. With its large landmass and active forest and agricultural industries, Canada has access to large and diversified biomass resources. ORC is also an alternative to typical boiler-turbine system for solar parabolic-trough plants. According to Natural Resources Canada, since 2007, there are an estimated $544,000m^2$ of solar collectors operating in Canada producing about 627,000 GJ of energy and displacing 38,000 tonnes of CO_2 annually [24].

1.3 System description

The Rankine Cycle is a model that is used to predict the performance of turbine systems that use H_2O as the working fluid. ORC systems use organic fluids selected for very low boiling points, high molecular weights, and high vapor pressure [107]. A basic ORC has four main components to complete its cycle (Figure 1.1), a pump, an evaporator (boiler unit), an expander (turbine), and a condenser. Adding a recuperator to the typical ORC (Figure 1.2) increases the efficiency of the cycle by extracting some of the heat from the expander outlet to preheat the fluid headed for the evaporator [80][36].

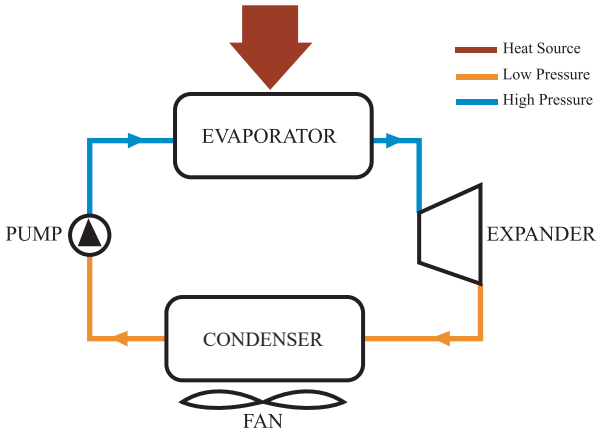

Figure 1.1: Typical ORC

The thermodynamic process involved in the cycle is typically portrayed as a temperature-entropy profile (Figure 1.3) that follows points 1,...,7 sequentially. The liquid working fluid is first pumped to a higher pressure (1-2), which is ideally an isentropic process. It is then preheated in the recuperator (2-3). The following evaporation (3-4) is ideally an isobaric process, and in this thesis will be assumed to occur in the supercritical region rather than the subcritical region (explained in the next paragraph). The mass flow rate of the vaporized fluid is controlled by a valve (4-5). The vapour then enters the expander (5-6), ideally undergoing an isentropic expansion, which gives mechanical energy to the shaft. (Note it is very important to ensure that the working fluid is fully vaporized before it enters the expander, otherwise the liquid-gas mixture of

the working fluid will cause erosion inside the expander eventually causing it to fail). A generator connected to the shaft produces electricity; but the generator is not modelled as part of the ORC system but rather constitutes a load. During the expansion, the working fluid has a drop in pressure. The low pressure exhaust gas coming out from the expander passes through the other side of the recuperator where it is cooled (6-7). The pre-cooled working fluid is then condensed into a liquid state inside the condenser using a fan (7-1), which is ideally an isobaric process. It is important to note that the recuperator is reducing the load on the evaporator and the condenser by mutual heat transfer within the cycle.

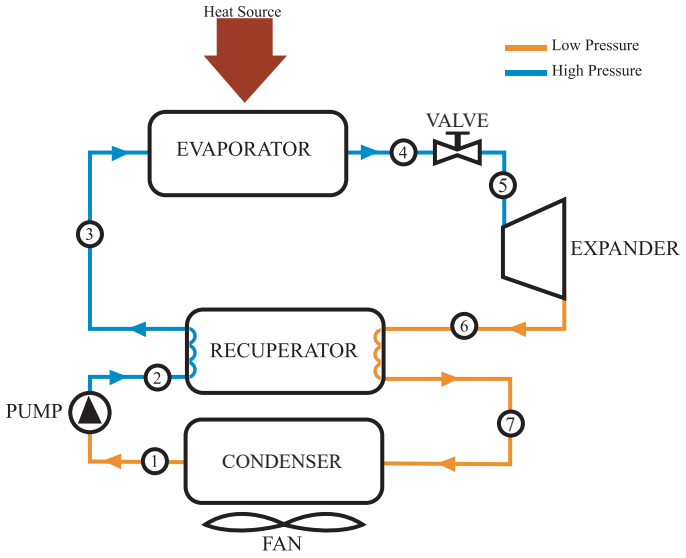

Figure 1.2: ORC with the addition of a recuperator

ORCs can be designed to work in one of two different regions, the subcritical region or the transcritical region which comprises of both subcritical and supercritical regions. A subcritical region is where the working fluid is always below its critical pressure, whereas, in the supercritical region it is above its critical pressure on the evaporation side. An ORC that operates in the supercritical region plus subcritical region is referred to as a transcritical ORC (TORC). Despite the fact that a higher pressure in the system leads to a safety concern and as well as component availability issues [28], TORCs are becoming more popular because of higher work output and as well as higher efficiency due to a higher pressure [82]. The use of organic fluids makes a supercritical design

much easier than in a H_2O-boiler system, since ORCs have a much lower critical pressure and the supercritical operation can be achieved with much less cost in the compression work [43]. For a subcritical ORC (SORC) the upper line during the evaporation process (3-4') is at a lower level compared to that of a TORC. It is the difference between the upper line and the lower line during the condensation process (7-1) that determines how much energy can be extracted by the expander [97]. Since it is not realistic to substantially lower the condensing line using external influences such as atmospheric temperature and pressure [97], the only option left is to push the evaporating line higher - which is achieved using a TORC. However, very few papers in the literatures examine a TORC. Those that have usually focus on either selecting the working fluid [43][45], or on choosing set points through optimization [56][88].

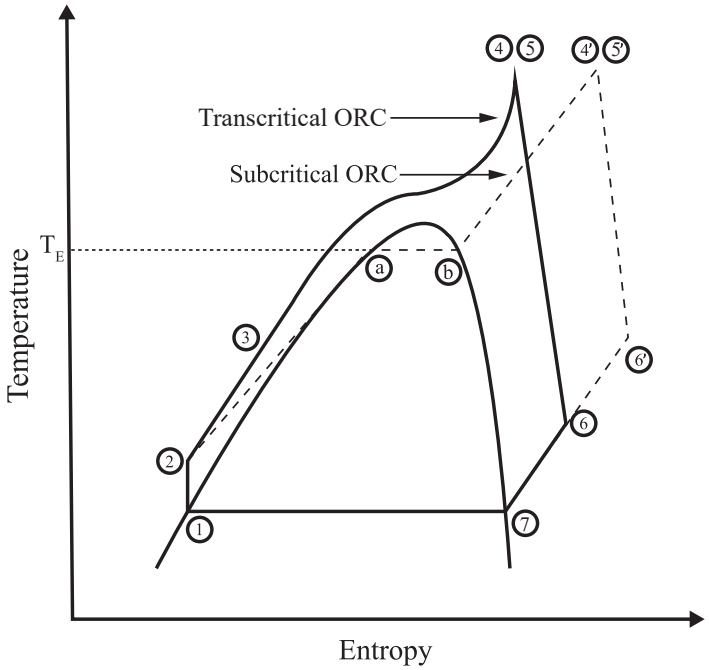

Figure 1.3: Temperature vs Entropy for SORC and TORC

1.4 Modelling of ORC systems

There are several challenges involved in the modelling of an ORC system. Modelling of the heat exchanger introduces the most complexity. Most previous literatures has considered static alge-

braic equations to model the expander, the pump and the valve [81][84][83][102][108]. A lot of work has been done over the past few decades developing heat exchanger models using several techniques, including the moving-boundary (MB) technique, the lumped-parameter (LP) approach, and the finite volume (FV) method (also known as discretization). The appropriate choice depends on the purpose of modelling, the performance requirements, and the working condition of the heat exchangers. (There is one common assumption about all three techniques made in the literature - momentum balance is ignored to keep the models simple and faster [81][80][50][54][74][86]). Bendapudi et al. in [16] concludes that the MB models are approximately three times faster than the FV models, but are less robust to start-up and load-change transients. Desideri et al [35] also conducted experiments in order to compare the performance between the FV and MB techniques and concluded that while both of the techniques are suitable for dynamic modelling of two-phase heat exchangers, the MB technique proved to be much faster compared to the FV technique (they did not investigate the robustness of the two methods). They also suggested using at least 20 nodes for the modelling of a heat exchanger in small-scale ORC applications. However, if the fluid inside the heat exchanger is in the supercritical region the working fluids are not two-phase and MB techniques cannot used [86].

One of the earliest studies on heat exchanger modelling for two-phase fluid flows was conducted by Wedekind et al. [101]. They modelled the two-phase evaporating or condensing flow system as a lumped form by assuming a time-invariant void fraction. They still captured sufficient details of the two-phase region without taking the momentum balance into account. This was a significant contribution that led to developing MB models. Xiang proposed an MB model for the condenser in his vapor compression cycle [50] as a highly useful model for designing control schemes and successfully implemented a model-based state feedback controller (LQG with integrator) for the cycle. Willatzen et al. [104] proposed three-phase MB models and validated their results with experimental data. Jensen in [54] did an intensive study on the MB modelling method. He first proposed a general seventh-order model, but then continued to reduce the model down to a fifth-order, a fourth-order, a third-order and a finally a second-order model. All of these reduced-

order models can capture the essential dynamics, and based on the application of the model the appropriate *n*th order model can be chosen. The reduced order models are very useful for both designing control strategies and optimization as they reduce the mathematical complexities while still capturing the essential dynamics. However, Jensen did not carry out control design nor optimization to validate his point. He also studied discretized models; however, chattering has been identified as a serious numerical issue in the discretized models. MacArthur et al. proposed a very interesting combination of MB technique and FV technique in order to model the heat exchanger [66]. The two-phase region is modelled by the MB technique while the superheated region is modelled by the FV technique. MacArthur et al. stated the differences between the regions inside the heat exchanger as the primary reasons for the difference in modelling techniques. The liquid phase and the vapor phase in the two-phase region travel at different velocities which results in a density that needs to be calculated with proper accuracy using void fraction, which can only be done in the MB technique. Zhang et al. modelled both the condenser and the evaporator using the MB technique, while the pump and the expander are functions of static equations [108]. All the aforementioned works using MB techniques had their own assumptions based on their applications and goals.

In [81], Quoilin used the FV model for his SORC because of his preference for a robust model. He discretized the heat exchangers into N number of cells and applied energy and mass conservation equations for each of the cells. Static models were used for the pump and the expander to keep the model simple. The heat source, or secondary fluid as he termed it, is considered a single-phase fluid and thus modelled it by only its mass flow rate, average heat capacity and density. The fluid properties were calculated using TILMedia library coupled to Refprop and these properties were assumed to vary only in the flow direction. However, in other works [83][84], Quoilin in coalition with others, used the $\varepsilon - NTU$ technique to model the heat exchangers and found a fairly good agreement between the simulated results and the experimental results. The $\varepsilon - NTU$ technique divides the heat exchanger into three zones - liquid, two-phase and vapor, each of them characterized by their corresponding heat exchange coefficient. In [82], Sylvain et al. used the FV technique for

the evaporator moeling but uses a much more simplified algebraic equation to model the condenser. The simplification of the condenser is based on the assumption that the temperature and flow rate of the heat sink are constants.

Wei et al. modelled an SORC using both the MB technique and FV technique to compare with experimental data from an ORC pilot plant [102]. While the MB technique remains the same as the previous literature, they proposed a new FV method for dynamic modelling of heat exchangers by incorporating the momentum balance equation for certain cells . Pressure drop is not neglected in this new model since wall friction and gravitational force are taken into account under the momentum balance equation. The simulation results from both the models match the experimental results with a highest error of 4%. However, due to much more mathematical complexity involved in the FV technique, the MB technique is suggested for the purpose of control design applications. For a centrifugal chiller system [15], Bendapudi et al. modelled shell-and-tube heat exchangers using the FV technique, and they suggested that the heat exchanger should be discretized into a minimum of six cells to capture the superheating process while a minimum of fifteen cells are required to function properly at a system level.

Few references can be found regarding dynamic modelling of heat exchangers dealing with supercritical parameters of working fluids. Static models have been developed for supercritical heat exchangers, but that is not sufficient for the purpose of control design. Ruivo et al. formulated a model of a countercurrent packed column operating at supercritical fluid using a set of partial differential equations (PDEs) corresponding to the differential material balances [87]. Using the method of lines, the set of PDEs were then solved by decoupling the spatial and time discretization into a system of ordinary differential equations (ODEs) with respect to time. Simoes et al. also decoupled a set of PDEs for a double-pipe heat exchanger using a control volume method into a set of ODEs and solved it to simulate the model [92]. The simulated results from the dynamic model were then compared to the experimental results obtained from a lab-scale heat exchanger, and the developed model was able to predict within $\pm 2.3\%$ of the experimental data. Rasmussen and Alleyne used Leibniz's equation to solve an existing set of PDEs for a given heat exchanger in

order to free the model of spatial dependence [86]. This allowed them to develop a dynamic model for heat exchangers working in a supercritical environment using the LP approach.

1.5 Working fluid selection and performance analysis

Selection of the working fluid used in an ORC is critical to cycle performance, and constitutes an ongoing challenge for researchers. The selection should ensure high thermal efficiency allowing high utilization of the available waste heat. Additionally, the working fluid must satisfy safety criterion while still resulting in a low cost for the plant. Few common working fluids that are used in ORC applications are R123 (2,2-Dichloro-1,1,1-trifluoroethane), R113 (1,1,2-trichloro-1,2,2-trifluoroethane), R245fa (1,1,1,3,3-Pentafluoropropane), R134a(1,1,1,2-tetrafluoroethane), etc. Table 1.1 shows thermal efficiencies for few working fluids with various critical temperatures for an ideal recuperated ORC cycle [19]. In order to ensure environmental safety, the following safety standards are maintained when selecting the working fluid [98]:

- Not ODS (Ozone Depleting Substances), or zero ODP (Ozone depleting potential)
- GWP (Global Warming Potential) < 5000
- Rank A1, A2, or B1 from ASHRAE safety classification (the ranks are described in Table 1.2)

Working fluid	Critical temperature (^{o}F)	Ideal recuperated thermal efficiency (%)
HFC134a	213.9	15.8
HFC236fa	256.9	19.4
CFC114	294.134	22.4
HFC245fa	309.29	23.3
HCFC123	362.63	26.4
CFC11	388.4	26.8
CFC113	417.38	30.1

Table 1.1: Thermal efficiency of an ideal recuperated ORC for different working fluids

	Lower Toxicity	Higher Toxicity
Higher Flammability	A3	B3
Lower Flammability	A2	B2
No flame propagation	A1	B1

Table 1.2: ASHRAE safety classification

Numerous studies have been carried out in recent years in order to find the "best match working fluid" for an ORC. However, a general best match does not exist since the choice varies depending on heat sources, working regions and conditions, the size of the ORC, etc. Several guidelines have been provided in the literature by evaluating the performance of the working fluids under different circumstances and required performance. In [96], Bertrand discusses several criteria and finally proposes a general methodology for selection of working fluids in ORC systems. He proposes working fluids with low specific volumes to be used since such fluids increases heat transfers in the heat exchangers while minimizing the feed pump work. Working fluids with high molecular weight

are also recommended for single-stage turbines. The working fluid must also be compatible with the materials and lubricants in contact to ensure thermal stability and minimum flow resistance. From an economic point of view, the fluid must be readily available and cheap. However, ORC performance analysis for the selection of working fluids has overshadowed all other factors, at least in the literatures. There are plenty of potential candidates for the selection process of a working fluid. Thus, several papers have focused on comparing the performance of the candidates to determine their choice of the best fit according to their experimental environments. Of these environments, SORCs are found to be more common in the literatures than TORCs.

Bo-Tau et al. have studied the effect of several working fluids on an SORC and compared their performances [64]. The team first categorized the working fluids into three categories of wet, dry and isentropic fluids, and then considered thermal efficiency and total heat recovery efficiency as measures of performances. Firstly, they observed that wet fluids are unfitting for an ORC because of a larger enthalpy requirement for vaporization, whereas dry fluids and isentropic fluids do not have this issue. Also, wet fluids, when expanded, leave liquid droplets in the turbine causing corrosion in the turbine blades. They also conclude that lower critical temperature (T_{crit}) working fluids (somewhat) lower thermal efficiency and substantially decrease the total heat recover efficiency. On the other hand, in [28], Chen et al. state that fluids with lower T_{crit} and lower critical pressure (P_{crit}) are potential candidates for a TORC. Several factors have been considered in this study by Chen et al. - including the influence of latent heat, density and specific heat, effectiveness of superheating, the critical points of the working fluids, stability of the fluid and compatibility with materials in contact, environmental aspects, safety, availability and cost. They introduced a new chart for classifying the fluids into five distinct groups. The chart is basically a ξ versus T_c diagram, where ξ is the inverse of the slope of a temperature-entropy diagram, and the value of ξ determines how much dry or wet the fluid is, i.e., $\xi > 0 \Rightarrow$ dry fluid, $\xi < 0 \Rightarrow$ wet fluid, and $\xi \approx 0 \Rightarrow$ isentropic fluid. Each of the five groups are discussed with their merits and drawbacks, and since there is no best fluid which can fulfill all the criteria mentioned earlier, the authors suggest to compromise when selecting the working fluid based on needs and conditions of the application

itself.

In [36], Drescher et al. studied fluid selection for a subcritical biomass power and heat plant. Thermal stability, compatibility, environmental issues and economical issues are discussed only in qualitative respects. However, they suggested that evaluating thermal efficiency for biomass applications is sufficient for the choice of a proper working fluid. From their simulation results, they could achieve the highest thermal efficiency when the working fluid was refrained from superheating and was expanded directly from the dew line. The results also showed that there is an optimal evaporating pressure at which the maximum thermal efficiency can be achieved. Along with that, the results also confirm that the thermal efficiency is highest when the process temperature is at a maximum and the upper bound for the process temperature is determined by the thermal stability and compatibility of the fluid with its contact materials. On the other hand, for a geothermal power generation system in Turkey, Etemoglu discusses the importance of the Second Law of Thermodynamics for the purpose of selection of working fluids (over the First Law which is more commonly used for the evaluation of performances), since the Second Law takes into account the useful work [40]. Mago et al. in [69] uses both First Law and Second Law to evaluate the performance of different dry working fluids. Aghahosseini and Dincer also investigated several working fluids for a SORC using both First Law and Second Law criteria.

Maizza and Maizza investigated pure fluids and blended fluids for waste heat recovery SORCs using Carnot efficiency and Rankine cycle efficiency as the means of measure [70]. They state that for their particular environmental setup and application, the difference in the two efficiency values is an appropriate measure for the selection of working fluids. Using this difference measurement, they concluded from their results that pure fluids such as R123 and R124 exhibit good system performance.

Yamamoto et al. experimented with the most conventional working fluids, water and an organic fluid R123, to show that organic fluids are better choices for low-grade heat sources systems since they increase the cycle performance drastically [105]. When water is used as the working fluid, an increased turbine inlet temperature increases turbine power; when organic fluids are used

the turbine inlet temperature is as close as possible to the boiling temperature giving the best performance of the system. However, in [29], Chen et al. compares another non-organic fluid, CO_2 (carbon dioxide), with R123 in order to evaluate the performance of a waste heat recovery system. The results obtained showed that CO_2 gives slightly more output power compared to that of R123. However, that does not seem to be a fair comparison between the two, since the CO_2 as a working fluid was tested in a transcritical cycle, whereas, R123 was tested in a subcritical cycle. In [28], Chen et al. raises concern over using CO_2 as the working fluid because of the required operating condition of 60-160 bar which is a definite safety concern. In addition to that, CO_2 needs to be cooled below its critical temperature of 31^{o}C (close to 20^{o}C), which presents a challenge and creates stress on the condenser itself. Thus they suggest searching for alternative working fluids which can overcome these issues. Later in [27], Chen et al. studies a zeotropic mixture working fluid (0.7R134a/ 0.3R32) for a TORC and compares it with a SORC using a pure fluid (R134a). The results showed that TORC using zeotropic mixture has better thermal efficiency and exergy efficiencies of the heating and condensation processes compared to the SORC under the same thermal conditions. Radulovic and Castaneda also investigated six different zeotropic mixtures for a TORC powered by geothermal energy source by varying the high pressure and temperature at the turbine inlet in order to identify the best thermal and exergetic performance [85]. They concluded that pure fluids have lower thermal efficiency and exergy efficiency, and the zeotropic mixture of R- 143a(0.2)/R-124a(0.8) exhibited the best performance of all the candidates.

Chao et al. went one step further by not only evaluating net power output and total heat transfer capacity, but also accounted for how different working fluids affect the sizing parameters of the expander [49]. In [12], Bao and Zhao discussed the working fluid selection process as well as expander selection. As the choice of working fluids impact the operation of the expander, the study suggests that the working fluid should be determined by taking into account the limitations of the expander (types of expanders are inherently limited). Wang et al. in [99] considered one more aspect for the choice of working fluids (beside thermal efficiency, heat absorption rate, and exergy destruction rate), the pump power consumption. This study, prior to installation, will give

an idea of how much influence the working fluid will have on the net power through-pump power consumption. Dai et al. also did parametric optimization of an SORC with 10 different working fluids with net power as the objective function [32]. The study showed that a higher turbine inlet temperature does not lead to higher turbine output; for working fluids with non-negative slope of the saturation vapor curves, the turbine inlet temperature should be as low as possible (just above the boiling point). The internal heat exchanger could not improve the performance of the ORC. They concluded that R236EA was the optimal working fluid for their system, and since it has less turbine inlet specific volume, it allows for smaller dimensions for the turbine design. Torres and Rodríguez analyzed and optimized a solar ORC with respect to solar collector area required for 12 different working fluids [34]. They concluded that usually dry fluids yield lower values of the unit aperture area than wet fluids. These sort of studies, where the sizing and influence of the components are considered, give industry some guidelines for choosing a working fluid prior to installation of the system.

Most of the aforementioned studies deal with selecting working fluids for SORCs; there are few studies which involve selection of working fluids for TORCs. In [73], Dariusz and Jaroslaw used micro combined heat and power units based on ORC to compare several potential candidates of working fluid for both SORC and TORC . The working fluids selected had to first pass environmental and safety criteria, and were then evaluated based on Carnot efficiency and overall cycle efficiency for the two different cycles. The results showed a clear advantage for the working fluids working in supercritical conditions over subcritical conditions. Karellas and Schuster also found working fluids under supercritical conditions to be more effective in maximizing the efficiency of the cycle during their study of supercritical fluid parameters in ORC applications [55]. Gao et al. conducted a study solely on TORC [43], in which (beside the general characteristics like low toxicity, fluid stability, and low flammability) they compared eighteen different working fluids based on their performance in maximum net power, maximum cycle efficiency, maximum exergy efficiency, minimum total heat transfer requirement, and minimum expander size. Since it is difficult to find a fluid that fulfills the requirement of maximum output and minimum investment at the same time,

they recommended R152a and R143a as the "optimal" working fluids as both these fluids exhibit a good trade-off.

However, for the purpose of this work, no study was carried out for the selection of working fluid. Rather, it was assumed that the working fluid most suitable for this particular ORC system is R134a which has the properties shown in Table 1.3 [9][37][39]. Brasz and Bilbow, for R134a in an actual recuperated SORC cycle, calculated a thermal efficiency of approximately 10% [19].

Fluid name	Critical Temperature	Critical Pressure	ODP	GWP	Rank in ASHRAE Handbook
R134a	101.08^{o}C	4060.3 kPa	0	1300	A1

Table 1.3: Properties of R134a

In [100], Wang et al. performed multi-objective optimization solely for R134a as the working fluid for a SORC. The objectives of the study was to maximize exergy efficiency and minimize the overall capital cost under the given waste heat conditions, where both these objectives are competing with each other. To achieve this, they used a thermodynamic model and an economic model to calculate the exergy efficiency and the overall capital cost respectively by a set of algebraic equations. The multi-objective optimization was performed using NSGA-II using turbine inlet pressure, turbine inlet temperature, pinch temperature difference, approach temperature difference and condenser temperature difference as the variables since these parameters have significant effects on both the objectives. Through optimization, a pareto front was obtained and the optimum operating conditions were chosen by a process of decision-making. The result was a 1.8-2.3 MPa turbine inlet pressure and about 90^{o}C turbine inlet temperature. Sun and Li also investigated system thermal efficiency and system net power generation for R134a as the working fluid in an ORC heat recovery power plant [94]. The results obtained show that higher expander inlet pressure results in more system net power generation and higher system thermal efficiency, and linear relationships exist among the system thermal efficiency, the system net power generation and expander inlet pressure. The study also reveals that the condenser fan air mass flow rate has less influence on

both objectives.

1.6 Control design for ORC

Very few works have been done in the past developing control strategies for an ORC plant. Difficulties include large nonlinearities, uncertainties, and multi-variable coupling present in an ORC system [106]. Zhang et al. in [106] presents a multi-variable control strategy by incorporating a Linear Quadratic Regulator (LQR) with a Proportional Integral (PI) controller. A 4-input-4-output multi-input multi-output (MIMO) strategy was proposed for an SORC system. The manipulated variables (MVs), *i.e.* control inputs, are the valve position, the speed of the pump, the velocity of the exhaust gas, and the velocity of the cooling air. The controlled variables (CVs), *i.e*. the system outputs, are the power output, the evaporating pressure, the superheated temperature at the outlet of the evaporator, and the temperature at the outlet of the condenser. They put the controller into several tests including set-point tracking and external disturbance rejection. The controller performs very well in both types of tests with acceptable changes in the control signals (although a bit sharp at some instances), with low overshoot and zero steady-state error. However, the proposed control requires an accurate linear state space model of the ORC system, which is a great challenge in itself. In [107], Zhang et al. proposes a General Predictive Control (GPC) strategy which does not require the knowledge of a linear state space model. GPC is a multi-variable control scheme appropriate for systems having strong interactions between the variables, disturbances and operating constraints. It generates control signals by minimizing a cost function that takes into account the future output errors and control inputs. They used the same MVs and CVs as [106] for their control strategy and similar tests were done as well to observe the performance of the GPC. The GPC was successful in both set-point tracking and disturbance rejection with little overshoot and zero steady-state error. The control signals are again a little sharp, but still acceptable. Soon afterwards, Zhang et al. designed a constrained Model Predictive Control (MPC) for a SORC [108] which also performed well in tracking the set points in the presence of variation of the heat source and

output power. However, in this study, they used a 3-input-3-output MIMO strategy with expander speed, pump speed and cooling air mass flow rate as the MVs and superheating temperature, evaporating pressure and condenser outlet temperature as the CVs. Sylvain et al. decided to ignore the multi-variable interactions and designed a SISO PI controller [82]. They used a 2-input-2-output SISO strategy where the MVs are the expander speed and the pump speed and the CVs are the evaporating temperature and the superheating temperature. The evaporating temperature being a more critical condition of the system, it was paired with the expander speed while the superheating temperature was paired with the pump speed; thus two PI controllers were established with two different loops.

1.7 Cerebellar Model Articulation Controller (CMAC)

In 1971, James Albus first proposed a computer algorithm that can mimic the motor control functions inside a brain, the first artificial neural network. It modelled the functioning of the cerebellum. The cerebellum's primary task is to send nerve signals that will ensure correct coordination of moving body parts. The proposed algorithm can generate commands required for achieving proper motor activities by comparing or correlating incoming patterns with existing stored patterns [8]. Then in 1975, Albus developed his proposed model into an adaptive controller, the Cerebellar Model Arithmetic Computer (CMAC), which includes a memory addressing algorithm (hash coding) that makes it possible to store the necessary data in a practical physical memory [7][6].

In 1990, Kraft and Campagna studied the CMAC in comparison to two traditional adaptive controllers, the self-tuning regulator (STR) and model reference adaptive controller (MRAC) [59]. They investigated the three controllers in terms of closed-loop system stability, speed of adaptation, noise rejection, the number of required calculations, system tracking performance, and the degree of theoretical development, and concluded with pros and cons of the three control schemes. Although the CMAC performed well in all the aspects of the study, it had the worst performance

in terms of convergence speed among the three controllers. Afterwards, in 1991, Glanz along with Miller and Kraft, studied CMAC applications in pattern recognition, robot control and signal processing [44]. In their study, they came to the conclusion that CMACs are more realizable in practice compared to the dominant multi-layer perceptron (MLP) neural network. The CMAC has faster convergence compared to the MLP and thus a better fit for real-time applications, but no clear indication was provided as to how much faster is "fast enough". Later in 1992, Parks and Militzer compared five different learning algorithms, including the original learning algorithm developed by Albus in 1975, to study the convergence speed of the CMAC under several test conditions including disturbance tests [77]. Out of the five algorithms investigated, the maximum error (ME) algorithm proved to be the best for all the test problems, exhibiting good convergence speed and requiring moderate computational effort, thus recommended by the authors. Commuri and Lewis, in 1995, developed a novel weight-update law for the CMAC that guarantee the closed-loop stability[30]. In their conclusion, they state that the controller is "model-free" in the sense that it succeeds achieving the required performance for a general class of nonlinear systems. In 1997, Lin and Chiang used a mathematical formulation for CMAC in order to investigate the convergence properties of the CMAC [63]. They used algebraic equations in matrix form to describe information retrieval and learning and used these equations to study the convergence properties and learning characteristics with and without hash coding.

Dr. Chris J.B. Macnab at the University of Calgary has done significant work on neural networks for adaptive control schemes, stability being the main core of his investigations. Through his investigation, he recognized bursting phenomena of weights in the neural networks to be an area requiring improvements and further study. For a trajectory tracking problem in the presence of persistent oscillations, he proposed a robust weight update method by generating an alternate set of weights which produce approximately the same output - avoiding weight drift [67]. Takaghaj et al., including Dr. Macnab, implemented an adaptive controller using nonlinear optimal control switching in CMAC for waste-to-energy boilers and achieved better performance when compared to the traditional PI controller [95]. Dr. Macnab proposed the idea of voting scheme for weight

updates in a CMAC for activated sludge bioreactors by taking into account the the effect of weight updates upon the average error and the result showed that the proposed controller outperforms the PI controller applied to the plant [68]. Works like [95] and [68] provide motivation for implementation of adaptive CMAC in plants like ORC that can outperform the traditional PI controllers while requiring minimal *a-priori* information about the plant model.

Shannon implemented the CMAC for a switched reluctance machine to estimate rotor position and compared the performance with a Radial Basis Function (RBF) network and a backpropagation network; CMAC proved to be more accurate in estimating the rotor position [90]. Using a Hamilton–Jacobi–Bellman (HJB) equation for optimal control of robot motion, Lewis along with Young Kim developed an optimal CMAC neural-HJB for controlling robot manipulators [58]. To ensure system-tracking stability and error convergence in a closed-loop, they used the standard Lyapunov stability analysis. Despite no knowledge of the nonlinearities in the robotic manipulator and presence of disturbances, the proposed controller exhibited robustness and adaptation to changing system dynamics. In [71], Maouche and Attari designed a hybrid controller by combining a nonlinear controller with an adaptive CMAC for a manipulator robot. While the nonlinear controller used knowledge-based modelling to provide the main control signal, the CMAC ensured the actual trajectory matched the desired one by compensating for errors due to structured and unstructured uncertainties. Larsen et al. studied the CMAC performance for ultra-precision machining in the presence of large friction [62]. The CMAC was able to ensure extremely low position errors, in the scale of nanometers, and at the same time tracking extremely low velocities to avoid sub-surface damage of the machined part (whereas conventional PID controllers are known to be insufficient for such purposes). Achmad et al. used the CMAC network for sequential image coding and found that it improved performance of mean square error (MSE) per frame by a factor of 28.1%, frame rate by a factor of 14% and perceptual quality by a factor of 24.4%, compared to the block-based coding of MPEG [4]. Bucak and Karlik used the CMAC network to perform environmental investigation - detection of drinking water quality to be more precise [21]. They compared their results from CMAC with an MLP and realized more accuracy and faster

learning capability of the CMAC - the success rate of the CMAC detecting the water quality was almost 100% (achieved near 500 iterations) compared to 98% for the MLP (achieved after 1000 iterations).

Advantage of using any neural network controller is that the controller does not require prior knowledge of the dynamic model of the system to be controlled [10]. To rely on a model can eventually result in tracking inaccuracy when there is change in the system dynamics due to disturbances or changes in operating conditions [13]. An adaptive CMAC neural network is advantageous over other neural networks because of its faster convergence [25]. It has the unique property of training certain areas of the memory without affecting the whole memory, which makes learning significantly faster compared to other neural networks [33]. However, the adaptive CMAC needs to be decentralized unlike MIMO controllers.

1.8 Thesis contribution

Throughout the literature, plenty of efforts have been made to model and optimize the SORC cycles, while the TORC remains notably untapped. As for control design, only a few works have been done in the past for SORC, while no literature was found regarding TORC. In this thesis study, all of these aspects have been considered for a TORC. The objectives of this thesis are to first to produce a model of a recuperated TORC suitable for use in control design, and then compare performance and robustness of an advanced CMAC adaptive control to traditional PI control. When applying the adaptive CMAC approach, an accurate nonlinear model of the TORC is not required since the CMAC can compensate for the nonlinearities in the system. Performance based on a static model of the TORC is analyzed as well to get an idea of the operating condition.

1.9 Summary

In summary, this chapter illustrates the overall purpose of this work and outlines the processes involved in obtaining a computer simulation of a TORC plant. Details of modelling the TORC are

presented in Chapter 2. Chapter 3 describes control strategies that allows one to choose optimal set points for plant and devises control techniques that will ensure set-point tracking and disturbance rejection. The results obtained are shown in Chapter 4. Finally, in Chapter 5, summary of the thesis is discussed along with potential future works.

Chapter 2

Modelling

2.1 Modelling

Modelling of an ORC is a necessary prerequisite toward designing a well-structured control system. Many researchers, including [81] [107] [108], have worked on modelling of an ORC in subcritical regions, but modelling of an ORC working in the transcritical region is rare in the literatures. Also, the typical ORC models have no recuperator in them, but in this work, a recuperator has been added which increases the overall model complexity. Thus, the ORC model developed for this thesis has six components in total: evaporator, condenser, recuperator, pump, expander and valve.

The modelling of the ORC plant has been divided into two categories - fast and slow dynamic components. [81]. The fast dynamic components have very small time constants compared to the slow ones, and are modelled as constant terms. The fast dynamics components include the pump, the expander, and the valve. Thus, the slow dynamics components are the heat exchangers: the recuperator, the condenser, and the evaporator. The dynamic modelling for the heat exchangers provides a platform for transient analysis of the system and control-system development.

In order to model an ORC working in both subcritical and supercritical regions, it is essential to apply the proper methodology for heat exchanger modelling. Therefore, the rules in Table 2.1 are established:

Working fluid region	Component	Technique
Subcritical	Condenser	Moving Boundary
Supercritical	Evaporator	Lumped parameter
Subcritical + Supercritical	Recuperator	Lumped parameter

Table 2.1: Rules for heat exchanger modelling

Table 2.1 suggests that when the working fluid is in the subcritical region, which is the case inside the condenser, it should be modelled using the moving boundary technique [50][54][86]. In the second case where the working fluid is in the supercritical region only inside the heat exchanger (in the evaporator) it should be modelled using the lumped parameter technique [86]. The final scenario, when the working fluid is in the subcritical region on one side and is in the supercritical region on the other side, which is the case inside the recuperator, it should be modelled using the lumped parameter technique as well. Also, as seen in Figure 1.2, the cycle is divided into two parts based on high pressure and low pressure. The higher pressure is imposed by the dynamics of the evaporator, while the lower pressure is imposed by the condenser [50][54][81].

2.2 Thermodynamic properties and CoolProp

The thermodynamic properties for the fluids involved in the ORC process are required to create a computer model. One option to obtain these thermodynamic properties is to perform the tedious thermodynamic calculations. However, using a precalcluated database for the properties allows relatively fast computer simulations. Thus the CoolProp [14] C++ library was utilized in this thesis. CoolProp is a free platform that outputs one thermodynamic property of a fluid given two other properties as inputs. For example, to get the density value (ρ_{val}) of a certain fluid (e.g. R134a), two other properties such as the temperature (T_{val}) and pressure (P_{val}) of the fluid must be fed as input to the CoolProp with proper syntax. An example with the syntax is shown below for MATLAB:

$$\rho_{\text{val}} = CoolProp.PropsSI('D','T',T_{\text{val}},'P',P_{\text{val}},R134a). \tag{2.1}$$

Details of computing the thermodynamics properties of fluids can be studied in the CoolProp website. It is important to note that there are restrictions to input combinations.

2.3 Structure of the heat exchangers

Concentric-annular-tube heat exchangers were chosen for the model in this thesis because of their simplistic design. Due to their robust build, they can tolerate high pressure operations [89]. They also can induce turbulent conditions at low flow rates, increasing the heat transfer coefficient and consequentially the heat transfer rate [31]. In Figure2.1, the cross view of a heat exchanger can be seen, where the inner pipe has an internal radius r_i and an external diameter r_o, and the external pipe has an inner radius of R_i. Therefore, the cross sectional area of the wall can be computed as $A_w = \pi(r_o - r_i)^2$. The material of the wall is assumed to be copper in all the heat exchangers.

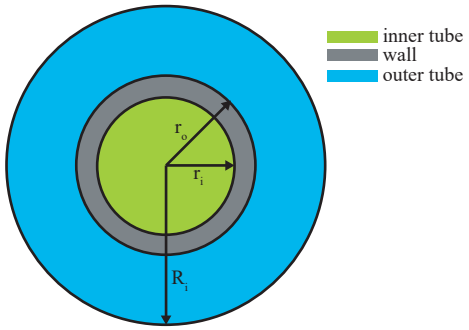

Figure 2.1: Cross-view of a concentric annular tube heat exchanger

In a concentric-annular-tube heat exchanger, both counter-flow and parallel-flow designs are possible. Counter flow has some distinct advantages over parallel flow. A common analysis to compare the two designs is the use of the log mean temperature difference (LMTD) [2].

$$\text{LMTD}, \triangle T_m = \frac{\triangle T_2 - \triangle T_1}{ln(\frac{\triangle T_2}{\triangle T_1})} \tag{2.2}$$

where $\triangle T_1$ is the larger temperature difference between the two fluid streams at either the entrance or the exit to the heat exchanger and $\triangle T_2$ is the smaller temperature difference between the two fluid streams at either the entrance or the exit to the heat exchanger.

In order to understand the process of comparison, Fig.2.2 illustrates a better view of the issue. The efficiency (in terms of heat transfer rate per unit surface area) of a counter flow is higher due to the fact that the average difference in temperature of the two fluids over the length of the heat exchanger is higher (see Fig.2.2). This results in a larger LMTD for a counter-flow heat exchanger. This can be seen in the temperature profile in Fig.2.2. In parallel flow, the cold stream outlet, $T_{c,\text{out}}$, is always less than that of the hot stream outlet, $T_{h,\text{out}}$, and thus the heat transfer is restricted by $T_{c,\text{out}}$,. In counter flow, the restriction is eased and $T_{c,\text{out}}$ can exceed $T_{h,\text{out}}$. Therefore, larger heat recovery can be achieved using a counter-flow design. It is important to note that for the condenser, there is no need for an external tube since it is fan-cooled.

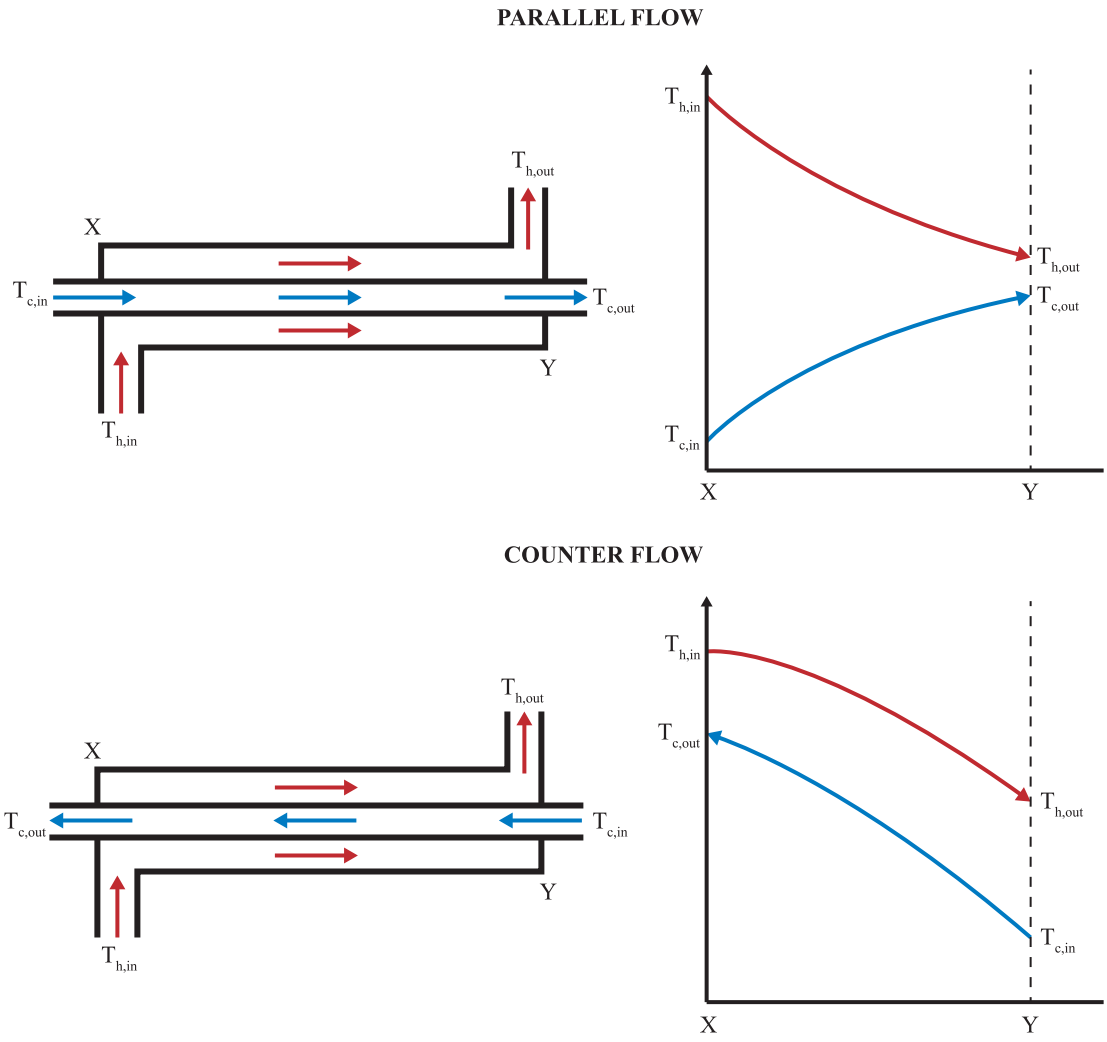

Figure 2.2: Side-view of concentric annular tube heat exchanger - parallel flow and counter flow and their temperature profiles

2.4 Some important terminology for ORC modelling

This section introduces some terminology needed to describe modelling of an ORC.

2.4.1 Average Void Fraction $(\overline{\gamma})$

The average void fraction is a lumped parameter which describes the fraction of the total volume occupied by gas and it is limited to $0 \leq \overline{\gamma} \leq 1$. It is not uncommon to use the constant average void fraction in moving boundary modelling [51][53][79]. However, to get a more accurate model

of the system, a new method to calculate the average void fraction is presented in [54] which has been used in this thesis. The method includes the effect of slip (S), which is the ratio of the average phasic velocities and for most technical applications limited to $1 \leq S \leq \sqrt{\frac{\rho'}{\rho''}}$. The slip is calculated using a simple correlation presented by Zivi in 1964 [103] as shown in equation (2.3).

$$S = \left(\frac{\rho'}{\rho''}\right)^{\frac{1}{3}} = \mu^{-\frac{1}{3}}. \tag{2.3}$$

Now, using equation (2.3), [54] has come up with the following equation for the average void fraction

$$\overline{\gamma} = \frac{(x_{\text{out}} - x_{\text{in}})\left(1-\mu^{\frac{2}{3}}\right) - \mu\left\{x_{\text{in}}\left(\mu^{-\frac{1}{3}}-1\right)+1\right\}\left\{x_{\text{out}}\left(\mu^{-\frac{1}{3}}-1\right)+1\right\}\beta}{(x_{\text{out}} - x_{\text{in}})\left(1-\mu^{\frac{2}{3}}\right)^2}, \tag{2.4}$$

where x is the quality of the fluid and

$$\beta = ln\frac{\left\{x_{\text{in}}\left(\mu^{\frac{1}{3}}-1\right)+1\right\}\left\{x_{\text{out}}(1-\mu)+\mu\right\}}{\left\{x_{\text{out}}\left(\mu^{-\frac{1}{3}}-1\right)+1\right\}\left\{x_{\text{in}}(1-\mu)+\mu\right\}}. \tag{2.5}$$

For the two-phase region inside the condenser, $x_{\text{in}} = 1$ and $x_{\text{out}} = 0$, and thereby equation (2.5) becomes

$$\beta = ln\left(\mu^{\frac{2}{3}}\right). \tag{2.6}$$

The quality of the fluid signifies the ratio of the mass of vapor to the total mass of vapor and liquid present in a saturated mixture of the working fluid, i.e., $x = 1$ for saturated vapor and $x = 0$ for saturated liquid. Also, by substituting equation (2.6) into equation (2.4), the average void fraction for the two-phase region of a condenser is

$$\overline{\gamma} = \frac{1-\mu^{\frac{2}{3}}\left\{1+ln\left(\mu^{-\frac{2}{3}}\right)\right\}}{\left(1-\mu^{\frac{2}{3}}\right)^2}. \tag{2.7}$$

2.4.2 Heat Transfer Coefficient (α)

The heat transfer coefficient is one of the most important calculations when modelling an ORC as it dictates the heat transfers taking place throughout the cycle. Thus, it is important to identify the proper methodology to enumerate this value for individual regions and/or components. Variations around the nominal value of heat transfer coefficient is used in [81] to calculate the heat transfer coefficient. Using Gnielinski's correlation [52], the heat transfer coefficient has been calculated in [54]. Several other techniques can be found in the literature for the calculation of heat transfer coefficients for different regions.

2.4.2.1 Single-phase flow for the inner tube

For the calculation of heat transfer coefficient in single phase regions, the same technique has been used as [54]. In order to do that, first the Reynol's number (Re) is computed as

$$\mathrm{Re} = \frac{\dot{m}D}{A\eta}, \tag{2.8}$$

where $\dot{m}$ is the mass flow rate of the fluid, D is the internal diameter of the tube, A is the cross-sectional area of the tube and η is the dynamic viscosity of the fluid. Using equation (2.8), the Moody friction factor (ξ) can be computed by the following equation [52]

$$\xi = \{0.790ln(\mathrm{Re}) - 1.64\}^{-2}. \tag{2.9}$$

The Prandtl number (Pr) can be computed using the following relation

$$\mathrm{Pr} = \frac{\eta c}{\lambda}, \tag{2.10}$$

where c is the specific isobaric heat capacity and λ is the thermal conductivity of the fluid. Using values obtained in equations (2.8), (2.9) and 2.10, the Nusselt number (Nu) is then computed

$$\mathrm{Nu} = \frac{(\xi/8)\,(\mathrm{Re}-1000)\,\mathrm{Pr}}{1+12.7\,(\xi/8)^{\frac{1}{2}}\left(\mathrm{Pr}^{\frac{2}{3}}-1\right)}. \tag{2.11}$$

Therefore, using the value obtained from equation (2.11), the heat transfer coefficient for the single phase region is

$$\alpha = \frac{\lambda \mathrm{Nu}}{D}. \tag{2.12}$$

2.4.2.2 Two-phase flow for the inner tube

The heat transfer coefficient of the fluid in the two-phase region can be expressed in terms of a single phase heat transfer coefficient (using α' and α'' for the liquid and vapor respectively) by [54]

$$\alpha = \alpha' \left[(1-x) + 1.2x^{0.4}\left(\frac{\rho'}{\rho''}\right)^{0.37}\right]^{-2.2} + \alpha' \left[\frac{\alpha''}{\alpha'}x^{0.01}\left(1+8\,(1-x)^{0.7}\left(\frac{\rho'}{\rho''}\right)^{0.67}\right)\right]^{-2}, \tag{2.13}$$

where x is the quality of the fluid in the two-phase region in the range $0 \leq x \leq 1$ ($x = 0$ indicating liquid at saturation temperature and $x = 1$ indicating vapor at saturation temperature) and, ρ' and ρ'' are density values at $x = 0$ and $x = 1$ respectively. The coefficients α' and α'' are calculated using equation (2.12) at $x = 0$ and $x = 1$ respectively. All these values can be obtained using CoolProp.

2.4.2.3 Single-phase flow for the outer tube

As discussed earlier, the heat exchangers have outer diameters, i.e. an annular passage for the hot side flow (see Figure 2.1). Fluid flowing through the external tube does not have the same heat transfer coefficient calculation as that of the the internal tube. A different approach is used as

suggested in [22].

Firstly, the hydraulic mean diameter $(l = D_i - d_o)$ is calculated from the inner diameter of the outer tube $(D_i = 2R_i)$ and outer diameter of the inner tube $(d_o = 2r_o)$ referring to Figure 2.1. Then the channel flow area (S) is calculated using the following equation

$$S = \frac{\pi}{4}\left(D_i^2 - d_i^2\right). \tag{2.14}$$

Using the value obtained from equation (2.14), the fluid mean velocity (v) is calculated using

$$u = \frac{\dot{m}}{\rho S}, \tag{2.15}$$

where ρ is the density and $\dot{m}$ is the mass flow rate of the fluid. Using the value obtained from equation (2.15), the Reynold's number is obtained by the following equation

$$\mathrm{Re} = \frac{\rho v l}{\eta}. \tag{2.16}$$

Then the Prandtl number is calculated using equation (2.10). Using values obtained from equations (2.10) and (2.8), the Stanton number (St) number is calculated

$$\mathrm{St} = E\,(\mathrm{Re})^{-0.205}\,(\mathrm{Pr})^{-0.505}, \tag{2.17}$$

where $E = 0.0225e^{\left\{-0.0225(lnPr)^2\right\}}$. Finally, using the Stanton number obtained from equation (2.17), the heat transfer coefficient of the fluid in the outer tube is

$$\alpha = \rho \times v \times c \times \mathrm{St}. \tag{2.18}$$

2.4.2.4 Heat-transfer coefficient of air in the condenser

The Prandtl number for air is calculated using equation (2.10). The Reynold's number is calculated using the following equation

$$\mathrm{Re} = \frac{\rho v d_o}{\eta}. \tag{2.19}$$

The Nusselt number is thus calculated using equation (2.11). Finally, the heat transfer coefficient is calculated by using equation (2.12). A linear relation between the air mean velocity (v) and the fan speed (N_{fan}) is assumed: $v = k_{\mathrm{vel}} N_{\mathrm{fan}}$, where $k_{\mathrm{vel}} = 1$ is a constant.

The thermodynamic properties λ, η and c are computed using CoolProp.

2.5 Slow dynamics components

As mentioned earlier, all the heat exchangers in the ORC are slow dynamics components. Possible dynamic models include moving boundaries models and lumped parameter models. The moving boundary technique divides the heat exchanger into several zones, and the zone boundaries vary with time in respect to the current condition of the heat exchanger [81][50][54]. In the lumped parameter technique for supercritical heat exchangers, a single control volume is defined where the boundaries do not vary with time [86].

2.5.1 Condenser

The condenser contains refrigerant working in the subcritical region, and thus the simpler moving boundaries technique is appropriate. The aim of the moving boundary technique is to divide the condenser into three regions: the superheated region, the two-phase region, and the sub-cooled region (Figure 2.3). The physical behaviors of these individual regions differ a lot from each other [54], *e.g.,* the heat transfer coefficient may differ by an order of magnitude between the two-phase region and the sub-cooled region. The moving boundary technique dynamically tracks the lengths of the three different regions in the condenser.

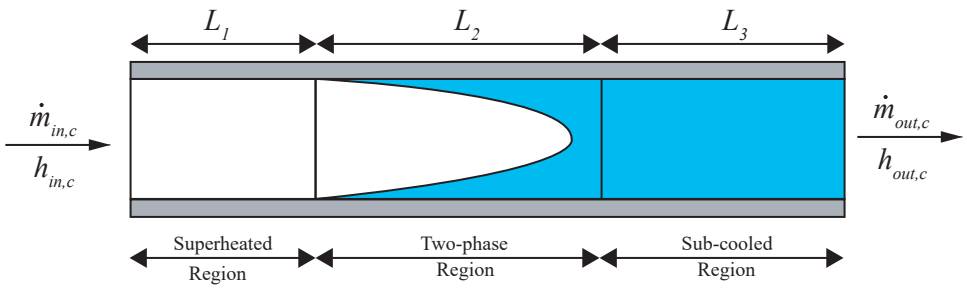

Figure 2.3: Moving boundary model for condenser

Each of the regions in the condenser is defined by a control volume and for each control volume, energy conservation and mass conservation equations are formulated in order to represent the dynamics. Average properties of the refrigerant are used in the control volumes for calculating average values of enthalpy, temperature, etc [54][50][86]. Furthermore, the mean void fraction is used in the two-phase region instead of a time-varying void fraction. Since the exit of the refrigerant from the condenser is in liquid form and not two-phase, having a time-invariant void fraction is acceptable [86]. There are other important assumptions made for modelling the condenser, which are as follows [54][50][86]:

- Gravitational forces and changes kinetic energy are negligible.
- Pressure loss is negligible.
- The two-phase is in thermodynamic equilibrium.
- Axial conduction of refrigerant is negligible.
- The refrigerant flow is modelled as one-dimensional fluid flow.

Figure 2.4 shows the schematic of a control volume studied in this thesis to obtain a mathematical model for the condenser, where the subscripts A and B represent the boundaries. Using the assumptions mentioned earlier, general mass balance and energy balance equations for the refrigerant can be obtained for each of the three regions [54][50].

Mass Balance:

$$\frac{d}{dt}\iiint \rho dV + \iint \rho(w - w_s)dA = 0 \tag{2.20}$$

Energy Balance:

$$\frac{d}{dt}\iiint(\rho h - p)dV + \iint \rho h(w - w_s)dA = \iint q dA \tag{2.21}$$

where w is the velocity of the fluid, w_s is the velocity of the surface of the control volume, q is the heat flux per unit area and p is the pressure inside the condenser. Note, p is constant throughout the condenser but is still time dependent. Now, using equation (2.20) for the control volume shown in Figure 2.4, the mass balance can be rewritten as follows:

$$A\frac{d}{dt}\int_{z_{l,A}}^{z_{l,B}} \rho dz + \rho_A A\frac{dz_{l,A}}{dt} - \rho_B A\frac{dz_{l,B}}{dt} = \dot{m}_A - \dot{m}_B, \tag{2.22}$$

where $A\frac{d}{dt}\int_{z_{l,A}}^{z_{l,B}} \rho dz$ represents the rate of change of mass and $\rho_A A\frac{dz_{l,A}}{dt}$ and $\rho_B A\frac{dz_{l,B}}{dt}$ represent the change of mass in control volume due to change in boundaries.

Using equation 2.21, the energy balance can be rewritten as

$$\begin{aligned} A\frac{d}{dt}\int_{z_{l,A}}^{z_{l,B}} \rho h dz - A(z_{l,B} - z_{l,A})\frac{dp}{dt} + A\rho_A h_A\frac{dz_{l,A}}{dt} - A\rho_B h_B\frac{dz_{l,B}}{dt} \\ = \dot{m}_A h_A - \dot{m}_B h_B + q(z_{l,B} - z_{l,A}), \end{aligned} \tag{2.23}$$

where $A\frac{d}{dt}\int_{z_{l,A}}^{z_{l,B}} \rho h dz$ represents the rate of change of enthalpy in the control volume, $A(z_{l,B} - z_{l,A})\frac{dp}{dt}$ is a result of using enthalpy in the first term instead of internal energy [54] and $A\rho_A h_A\frac{dz_{l,A}}{dt}$ and $A\rho_B h_B\frac{dz_{l,B}}{dt}$ represent the change of enthalpy in the control volume due to thechange in boundaries.

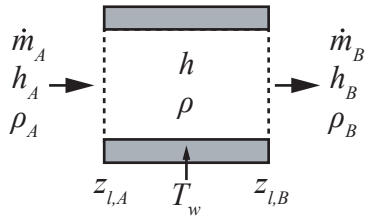

Figure 2.4: Control volume for each region

Now, the general forms of mass balance and energy balance equations as shown in equations

(2.22) and (2.23) respectively, need to be evaluated for each of the three regions of the condenser.

2.5.1.1 Superheated region

For the superheated region, $z_{l,A} = 0$ and $z_{l,B} = L_1$, and putting these relations into equation (2.22), the following mass balance equation for the superheated region is obtained:

$$\begin{aligned} A_c \frac{d}{dt} \int_0^{L_1} \rho_1 dz - \rho_g A_c \frac{dL_1}{dt} &= \dot{m}_{\text{in,c}} - \dot{m}_{\text{int1}} \\ \Rightarrow A_c L_1 \frac{d\rho_1}{dt} + A_c(\rho_1 - \rho_g)\frac{dL_1}{dt} &= \dot{m}_{\text{in,c}} - \dot{m}_{\text{int1}}. \end{aligned} \tag{2.24}$$

The time derivative of ρ_1 can be written using the chain rule

$$\begin{aligned} \frac{d\rho_1}{dt} &= \frac{\partial \rho_1}{\partial h_1}\frac{dh_1}{dt} + \frac{\partial \rho_1}{\partial P_c}\frac{dP_c}{dt} \\ \Rightarrow \frac{d\rho_1}{dt} &= \frac{1}{2}\frac{\partial \rho_1}{\partial h_1}\left(\frac{dh_{\text{in,c}}}{dt} + \frac{\partial h_g}{\partial P}\frac{dP_c}{dt}\right) + \frac{\partial \rho_1}{\partial P_c}\frac{dP_c}{dt} \\ \Rightarrow \frac{d\rho_1}{dt} &= \frac{1}{2}\frac{\partial \rho_1}{\partial h_1}\frac{dh_{\text{in,c}}}{dt} + \left(\frac{1}{2}\frac{\partial \rho_1}{\partial h_1}\frac{\partial h_g}{\partial P} + \frac{\partial \rho_1}{\partial P_c}\right)\frac{dP_c}{dt}. \end{aligned} \tag{2.25}$$

Putting equation (2.25) into equation (2.24), the following final mass balance equation for superheated region is

$$\begin{aligned} A_c L_1 \left(\frac{1}{2}\frac{\partial \rho_1}{\partial h_1}\frac{\partial h_g}{\partial P} + \frac{\partial \rho_1}{\partial P_c}\right)\frac{dP_c}{dt} + A_c(\rho_1 - \rho_g)\frac{dL_1}{dt} \\ + \frac{1}{2}A_c L_1 \frac{\partial \rho_1}{\partial h_1}\frac{dh_{\text{in,c}}}{dt} = \dot{m}_{\text{in,c}} - \dot{m}_{\text{int1}}, \end{aligned} \tag{2.26}$$

where P_c is the condensing pressure, A_c is the cross-sectional area of the inner tube, ρ_g is the saturated vapor density, h_g is the saturated vapor specific enthalpy, $\dot{m}_{\text{in,c}}$ is the inlet mass flow rate of the condenser, $\dot{m}_{\text{int1}}$ is the exit mass flow rate of superheated region and $\frac{dh_{\text{in,c}}}{dt}$ is the boundary

condition imposed by the recuperator.

Similarly, using $z_{l,A} = 0$ and $z_{l,B} = L_1$ in equation (2.23), the energy balance equation for the superheated region is obtained as follows

$$A_c \frac{d}{dt}\int_0^{L_1} \rho_1 h_1 dz - A_c L_1 \frac{dP_c}{dt} - A\rho_g h_g \frac{dL_1}{dt} = \dot{m}_{\text{in},c} h_{\text{in},c} - \dot{m}_{\text{int1}} h_g + 2\pi r_{i,c} L_1 \alpha_{i,1} (T_{w,1} - T_{\text{wf},1}). \tag{2.27}$$

The first term of equation (2.27) can be written as follows

$$\frac{d}{dt}\int_0^{L_1} \rho_1 h_1 dz = \frac{1}{2}\rho_1 \left(h_{\text{in},c} + h_g\right) \frac{dL_1}{dt} + \frac{1}{2} L_1 (h_{\text{in},c} + h_g) \frac{d\rho_1}{dt} + \frac{1}{2}\rho_1 L_1 \left(\frac{dh_{\text{in},c}}{dt} + \frac{\partial h_g}{\partial P_c}\frac{dP_c}{dt}\right). \tag{2.28}$$

Substituting equation (2.25) into equation (2.28) gives

$$\frac{d}{dt}\int_0^{L_1} \rho_1 h_1 dz = \frac{1}{2}\rho_1 \left(h_{\text{in},c} + h_g\right) \frac{dL_1}{dt} + \frac{1}{2} L_1 \left[\rho_1 + \left(h_{\text{in},c} + h_g\right) \frac{\partial \rho_1}{\partial h_1}\right] \frac{dh_{\text{in},c}}{dt} + \frac{1}{2} L_1 \left[(h_{\text{in},c} + h_g)\left(\frac{1}{2}\frac{\partial \rho_1}{\partial h_1}\frac{\partial h_g}{\partial P} + \frac{\partial \rho_1}{\partial P_c}\right) + \rho \frac{\partial h_g}{\partial P_c}\right] \frac{dP_c}{dt}. \tag{2.29}$$

Substituting equation (2.29) into equation (2.27) gives the following final energy balance equation for the superheated region

$$A_c\left[\frac{1}{2}\rho_1(h_{\text{in},c}+h_g)-\rho_g h_g\right]\frac{dL_1}{dt}+\frac{1}{2}A_cL_1\left[\rho_1+\left(h_{\text{in},c}+h_g\right)\frac{\partial\rho_1}{\partial h_1}\right]\frac{dh_{\text{in},c}}{dt}$$
$$+\frac{1}{2}A_cL_1\left[(h_{\text{in},c}+h_g)\left(\frac{1}{2}\frac{\partial\rho_1}{\partial h_1}\frac{\partial h_g}{\partial P}+\frac{\partial\rho_1}{\partial P_c}\right)+\rho\frac{\partial h_g}{\partial P_c}-2\right]\frac{dP_c}{dt}$$
$$=\dot{m}_{\text{in},c}h_{\text{in},c}-\dot{m}_{\text{int1}}h_g+2\pi r_{i,c}L_1\alpha_{i,1}(T_{w,1}-T_{\text{wf},1}), \tag{2.30}$$

where $T_{w,1}$ is the average temperature of the tube wall in the superheated region, $T_{\text{wf},1}$ is the temperature of refrigerant in the superheated region and $\alpha_{i,1}$ is the heat transfer coefficient of the refrigerant in the superheated region.

The energy balance of the wall of superheated region can be written as follows:

$$c_w\rho_wA_{w,c}\frac{dT_{w,1}}{dt}=2\pi r_{i,c}\alpha_{i,1}(T_{\text{wf},1}-T_{w,1})+2\pi r_{o,c}\alpha_o(T_a-T_{w,1}), \tag{2.31}$$

where T_a is the ambient temperature, c_w is the specific heat capacity of the wall, ρ_w is the density of the wall, $A_{w,c}$ is the cross-sectional area of the wall and α_o is the heat transfer coefficient of the ambient.

2.5.1.2 Two-phase region

For the two-phase region, $z_{l,A}=L_1$ and $z_{l,B}=L_1+L_2$, and putting these relations in equation (2.22), the following mass balance equation for the two-phase region is obtained:

$$A\frac{d}{dt}\int_{L_1}^{L_1+L_2}\rho_2dz+A\rho_g\frac{dL_1}{dt}-A\rho_l\frac{d(L_1+L_2)}{dt}=\dot{m}_{\text{int1}}-\dot{m}_{\text{int2}} \tag{2.32}$$

$$A\left\{\frac{d}{dt}(\rho_2L_2)+(\rho_g-\rho_l)\frac{dL_1}{dt}-\rho_l\frac{dL_2}{dt}\right\}=\dot{m}_{\text{int1}}-\dot{m}_{\text{int2}}, \tag{2.33}$$

where $\rho_2=\rho_l(1-\bar{\gamma})+\rho_g\bar{\gamma}$ is the average density of the refrigerant in the two-phase region and the time derivative of ρ_2 is defined as

$$\frac{d\rho_2}{dt} = \left(\overline{\gamma}\frac{d\rho_g}{dP} + (1-\overline{\gamma})\frac{d\rho_l}{dP}\right)\frac{dP_c}{dt}, \tag{2.34}$$

where $\overline{\gamma}$ is calculated using equation (2.7). Using equation (2.34) in equation (2.33), the following final mass balance equation for the two-phase region is

$$A_c L_2\left(\overline{\gamma}\frac{d\rho_g}{dP} + (1-\overline{\gamma})\frac{d\rho_l}{dP}\right)\frac{dP}{dt} + A_c(\rho_g-\rho_l)\frac{dL_1}{dt} + A_c\overline{\gamma}(\rho_g-\rho_l)\frac{dL_2}{dt} = \dot{m}_{\text{int1}} - \dot{m}_{\text{int2}}, \tag{2.35}$$

where m_{int2} is the mass flow rate at the outlet of the two-phase region.

Similarly, using $z_{l,A} = L_1$ and $z_{l,B} = L_1 + L_2$ in equation (2.23), the energy balance equation for the two-phase region is:

$$A_c\frac{d}{dt}\int_{L_1}^{L_1+L_2}\rho_2 h_2 dz + A_c\rho_g h_g\frac{dL_1}{dt} - A_c L_1\frac{dP_c}{dt} - A_c\rho_l h_l\frac{d(L_1+L_2)}{dt} - A_c L_2\frac{dP_c}{dt} = \dot{m}_{\text{int1}}h_g - \dot{m}_{\text{int2}}h_l + 2\pi r_{i,c}L_2\alpha_{i,2}(T_{w,2} - T_{\text{wf},2}). \tag{2.36}$$

The first term on the left hand side of equation (2.36) can be evaluated as

$$\begin{aligned}
&\frac{d}{dt}\int_{L_1}^{L_1+L_2}\rho_2 h_2 dz = \frac{d}{dt}\int_{L_1}^{L_1+L_2}(\overline{\gamma}\rho_g h_g + (1-\overline{\gamma})\rho_l h_l)\,dz \\
\Rightarrow &\frac{d}{dt}\int_{L_1}^{L_1+L_2}\rho_2 h_2 dz = \frac{d}{dt}\left\{(\overline{\gamma}\rho_g h_g + (1-\overline{\gamma})\rho_l h_l)L_2\right\} \\
\Rightarrow &\frac{d}{dt}\int_{L_1}^{L_1+L_2}\rho_2 h_2 dz = L_2\left[\overline{\gamma}\frac{d(\rho_g h_g)}{dP} + (1-\overline{\gamma})\frac{d(\rho_l h_l)}{dP}\right]\frac{dP_c}{dt} \\
&+ \left\{\overline{\gamma}\rho_g h_g + (1-\overline{\gamma})\rho_l h_l\right\}\frac{dL_2}{dt}.
\end{aligned} \tag{2.37}$$

Putting equation (2.37) into equation (2.36) gives the following final energy balance equation for

the two-phase region:

$$A_c\left(\rho_g h_g-\rho_l h_l\right)\frac{dL_1}{dt}+A_c L_2\left[\overline{\gamma}\frac{d(\rho_g h_g)}{dP}+(1-\overline{\gamma})\frac{d\left(\rho_l h_l\right)}{dP}-1\right]\frac{dP_c}{dt}$$
$$+A_c\overline{\gamma}(\rho_g h_g-\rho_l h_l)\frac{dL_2}{dt}=\dot{m}_{\text{int1}}h_g-\dot{m}_{\text{int2}}h_l+2\pi r_{i,c}L_2\alpha_{i,2}(T_{\text{wf},2}-T_{w,2}), \tag{2.38}$$

where $T_{w,2}$ is the average temperature of the tube wall in the two-phase region, $T_{\text{wf},2}$ is the temperature of refrigerant in the two-phase region and $\alpha_{i,2}$ is the heat transfer coefficient of the refrigerant in the two-phase region.

The energy balance of the wall of the two-phase region can be written as follows

$$c_w\rho_w A_{w,c}\frac{dT_{w,2}}{dt}=2\pi r_{i,c}\alpha_{i,2}(T_{\text{wf},2}-T_{w,2})+2\pi r_{o,c}\alpha_o(T_a-T_{w,2}). \tag{2.39}$$

2.5.1.3 Sub-cooled region

For the sub-cooled region, $z_{l,A}=L_1+L_2$ and $z_{l,B}=L_c$, and putting these relations in equation (2.22), the mass balance equation for the sub-cooled region is :

$$A_c\frac{d}{dt}\int_{L_1+L_2}^{L_c}\rho_3 dz+\rho_l A_c\frac{d(L_1+L_2)}{dt}-\rho_{\text{out},c}A_c\frac{dL_c}{dt}=\dot{m}_{\text{int2}}-\dot{m}_{\text{out},c}. \tag{2.40}$$

The time derivative of ρ_3 can be written using the chain rule

$$\begin{aligned}
\frac{d\rho_3}{dt}&=\frac{\partial\rho_3}{\partial h_3}\frac{dh_3}{dt}+\frac{\partial\rho_3}{\partial P_c}\frac{dP_c}{dt}\\
\Rightarrow\frac{d\rho_3}{dt}&=\frac{1}{2}\frac{\partial\rho_3}{\partial h_3}\left(\frac{dh_{\text{out},c}}{dt}+\frac{\partial h_l}{\partial P}\frac{dP_c}{dt}\right)+\frac{\partial\rho_3}{\partial P_c}\frac{dP_c}{dt}\\
\Rightarrow\frac{d\rho_3}{dt}&=\frac{1}{2}\frac{\partial\rho_3}{\partial h_3}\frac{dh_{\text{out},c}}{dt}+\left(\frac{1}{2}\frac{\partial\rho_3}{\partial h_3}\frac{\partial h_l}{\partial P}+\frac{\partial\rho_3}{\partial P_c}\right)\frac{dP_c}{dt}.
\end{aligned} \tag{2.41}$$

Since $L_3=L_c-L_1-L_2$, the time derivative for L_3 can be written as

$$\frac{dL_3}{dt} = -\frac{dL_1}{dt} - \frac{dL_2}{dt}. \tag{2.42}$$

The first term of equation (2.40) can be written as

$$\frac{d}{dt}\int_{L_1+L_2}^{L_c} \rho_3 dz = L_3 \frac{d\rho_3}{dt} + \rho_3 \frac{dL_3}{dt}. \tag{2.43}$$

Using equation (2.41) and equation (2.42) in equation (2.43) gives

$$\frac{d}{dt}\int_{L_1+L_2}^{L_c} \rho_3 dz = L_3 \left\{ \frac{1}{2}\frac{\partial \rho_3}{\partial h_3}\frac{dh_{\text{out},c}}{dt} + \left(\frac{1}{2}\frac{\partial \rho_3}{\partial h_3}\frac{\partial h_l}{\partial P} + \frac{\partial \rho_3}{\partial P_c} \right) \frac{dP_c}{dt} \right\} - \rho_3 \left(\frac{dL_1}{dt} + \frac{dL_2}{dt} \right). \tag{2.44}$$

Putting equation (2.44) in equation (2.40) gives the mass balance equation for the sub-cooled region as follows

$$\begin{aligned} A_c(\rho_l - \rho_3)\frac{dL_1}{dt} + A_c(\rho_l - \rho_3)\frac{dL_2}{dt} + \frac{1}{2}A_c L_3 \frac{\partial \rho_3}{\partial h_3}\frac{dh_{\text{out},c}}{dt} \\ + A_c L_3 \left(\frac{1}{2}\frac{\partial \rho_3}{\partial h_3}\frac{\partial h_l}{\partial P} + \frac{\partial \rho_3}{\partial P_c} \right) \frac{dP_c}{dt} = \dot{m}_{\text{int2}} - \dot{m}_{\text{out},c}. \end{aligned} \tag{2.45}$$

Similarly, using $z_{l,A} = L_1 + L_2$ and $z_{l,B} = L_c$, and putting these relations in equation (2.23), the following energy balance for the sub-cooled region is obtained:

$$\begin{aligned} A_c \frac{d}{dt}\int_{L_1+L_2}^{L_c} \rho_3 h_3 dz - A_c L_3 \frac{dP_c}{dt} + A_c \rho_l h_l \frac{d(L_1+L_2)}{dt} - A_c \rho_{\text{out},c} h_{\text{out},c} \frac{dL_c}{dt} \\ = \dot{m}_{\text{int2}} h_l - \dot{m}_{\text{out},c} h_{\text{out,c}} + 2\pi r_{i,c} L_3 \alpha_{i,3}(T_{w,3} - T_{\text{wf},3}). \end{aligned} \tag{2.46}$$

The first term of equation (2.46) can be written as

$$\frac{d}{dt}\int_{L_1+L_2}^{L_c}\rho_3 h_3 dz = \frac{1}{2}L_3(h_l+h_{\text{out},c})\frac{d\rho_3}{dt}+\frac{1}{2}\rho_3 L_3\left(\frac{\partial h_l}{\partial P_c}\frac{dP_c}{dt}+\frac{dh_{\text{out},c}}{dt}\right) + \frac{1}{2}\rho_3(h_l+h_{\text{out},c})\frac{dL_3}{dt}. \quad (2.47)$$

Using equation (2.41) and equation (2.42) in equation (2.47) gives

$$\frac{d}{dt}\int_{L_1+L_2}^{L_c}\rho_3 h_3 dz = \frac{1}{2}L_3(h_l+h_{\text{out},c})\left\{\frac{1}{2}\frac{\partial\rho_3}{\partial h_3}\frac{dh_{\text{out},c}}{dt}+\left(\frac{1}{2}\frac{\partial\rho_3}{\partial h_3}\frac{\partial h_l}{\partial P}+\frac{\partial\rho_3}{\partial P_c}\right)\frac{dP_c}{dt}\right\} + \frac{1}{2}\rho_3 L_3\left(\frac{\partial h_l}{\partial P_c}\frac{dP_c}{dt}+\frac{dh_{\text{out},c}}{dt}\right)-\frac{1}{2}\rho_3\left(h_l+h_{\text{out},c}\right)\left(\frac{dL_1}{dt}+\frac{dL_2}{dt}\right). \quad (2.48)$$

Putting equation (2.48) into equation (2.46) gives the energy balance equation for the sub-cooled region as

$$A_c\left(\frac{1}{2}L_3(h_l+h_{\text{out},c})\left(\frac{1}{2}\frac{\partial\rho_3}{\partial h_3}\frac{\partial h_l}{\partial P}+\frac{\partial\rho_3}{\partial P_c}\right)-1\right)\frac{dP_c}{dt}+A_c\left(\rho_l h_l-\frac{1}{2}\rho_3\left(h_l+h_{\text{out},c}\right)\right)\frac{dL_1}{dt} + A_c\left(\rho_l h_l-\frac{1}{2}\rho_3\left(h_l+h_{\text{out},c}\right)\right)\frac{dL_2}{dt}+A_c\left(\frac{1}{2}\rho_3 L_3+\frac{1}{4}L_3(h_l+h_{\text{out},c})\frac{\partial\rho_3}{\partial h_3}\right)\frac{dh_{\text{out},c}}{dt} = \dot{m}_{\text{int}2}h_l-\dot{m}_{\text{out},c}h_{\text{out},c}+2\pi r_{i,c}L_3\alpha_{i,3}(T_{w,3}-T_{\text{wf},3}), \quad (2.49)$$

where $T_{w,3}$ is the average temperature of the tube wall in the sub-cooled region, $T_{\text{wf},3}$ is the temperature of refrigerant in the sub-cooled region and $\alpha_{i,3}$ is the heat transfer coefficient of the refrigerant in the sub-cooled region. Note that $\frac{dL_c}{dt}=0$ since L_c is constant.

In order to have the outlet temperature of the condenser $(T_{\text{out,c}})$ as a state instead of the outlet enthalpy $h_{\text{out},c}$, $\frac{dh_{\text{out},c}}{dt}$ can be replaced by the following equation

$$\frac{dh_{\text{out},c}}{dt} = c_{\text{out,c}}\frac{dT_{\text{out,c}}}{dt}, \quad (2.50)$$

where $c_{\text{out,c}}$ is the specific heat capacity of the refrigerant at the outlet of the condenser. Now substituting equation (2.50) into equation (2.45), the following final mass balance equation for the sub-cooled region is obtained

$$A_c\left(\rho_l-\rho_3\right)\frac{dL_1}{dt}+A_c\left(\rho_l-\rho_3\right)\frac{dL_2}{dt}+\frac{1}{2}A_cL_3c_{\text{out,c}}\frac{\partial\rho_3}{\partial h_3}\frac{dT_{\text{out,c}}}{dt}$$
$$+A_cL_3\left(\frac{1}{2}\frac{\partial\rho_3}{\partial h_3}\frac{\partial h_l}{\partial P}+\frac{\partial\rho_3}{\partial P_c}\right)\frac{dP_c}{dt}=\dot{m}_{\text{int2}}-\dot{m}_{\text{out},c}. \tag{2.51}$$

Similarly, by substituting equation (2.50) into equation (2.49), the following final energy balance equation for sub-cooled region is

$$A_c\left[\frac{1}{2}L_3(h_l+h_{\text{out},c})\left(\frac{1}{2}\frac{\partial\rho_3}{\partial h_3}\frac{\partial h_l}{\partial P}+\frac{\partial\rho_3}{\partial P_c}\right)-1\right]\frac{dP_c}{dt}+A_c\left[\rho_lh_l-\frac{1}{2}\rho_3\left(h_l+h_{\text{out},c}\right)\right]\frac{dL_1}{dt}$$
$$+A_c\left[\rho_lh_l-\frac{1}{2}\rho_3\left(h_l+h_{\text{out},c}\right)\right]\frac{dL_2}{dt}+A_c\left[\frac{1}{2}\rho_3L_3+\frac{1}{4}L_3(h_l+h_{\text{out},c})\frac{\partial\rho_3}{\partial h_3}\right]c_{\text{out},c}\frac{dT_{\text{out},c}}{dt}$$
$$=\dot{m}_{\text{int2}}h_l-\dot{m}_{\text{out},c}h_{\text{out},c}+2\pi r_{i,c}L_3\alpha_{i,3}(T_{w,3}-T_{\text{wf},3}). \tag{2.52}$$

The energy balance of the wall of the sub-cooled region can be written

$$c_w\rho_wA_{w,c}\frac{dT_{w,3}}{dt}=2\pi r_{i,c}\alpha_{i,3}(T_{\text{wf},3}-T_{w,3})+2\pi r_{o,c}\alpha_o(T_a-T_{w,3}), \tag{2.53}$$

where α_o is the heat transfer coefficient between the wall and the ambient.

Using the mass balance and energy balance equations (2.26), (2.30), (2.31), (2.35), (2.38), (2.39), (2.51), (2.52) and (2.53) obtained above, a seven-state order model is established for the condenser. The states are as follows:

- Length of the superheated region (L_1)
- Length of the two-phase region (L_2)

- Condensing pressure (P_c)
- Outlet temperature of the refrigerant $(T_{\text{out,c}})$
- Temperatures of the wall for the three different regions $(T_{w,1}, T_{w,2}$ and $T_{w,3})$

The thermodynamic properties are derived using CoolProp. Design inputs and design outputs of the condenser are shown in Figure 2.5. The design parameters are values of physical parameters of the condenser which can be seen in Table 2.2. The design parameters were not chosen based on any existing plant, but rather based on assumption and trial and error. More details about designing a condenser using the moving boundary technique can be found in [50][54][74].

Power consumed by the fan of the condenser is assumed to be proportional to product of the fan speed and the amount of heat transferred from the working fluid to wall per second.

$$\dot{W}_{\text{fan}} = \frac{1}{2}\left(\dot{m}_{\text{in},c} + \dot{m}_{\text{out},c}\right)\left(h_{\text{in},c} - h_{\text{out},c}\right) k_{\text{fan}} N_{fan}, \tag{2.54}$$

where $k_{\text{fan}} = 1.73 \times 10^{-5}$ is a constant .

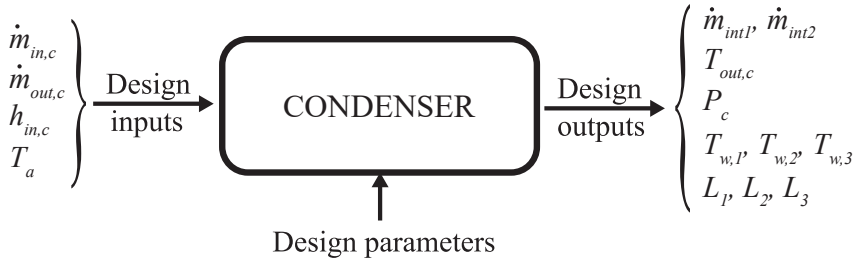

Figure 2.5: Design inputs and outputs for the condenser

Design Parameter	Value
L_c	$40m$
$r_{i,c}$	$11mm$
$r_{o,c}$	$12mm$
c_w	$384J/kg.K$
ρ_w	$8960kg/m^3$

Table 2.2: Design parameters of condenser

2.5.2 Evaporator

The refrigerant is preheated and and is in the supercritical pressure region when it enters the evaporator (represented by the subscript *ev*), *i.e.*, it is in supercritical region inside the evaporator. Therefore, the fluid is assumed not to be in liquid phase nor vapor phase, rather a supercritical fluid which behaves differently than both of the subcritical phases [86]. Thus a single fluid region is assumed for the evaporator and modelled as such in Figure 2.6. This implies, when referring to the general control volume in Figure 2.4, that the boundaries z_A and z_B are fixed for the evaporator design, *i.e.*, $z_{l,A} = 0$ and $z_{l,B} = L_{\text{ev}}$, where L_{ev} is the length of the evaporator. The red arrow in Figure 2.6 represents the heat source bulk temperature. Several assumptions were made for modelling the evaporator (just like the condenser): pressure loss is negligible, the change in kinetic energy and gravitational force are negligible, etc.

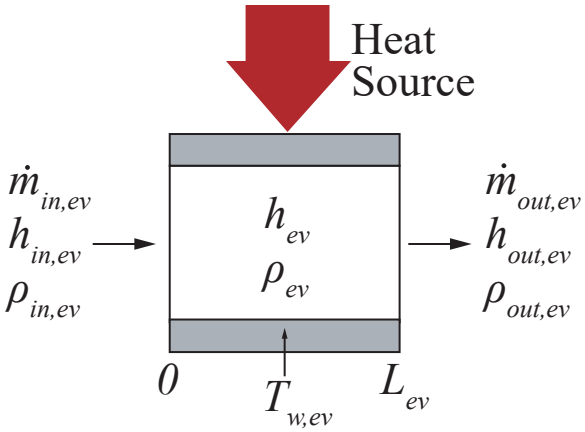

Figure 2.6: Schematic of the evaporator

Now, in the general mass balance equation (2.22) and the general energy balance equation (2.23) for the general control volume, $\frac{dz_{l,A}}{dt} = 0$ and $\frac{dz_{l,B}}{dt} = 0$ since $z_{l,A}$ and $z_{l,B}$ are constants. Therefore, for the evaporator, the following mass balance equation is obtained

$$A_{\text{ev}} \frac{d}{dt} \int_0^{L_{\text{ev}}} \rho_{\text{ev}} dz = \dot{m}_{\text{in,ev}} - \dot{m}_{\text{out,ev}}, \tag{2.55}$$

and, the energy balance equation becomes

$$A_{\text{ev}} \frac{d}{dt} \int_0^{L_{\text{ev}}} \rho_{\text{ev}} h_{\text{ev}} dz - A_{\text{ev}} L_{\text{ev}} \frac{dP_{\text{ev}}}{dt} = \dot{m}_{\text{in,ev}} h_{\text{in,ev}} - \dot{m}_{\text{out,ev}} h_{\text{out,ev}} + \dot{Q}_{\text{in}}, \tag{2.56}$$

where P_{ev} is the evaporating pressure, A_{ev} is the cross-sectional area of the inner tube, ρ_{ev} is the average density of the refrigerant inside the evaporator, h_{ev} is the average enthalpy and is expressed as $h_{\text{ev}} = \frac{h_{\text{in,ev}} + h_{\text{out,ev}}}{2}$, $\dot{m}_{\text{in,ev}}$ is the inlet mass flow rate of the evaporator, $\dot{m}_{\text{out,ev}}$ is the exit mass flow rate of evaporator and $\dot{Q}_{in}$ is the amount of heat transferred from the wall to the working fluid per second and is expressed as

$$\dot{Q}_{\text{in}} = 2\pi r_{i,\text{ev}} L_{\text{ev}} \alpha_{\text{wf,ev}} (T_{w,\text{ev}} - T_{\text{wf,ev}}), \tag{2.57}$$

where $\alpha_{\text{wf,ev}}$ is the heat transfer coefficient between the working fluid and the tube wall, $T_{w,\text{ev}}$ is the average temperature of the tube wall and $T_{\text{wf,ev}}$ is the temperature of refrigerant. The first term

of equation (2.55) can be written as

$$A_{\text{ev}} \frac{d}{dt} \int_0^{L_{\text{ev}}} \rho_{\text{ev}} dz = A_{\text{ev}} L_{\text{ev}} \frac{d\rho_{\text{ev}}}{dt}. \tag{2.58}$$

The time derivative of ρ_{ev} can be expressed by the chain rule

$$\frac{d\rho_{\text{ev}}}{dt} = \frac{d\rho_{\text{ev}}}{dP_{\text{ev}}} \frac{dP_{\text{ev}}}{dt} + \frac{d\rho_{\text{ev}}}{dh_{\text{ev}}} \frac{dh_{\text{ev}}}{dt}. \tag{2.59}$$

Since $h_{\text{ev}} = \frac{h_{\text{in,ev}} + h_{\text{out,ev}}}{2}$, equation (2.59) can be further expressed as

$$\frac{d\rho_{\text{ev}}}{dt} = \frac{d\rho_{\text{ev}}}{dP_{\text{ev}}} \frac{dP_{\text{ev}}}{dt} + \frac{1}{2} \frac{d\rho_{\text{ev}}}{dh_{\text{ev}}} \left(\frac{dh_{\text{in,ev}}}{dt} + \frac{dh_{\text{out,ev}}}{dt} \right), \tag{2.60}$$

where $\frac{dh_{\text{in,ev}}}{dt}$ is a boundary condition imposed by the recuperator. Now putting equation (2.60) into equation (2.58) gives

$$A_{\text{ev}} \frac{d}{dt} \int_0^{L_{\text{ev}}} \rho_{\text{ev}} dz = A_{\text{ev}} L_{\text{ev}} \left[\frac{d\rho_{\text{ev}}}{dP_{\text{ev}}} \frac{dP_{\text{ev}}}{dt} + \frac{1}{2} \frac{d\rho_{\text{ev}}}{dh_{\text{ev}}} \left(\frac{dh_{\text{in,ev}}}{dt} + \frac{dh_{\text{out,ev}}}{dt} \right) \right]. \tag{2.61}$$

Substituting equation (2.61) into equation (2.55) gives the following mass balance equation

$$A_{\text{ev}} L_{\text{ev}} \left[\frac{d\rho_{\text{ev}}}{dP_{\text{ev}}} \frac{dP_{\text{ev}}}{dt} + \frac{1}{2} \frac{d\rho_{\text{ev}}}{dh_{\text{ev}}} \left(\frac{dh_{\text{in,ev}}}{dt} + \frac{dh_{\text{out,ev}}}{dt} \right) \right] = \dot{m}_{\text{in,ev}} - \dot{m}_{\text{out,ev}}. \tag{2.62}$$

Now, the first term of the energy balance equation (2.56) can be expressed as

$$A_{\text{ev}} \frac{d}{dt} \int_0^{L_{\text{ev}}} \rho_{\text{ev}} h_{\text{ev}} dz = A_{\text{ev}} L_{\text{ev}} \rho_{\text{ev}} \frac{dh_{\text{ev}}}{dt} + A_{\text{ev}} L_{\text{ev}} h_{\text{ev}} \frac{d\rho_{\text{ev}}}{dt}. \tag{2.63}$$

Putting equation (2.60) into equation (2.63) gives the following

$$\begin{aligned} A_{\text{ev}} \frac{d}{dt} \int_0^{L_{\text{ev}}} \rho_{\text{ev}} h_{\text{ev}} dz = \frac{1}{2} A_{\text{ev}} L_{\text{ev}} \left(\rho_{\text{ev}} + h_{\text{ev}} \frac{d\rho_{\text{ev}}}{dh_{\text{ev}}} \right) \left(\frac{dh_{\text{in,ev}}}{dt} + \frac{dh_{\text{out,ev}}}{dt} \right) \\ + A_{\text{ev}} L_{\text{ev}} h_{\text{ev}} \frac{d\rho_{\text{ev}}}{dP_{\text{ev}}} \frac{dP_{\text{ev}}}{dt}. \end{aligned} \tag{2.64}$$

Substituting equation (2.64) into equation (2.56) gives the following energy balance equation

$$\frac{1}{2}A_{\text{ev}}L_{\text{ev}}\left(\rho_{\text{ev}}+h_{\text{ev}}\frac{d\rho_{\text{ev}}}{dh_{\text{ev}}}\right)\left(\frac{dh_{\text{in,ev}}}{dt}+\frac{dh_{\text{out,ev}}}{dt}\right)+A_{\text{ev}}L_{\text{ev}}\left(h_{\text{ev}}\frac{d\rho_{\text{ev}}}{dP_{\text{ev}}}-1\right)\frac{dP_{\text{ev}}}{dt}$$
$$=\dot{m}_{\text{in,ev}}h_{\text{in,ev}}-\dot{m}_{\text{out,ev}}h_{\text{out,ev}}+\dot{Q}_{\text{in}}. \tag{2.65}$$

In order to have the outlet temperature of the evaporator ($T_{\text{out,ev}}$) as a state instead of the outlet enthalpy $h_{\text{out,ev}}$, $\frac{dh_{\text{out,ev}}}{dt}$ can be replaced by the following equation

$$\frac{dh_{\text{out,ev}}}{dt}=c_{\text{out,ev}}\frac{dT_{\text{out,ev}}}{dt}, \tag{2.66}$$

where $c_{\text{out,ev}}$ is the specific heat capacity of the refrigerant at the outlet of the evaporator. Now substituting equation (2.66) into equation (2.62), the following final mass balance equation for the evaporator is obtained

$$A_{\text{ev}}L_{\text{ev}}\left[\frac{d\rho_{\text{ev}}}{dP_{\text{ev}}}\frac{dP_{\text{ev}}}{dt}+\frac{1}{2}\frac{d\rho_{\text{ev}}}{dh_{\text{ev}}}\left(\frac{dh_{\text{in,ev}}}{dt}+c_{\text{out,ev}}\frac{dT_{\text{out,ev}}}{dt}\right)\right]=\dot{m}_{\text{in,ev}}-\dot{m}_{\text{out,ev}}. \tag{2.67}$$

Similarly, substituting equation (2.66) into equation (2.65), the following final energy balance equation for the evaporator is obtained

$$\frac{1}{2}A_{\text{ev}}L_{\text{ev}}\left(\rho_{\text{ev}}+h_{\text{ev}}\frac{d\rho_{\text{ev}}}{dh_{\text{ev}}}\right)\left(\frac{dh_{\text{in,ev}}}{dt}+c_{\text{out,ev}}\frac{dT_{\text{out,ev}}}{dt}\right)+A_{\text{ev}}L_{\text{ev}}\left(h_{\text{ev}}\frac{d\rho_{\text{ev}}}{dP_{\text{ev}}}-1\right)\frac{dP_{\text{ev}}}{dt}$$
$$=\dot{m}_{\text{in,ev}}h_{\text{in,ev}}-\dot{m}_{\text{out,ev}}h_{\text{out,ev}}+\dot{Q}_{\text{in}}. \tag{2.68}$$

The energy balance of the wall of the evaporator can be written as follows

$$c_w\rho_w A_{w,\text{ev}}\frac{dT_{w,\text{ev}}}{dt}=2\pi r_{i,\text{ev}}\alpha_{\text{wf},ev}(T_{\text{wf},ev}-T_{w,\text{ev}})+2\pi r_{o,\text{ev}}\alpha_{o,\text{ev}}(T_{\text{sf}}-T_{w,\text{ev}}), \tag{2.69}$$

where $\alpha_{o,\text{ev}}$ is the heat transfer coefficient between the heat source and the wall and T_{sf} is the bulk temperature of the heat source. It is important to note that the dynamics of the heat source are not considered for this work. The bulk temperature of the heat source acts as a disturbance to the system.

Using the mass balance and energy balance equations (2.67), (2.68) and (2.69) obtained above, a three-state order model is established for the evaporator with the following states:

- Evaporating pressure (P_{ev})
- Outlet temperature of the refrigerant $(T_{\text{out,ev}})$
- Temperature of the wall $(T_{w,\text{ev}})$

The thermodynamic properties are derived using CoolProp. Design inputs and design outputs of the condenser are shown in Figure 2.7. Design parameters are values of physical parameters of the evaporator which can be seen in Table 2.3. The design parameters were not chosen based on any existing plant, but rather based on assumption and trial and error.

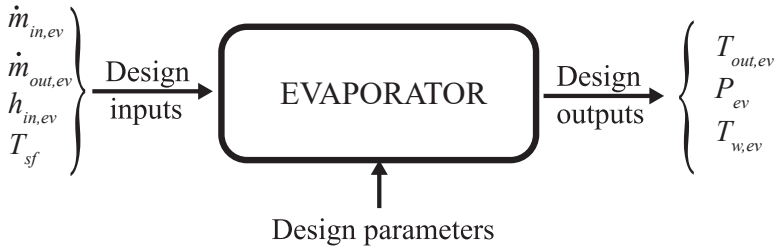

Figure 2.7: Design inputs and outputs for the evaporator

Design Parameter	Value
L_{ev}	$40m$
$r_{i,\text{ev}}$	$11mm$
$r_{o,\text{ev}}$	$12mm$
$R_{i,\text{ev}}$	$55mm$
c_w	$384J/kg.K$
ρ_w	$8960kg/m^3$

Table 2.3: Design parameters of evaporator

2.5.3 Recuperator

Modelling the recuperator (represented by the subscript r) is slightly different than that of the evaporator, mainly because the refrigerant flows through both side of the recuperator (*i.e.* the cold side refrigerant, denoted by the subscript c, and the hot side refrigerant, denoted by the subscript h) having mutual heat exchange within the cycle. This is illustrated in the schematic of the recuperator as shown in Figure 2.8. Similar assumptions are made for the recuperator modelling as were made for the evaporator, with an additional assumption - the pressure dynamics are ignored on both sides, i.e., $\frac{dP}{dt} = 0$. Because of the new assumption, the pressure on the cold side and hot side are imposed by the evaporating pressure and the condensing pressure respectively. This is illustrated in a clear manner in Figure 1.2, where it can be seen that the cycle has been divided into a high pressure side and a low pressure side, where high pressure and low pressure are the result of the evaporator and the condenser dynamics respectively. Note that in Figure 1.2, (2-3) is the cold side of the recuperator because of its lower temperature compared to the hot side (6-7) of the recuperator.

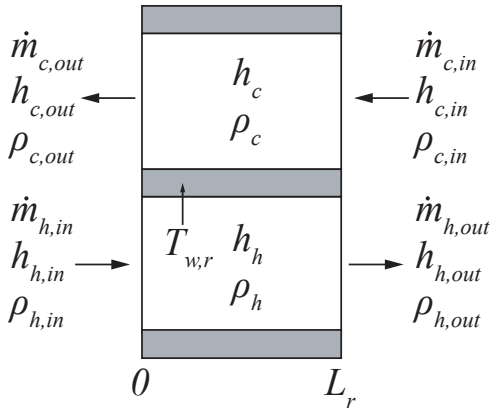

Figure 2.8: Schematic of the recuperator

The refrigerant is above the supercritical pressure in the cold side of the recuperator, therefore, the fluid is assumed not to be neither in liquid phase nor in vapor phase, rather it is a supercritical fluid. In the hot side of the recuperator, the refrigerant is in vapor phase. Thus a single fluid region is assumed for the recuperator on both sides of the recuperator and modelled as such as shown in Figure 2.8. This implies, when referring to the general control volume in Figure 2.4, that the boundaries $z_{l,A}$ and $z_{l,B}$ are fixed for the recuperator design, *i.e.*, $z_{l,A} = 0$ and $z_{l,B} = L_r$, where L_r is the length of the recuperator. It is also assumed that the cold refrigerant flows through the inner tube of the recuperator and the hot refrigerant flows through the outer tube of the recuperator.

Now, in the general energy balance equation (2.23) for the general control volume, $\frac{dz_{l,A}}{dt} = 0$ and $\frac{dz_{l,B}}{dt} = 0$ since z_A and z_B are constants. Therefore, for the recuperator, the following general energy balance equation is obtained

$$A_r \frac{d}{dt} \int_0^{L_r} \rho_r h_r dz = \dot{m}_{\text{in},r} h_{\text{in},r} - \dot{m}_{\text{out},r} h_{\text{out},r} + \dot{Q}_r, \tag{2.70}$$

where A_r is the cross-sectional area, ρ_r is the average density of the refrigerant, h_r is the average enthalpy and is expressed as $h_r = \frac{h_{\text{in},r} + h_{\text{out},r}}{2}$, $\dot{m}_{\text{in},r}$ is the inlet mass flow rate of the evaporator, $\dot{m}_{\text{out},r}$ is the exit mass flow rate of evaporator and $\dot{Q}_r$ is the amount of heat transferred from or to the wall. The time derivative for ρ_c can be expressed by the chain rule

$$\frac{d\rho_c}{dt} = \frac{d\rho_c}{dh_c}\frac{dh_c}{dt}. \tag{2.71}$$

Since $h_c = \frac{h_{c,\text{in}}+h_{\text{c,out}}}{2}$, equation (2.71) can be further expressed as

$$\frac{d\rho_c}{dt} = \frac{1}{2}\frac{d\rho_c}{dh_c}\left(\frac{dh_{c,\text{in}}}{dt} + \frac{dh_{c,\text{out}}}{dt}\right). \tag{2.72}$$

For the cold side, equation (2.70) can be written as

$$A_{i,r}L_r h_c\frac{d\rho_c}{dt} + A_{i,r}L_r\rho_c\frac{dh_c}{dt} = \dot{m}_{c,\text{in}}h_{c,\text{in}} - \dot{m}_{\text{c,out}}h_{c,\text{out}} + \dot{Q}_{\text{in},r}, \tag{2.73}$$

where $\dot{Q}_{\text{in,r}}$ is the amount of heat transferred from the wall to the cold side of the working fluid per second and is expressed as the following:

$$\dot{Q}_{\text{in},r} = 2\pi r_{i,r}L_r\alpha_{\text{wf},c,r}(T_{w,r} - T_{\text{wf},c,r}), \tag{2.74}$$

where $\alpha_{\text{wf},c,r}$ is the heat transfer coefficient between the cold side refrigerant and the tube wall, $T_{w,r}$ is the average temperature of the tube wall and $T_{\text{wf},c,r}$ is the temperature of refrigerant in the cold side. Using the relation $h_c = \frac{h_{c,\text{in}}+h_{\text{c,out}}}{2}$ and substituting equation (2.72) into equation (2.73), the following final energy balance for cold side can be obtained

$$\begin{aligned}\frac{1}{2}A_{i,r}L_r\left[\frac{1}{2}\left(h_{c,\text{in}}+h_{c,\text{out}}\right)\frac{d\rho_c}{dh_c}+\rho_c\right]\left(\frac{dh_{c,\text{in}}}{dt}+\frac{dh_{c,\text{out}}}{dt}\right)\\ = \dot{m}_{c,\text{in}}h_{c,\text{in}} - \dot{m}_{c,\text{out}}h_{c,\text{out}} + \dot{Q}_{\text{in},r}.\end{aligned} \tag{2.75}$$

For the hot side of the recuperator, using similar procedure for the cold side, the following final energy balance equation can be obtained

$$\frac{1}{2}A_{o,r}L_r\left[\frac{1}{2}\left(h_{h,\text{in}}+h_{h,\text{out}}\right)\frac{d\rho_h}{dh_h}+\rho_c\right]\left(\frac{dh_{\text{h,in}}}{dt}+\frac{dh_{h,\text{out}}}{dt}\right)$$
$$=\dot{m}_{h,\text{in}}h_{h,\text{in}}-\dot{m}_{h,\text{out}}h_{h,\text{out}}-\dot{Q}_{\text{out,r}}, \tag{2.76}$$

where $\dot{Q}_{\text{out,r}}$ is the amount of heat transferred from the the hot side of the working fluid to the wall per second and is expressed as:

$$\dot{Q}_{\text{out},r}=2\pi r_{o,r}L_r\alpha_{\text{wf},h,r}(T_{\text{wf},h,r}-T_{\text{w,r}}), \tag{2.77}$$

where $\alpha_{\text{wf},h,r}$ is the heat transfer coefficient between the hot side refrigerant and the tube wall and $T_{\text{wf},h,r}$ is the temperature of refrigerant in the hot side.

The wall energy balance for the recuperator is as follows:

$$c_w A_{\text{w,r}}L_r\rho_w\frac{dT_{\text{w,r}}}{dt}=\dot{Q}_{\text{out},r}-\dot{Q}_{\text{in},r}. \tag{2.78}$$

Using the energy balance equations (2.75), (2.76) and (2.78) obtained above, a three-state order model is established for the recuperator with the following states:

- Outlet enthalpy of the cold side $(h_{c,\text{out}})$
- Outlet enthalpy of the hot side $(h_{h,\text{out}})$
- Temperature of the wall $(T_{w,r})$

The thermodynamic properties are derived using CoolProp. Design inputs and design outputs of the condenser are shown in Figure 2.9. Design parameters are values of physical parameters of the recuperator which can be seen in Table 2.4. The design parameters were not chosen based on any existing plant, but rather based on assumption and trial and error.

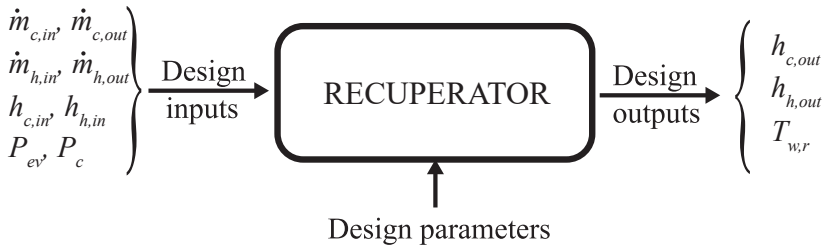

Figure 2.9: Design inputs and outputs for the recuperator

Design Parameter	Value
L_r	$10m$
$r_{i,r}$	$11mm$
$r_{o,r}$	$12mm$
$R_{i,r}$	$40mm$

Table 2.4: Design parameters of recuperator

2.6 Fast dynamics components

The pump, expander, and valve constitute the fast dynamics, since their time constants are so much lower compared to the heat exchangers [81][47]. In order to have the simulation work as fast as possible while still capturing the essential dynamics, these three components are modelled with static algebraic relationships. The pump and the valve act as actuators for the ORC.

2.6.1 Pump

The pump has a maximum limit of volume of fluid it can pump out per second, termed as the maximum volumetric flow rate $\dot{V}_{\max}$. Thus, a term called the capacity fraction of the pump X_{pp} is defined as the actuating value for the pump. It is the ratio between the actual volumetric flow rate $\dot{V}_{\text{pump}}$ to the maximum volumetric flow rate [81], as defined by the following equation

$$X_{\text{pp}} = \frac{\dot{V}_{\text{pump}}}{\dot{V}_{\text{max}}}. \tag{2.79}$$

Thus, the actuating value of the pump is limited by $0 \leq X_{\text{pp}} \leq 1$, where $X_{\text{pp}} = 0$ means that the pump is not working at all and $X_{\text{pp}} = 1$ means the pump is working at its full capacity. The pump is electronically controlled, *i.e.*, X_{pp} is an electronic signal passed as an input to the ORC.

Two algebraic equations are used to model the pump in order to have the required outputs imposed by the pump in an ORC. Firstly, the mass flow rate imposed by the pump is a function of its capacity fraction given by the following relation

$$\dot{m}_{\text{pump}} = \dot{V}_{\text{pump}} \rho_{\text{pump}} X_{\text{pp}}, \tag{2.80}$$

where ρ_{pump} is the density of refrigerant at the inlet of the pump. The refrigerant is assumed to be incompressible in its liquid form and thus density is assumed equal at the inlet and the outlet of the pump. Secondly, the outlet enthalpy of the pump is given by the following relation

$$h_{\text{out,pump}} = h_{\text{in,pump}} + \frac{\left(P_{\text{out,pump}} - P_{\text{in,pump}}\right)}{\eta_{\text{pump}} \rho_{\text{pump}}}, \tag{2.81}$$

where $h_{\text{in,pump}}$ and $P_{\text{in,pump}}$ are the inlet enthalpy and pressure of the pump respectively, $P_{\text{out,pump}}$ is the outlet pressure of the pump and η_{pump} is the pump efficiency coefficient usually provided by the pump performance curve. It is important to note that the inlet and outlet pressures of the pump are imposed by the dynamics of the condenser and the evaporator respectively. Power input to the pump can be calculated using the following relation

$$\dot{W}_{\text{pump}} = \dot{m}_{\text{pump}} (h_{\text{out,pump}} - h_{\text{in,pump}}). \tag{2.82}$$

The thermodynamic properties are derived using CoolProp. Design inputs and design outputs of the pump are shown in Figure 2.10. Design parameters are values of physical parameters of the pump which can be seen in Table 2.5. The design parameters were not chosen based on any

existing plant, but rather based on assumption and trial and error.

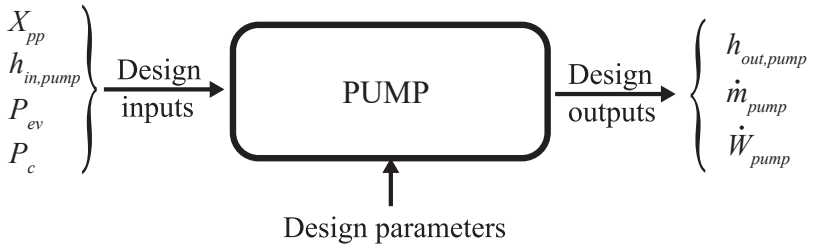

Figure 2.10: Design inputs and outputs for the pump

Design Parameter	Value
$\dot{V}_{\max}$	$1.4 \times 10^{-3} m^3/s$
η_{pump}	0.6001

Table 2.5: Design parameters of pump

2.6.2 Expander

The model for the expander is defined by its isentropic effectiveness (ε) usually provided by the expander performance curve. Since outlet enthalpy is the only aspect of the expander that matters for modelling purposes, a single algebraic equation is sufficient to model the expander. The following equation gives the output enthalpy for the expander

$$h_{\text{out,exp}} = h_{\text{in,exp}} - (h_{\text{in,exp}} - h_{\text{out,is}})\varepsilon, \tag{2.83}$$

where $h_{\text{in,exp}}$ is the inlet enthalpy of the expander and $h_{\text{out,is}}$ is the outlet enthalpy of the expander if the process was isentropic. The power output of the expander can be obtained from the following equation

$$\dot{W}_{\text{exp}} = \dot{m}_{\text{exp}}(h_{\text{out,exp}} - h_{\text{in,exp}}), \tag{2.84}$$

where $\dot{m}_{\text{exp}}$ is the mass flow rate of the refrigerant inside the expander imposed by the valve.

The thermodynamic properties are derived using CoolProp. Design inputs and design outputs of the expander are shown in Figure 2.11. The only design parameter that was required for the modelling was the isentropic effectiveness which was chosen to be 0.6163.

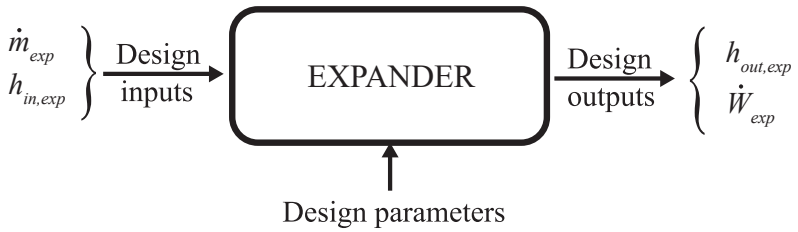

Figure 2.11: Design inputs and outputs for the expander

2.6.3 Valve

The valve acts as an actuator to the ORC and modulates the mass flow rate by changing the throttle valve position electronically [106]. It is assumed that it has negligible effect on the enthalpy or pressure of the refrigerant. So the only output that is of interest for this work is the mass flow rate which can be obtained by the following relation

$$\dot{m}_v = \beta_v \mu \frac{P_{\text{ev}}}{\sqrt{T_{\text{out,ev}}}}, \tag{2.85}$$

where β_v is a constant coefficient and μ is the opening of the valve. The value of μ is limited between 0 and 1, where $\mu = 0$ indicates that the valve is fully closed and $\mu = 1$ indicates that the valve is fully open. The design parameter β_v is chosen 3×10^{-6}. Design inputs and outputs of the expander are shown in Figure 2.12. Note that in a traditional boiler-turbine system, the valve position is treated as a load on the system and not as an MV (control input). When generating power using alternative energy sources, however, the task is to provide as much power 'as possible' to the larger grid rather than meeting a specific demand.

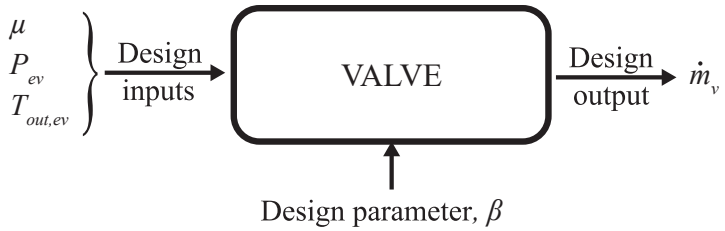

Figure 2.12: Design inputs and output for the valve

2.7 Model validation

As mentioned earlier, the design parameters for the components were chosen based on assumption and trial and error. There was no real data to validate the model with an actual plant, nor there were component specifications available from a real plant. Therefore, an alternate solution is proposed for model validation for this thesis. The solution is to observe the change in some of the core dynamics of the ORC with respect to changes in the actuator inputs. The changes are then compared to changes observed by [81].

In order to validate the model in the proposed way, step changes are made in the actuator inputs. First, a step change in the opening of the valve (μ) is made from 0.4 to 0.45 at 30s. The changes in the evaporating pressure and the outlet temperature of the evaporator are shown in Figure 2.13. It can be noticed that a step up in μ decreases both evaporating pressure and outlet temperature at the evaporator from a steady state value, *i.e.* both the outputs have a negative gain relation with μ. The same can be observed in [81].

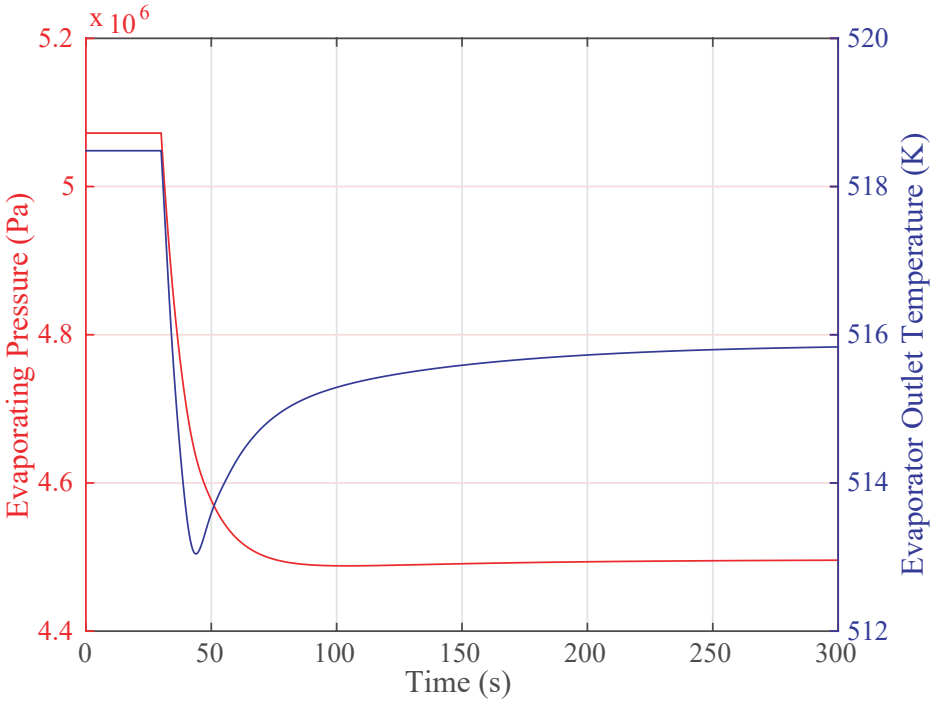

Figure 2.13: Step change in μ from 0.4 to 0.45

Secondly, a step change in the capacity fraction of the pump (X_{pp}) is made from 0.4 to 0.45 at 30s. The changes in the evaporating pressure and the outlet temperature of the evaporator are shown in Figure 2.14. It can be seen that a step up in X_{pp} decreases outlet temperature at the evaporator from a steady state value *i.e.* it has a negative gain relation with X_{pp}. Meanwhile, the evaporating pressure increases from a steady state value *i.e.* it has a positive gain relation with X_{pp}. The same gain relationships can be observed in [81].

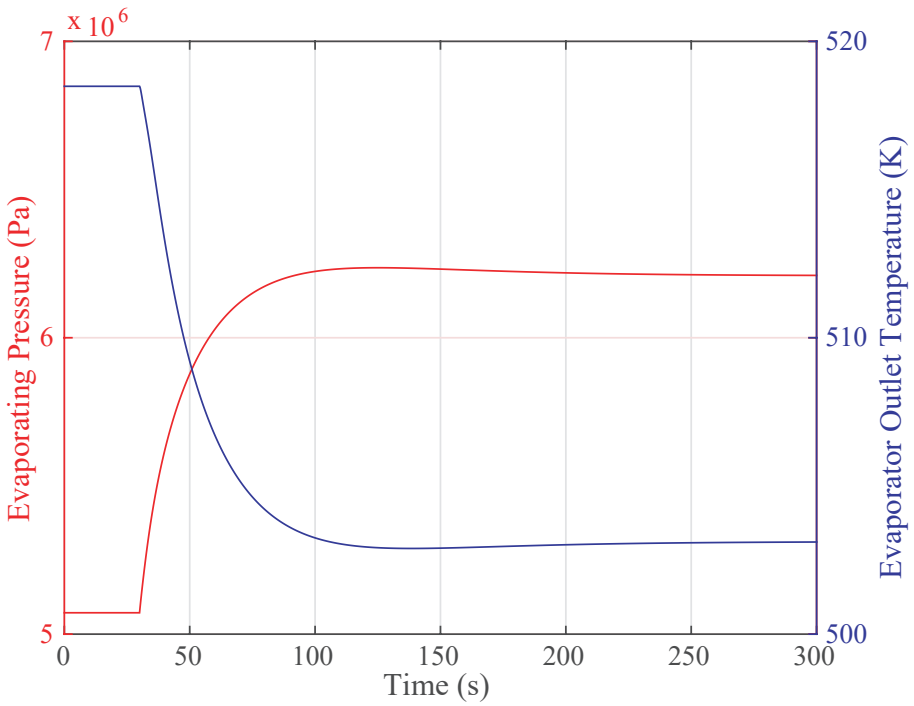

Figure 2.14: Step change in X_{pp} from 0.4 to 0.45

Finally, a step change in the fan speed (N_{fan}) is made from $300rpm$ to $500rpm$ at $30s$. The changes in the evaporating pressure and the outlet temperature of the evaporator are negligible. However, the change in the outlet temperature of the refrigerant of the condenser is significant. From Figure 2.15, it can be seen that a step up in N_{fan} decreases outlet temperature at the condenser from a steady state value *i.e.* it has a negative gain relation with N_{fan}. This makes intuitive sense: we expect the fan to create cooling.

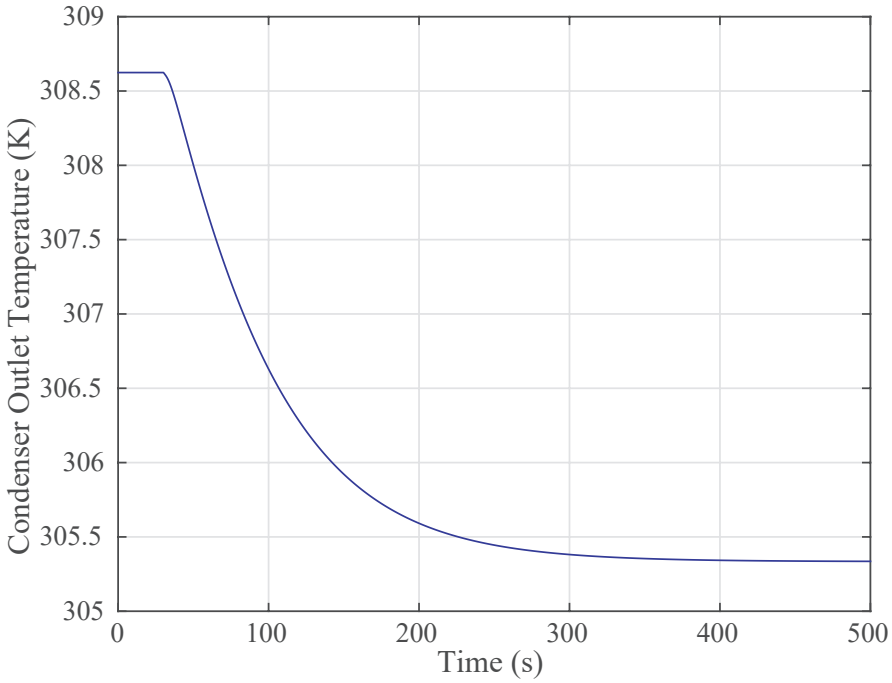

Figure 2.15: Step change in N_{fan} from $300rpm$ to $500rpm$

2.8 Summary

In summary, each of the components of the ORC are modelled by classifying the components into two main categories - fast dynamics components and slow dynamics components. The three heat exchangers are dynamically dominant over the other three components; therefore only the heat exchangers' dynamics were considered. The fast dynamics components were modelled with static algebraic relations. Overall, a thirteen order state model is established for the ORC, among which seven states are from the condenser and three states from each of the other two heat exchangers.

Chapter 3

Control development

After having developed the model for the ORC, the next task is to develop a control system to track the set point while remaining robust to disturbances (note that large steady-state changes to the input heat source will require a change in set point if optimal operation is to be maintained, but the control system should remain robust to small heat variations that occur without a set point change). The objective is to develop a control system that does not need an accurate model of the system. Not only do multi-input, multi-ouput (MIMO) control systems generally require an accurate model of the system, they are also based on linearizations that have questionable accuracy for such a highly nonlinear system such as ORC. Thus, first the system is shown to be approximated by three independent single-input single-output (SISO) systems. This makes decentralized PID (or PI) control possible. It also makes possible the application of approximate adaptive controls such as CMAC, that can adapt to an unknown model, remain robust to time-varying disturbances, and compensate for nonlinearities.

3.1 Control Strategy for determining set-points

In [108], Zhang et al. suggests two general strategies for ORC based waste heat recovery systems - FEL (following the electric load) and FWH (following the waste heat). In FEL mode, the objective is like those of conventional waste heat power plants, where the task for the ORC is to generate power by meeting the demand in variation of electric load demand while keeping ORC process

variables within safe operating limits. The second strategy, FWH mode, targets in utilizing the waste heat efficiently by following the variations of the waste heat so as to guarantee maximum power generation while keeping ORC process variables within safe operating limits. Zhang et al. uses FEL mode for their work [108] while Sylvain et al. uses FWH mode as their operation strategy for designing control for ORC cycle [82]. For this thesis, FWH mode is chosen since waste heat recovery units in industries are usually used as auxiliary power units and are desired to have maximum net power in the output. The net power is

$$\dot{W}_{\text{net}} = \dot{W}_{\text{exp}} - \dot{W}_{\text{pump}} - \dot{W}_{\text{fan}}. \tag{3.1}$$

The process variables (i.e. the CVs) chosen for this thesis which have effect on the objective function (the net work, $\dot{W}_{\text{net}}$) and are safety concerns, are the outlet temperature of the working fluid at the evaporator $(T_{\text{out,ev}})$, the evaporating pressure (P_{ev}), and the outlet temperature of the working fluid at the condenser $(T_{\text{out,c}})$. For an SORC in [82], Sylvain et al. uses an algebraic relation to update the optimal evaporating temperature $(T_{\text{ev,opt}})$ with respect to changes in the waste heat source temperature (T_{sf}) and its mass flow rate $(\dot{m}_{\text{sf}})$ and condensing temperature (T_c). Using the algebraic relation provided, changes in T_{ev} is observed with respect to changes in T_{sf}, keeping $\dot{m}_{\text{sf}} = 0.15 kg/s$ and $T_c = 30^0 C$ as constants and is shown in Figure 3.1, which shows that with increasing T_{sf}, $T_{\text{ev,opt}}$ also increases. However, it is important to understand the complexity involved in evaluating the performance of a TORC compared to that of a SORC. In an SORC, as shown in the temperature-entropy profile in Figure 1.3, the heat exchange process inside the evaporator (3-4') involves a phase change (a-b) where the evaporating temperature (T_{ev}) is constant for a particular evaporating pressure (P_{ev}). Whereas, in a TORC, as shown in the temperature-entropy profile in Figure 1.3, the heat exchange process inside the evaporator (3-4) does not have a phase change; rather the refrigerant is in supercritical phase. Hence no constant T_{ev} is involved in the process for a particular P_{ev}. For a SORC, [36] and [81] showed that higher efficiency is achieved when superheating of the refrigerant is avoided and expanded directly from the dew line (b-6'), and thus the objective was to optimize the cycle using the variable T_{ev}. But such a point

does not exist in a TORC and thus it becomes complex.

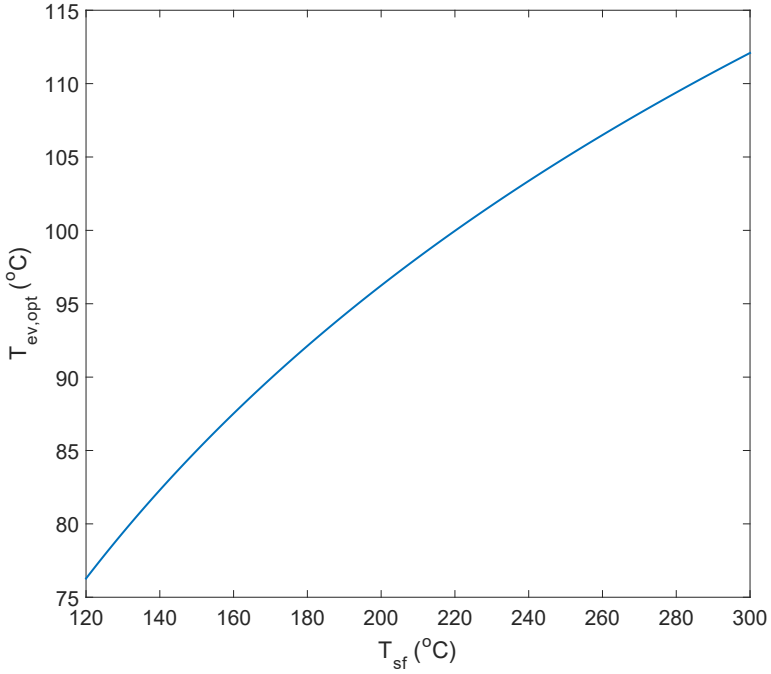

Figure 3.1: Changes in $T_{\text{ev,opt}}$ with respect to changes in T_{sf} for a SORC

For a TORC, $T_{\text{out,ev}}$ is rather chosen instead of $T_{\text{ev,opt}}$ as a replacement. Using a static model, which is basically the dynamic model described in Chapter 2 with all its time derivatives set to zero, changes in $\dot{W}_{\text{net}}$, P_{ev}, $T_{\text{out,ev}}$ and $T_{\text{out,c}}$ with respect to changes in T_{sf} $(175^0\text{C} \leq T_{\text{sf}} \leq 235^0\text{C})$ is obtained. The change in T_{sf} and its effect on $\dot{W}_{\text{net}}$ is shown in Figure 3.2 which suggests increase in $\dot{W}_{\text{net}}$ with increasing T_{sf} and vice versa. The changes in the process variables P_{ev}, $T_{\text{out,ev}}$ and $T_{\text{out,c}}$ can also be seen in Figure 3.3, Figure 3.4 and Figure 3.5 respectively. The graphs suggests that with increasing T_{sf}, P_{ev} and $T_{\text{out,ev}}$ must increase while $T_{\text{out,c}}$ must decrease in order for increase in $\dot{W}_{\text{net}}$. However, there are safety limits for process variables in a TORC which must be maintained for proper functioning of TORC and thus must have bounds on the process variables. For this thesis, the upper bounds for P_{ev} and $T_{\text{out,ev}}$ are arbitrarily chosen to be 5MPa and 245°C, and the lower bound for $T_{\text{out,c}}$ is chosen to be 30°C, and these are the set-points (sp) the controller must be able to track while utilizing the heat source temperature to its maximum capability. Note that the changes in $T_{\text{out,ev}}$ in a TORC is similar to changes in $T_{\text{ev,opt}}$ in a SORC with respect to changes in

T_{sf} (see Figure 3.4 and Figure 3.1).

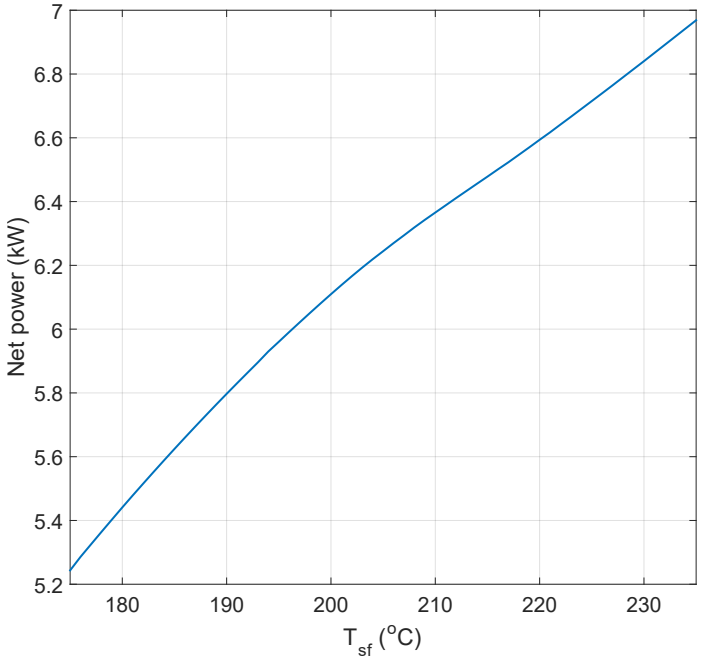

Figure 3.2: $\dot{W}_{net}$ against changes in T_{sf} for TORC

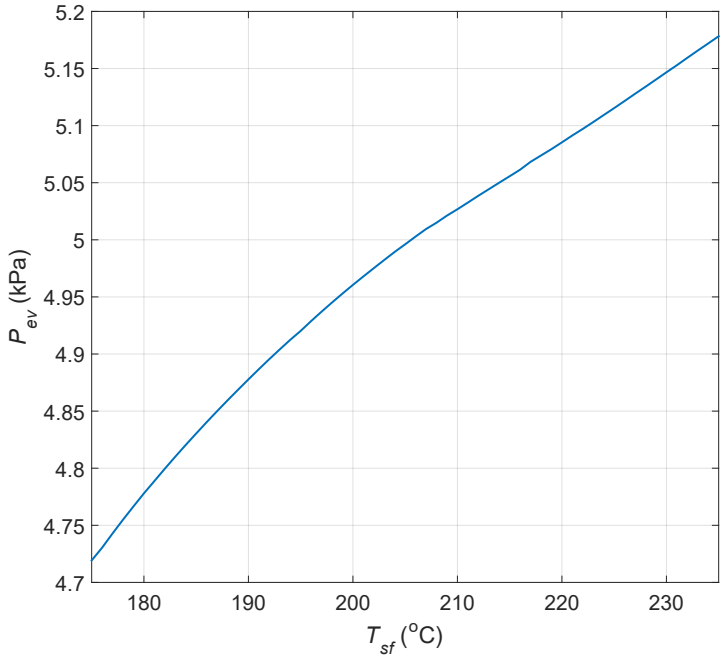

Figure 3.3: P_{ev} against changes in T_{sf} for TORC

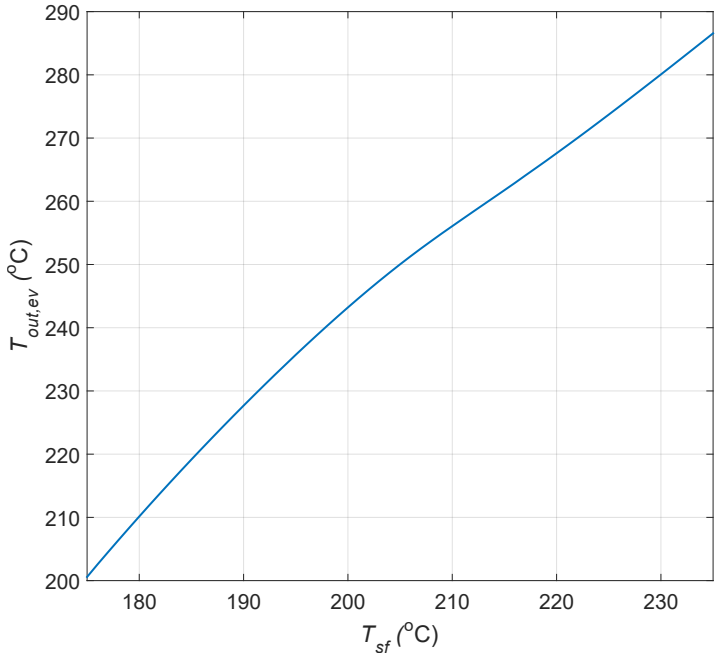

Figure 3.4: $T_{\text{out,ev}}$ against changes in T_{sf} for TORC

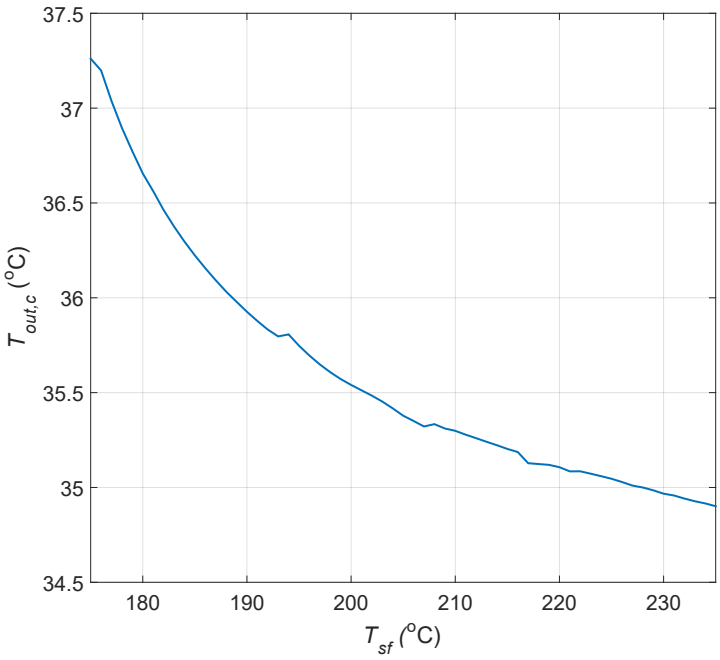

Figure 3.5: $T_{\text{out,c}}$ against changes in T_{sf} for TORC

3.2 Relative Gain Array (RGA) analysis

The majority of plants in the real world can be described as MIMO systems, but SISO control strategies are much easier to implement [76]. In the SISO strategy, only one manipulated variable (MV) is used to control one controlled variable (CV). There is always some degree of interaction between the SISO loops, and an approximate measure of the interactions between the loops is desired. The Relative Gain Array (RGA) analysis, first introduced by Bristol [20], provides such a measure. It identifies the control structure by identifying the degree of process interactions between the CVs and the MVs [20][26], thus providing a method for obtaining a decoupled system.

There are few basic rules which need to be followed in order to establish the correct pairings between the CVs and the MVs. The rules are as follows [93]:

1. Pairings which have values closest to one should be chosen.

2. Pairings which correspond to negative values should be avoided.

Table 3.1 shows transfer functions obtained using the System Identification toolbox in MATLAB by using data collected from the simulations of the TORC system. The transfer functions are a means of observing the interactions between the MVs and the CVs which are used to calculate the RGA matrix. The System Identification toolbox also provides with the percentage fit to estimation data which are shown in Table 3.2.

	μ	X_{pp}	N_{fan}
P_{ev}	$\frac{-1.1548\times10^{7}}{(1+10.011s)}$	$\frac{2.2803\times10^{7}}{(1+15.979s)}$	$\frac{309.26}{(1+79.587s)}$
$T_{\text{out,ev}}$	$\frac{-52.604}{1+30.5842s+304.3629s^{2}}$	$\frac{-307.94}{(1+19.461s)}$	$\frac{0.0071763}{(1+18.167s)}$
$T_{\text{out},c}$	$\frac{-17.624}{(1+93.441s)}$	$\frac{148.88}{(1+57.06s)}$	$\frac{-0.016544}{1+69.323s}$

Table 3.1: Transfer functions estimated using MATLAB showing relations between the MVs and CVs

	μ	X_{pp}	N_{fan}
P_{ev}	94.93	92.06	94.31
$T_{\text{out,ev}}$	66.01	93.84	90.36
$T_{\text{out},c}$	91.12	89.56	96.72

Table 3.2: Percentage fit to estimation data between MVs and CVs

The following 3×3 RGA matrix (Λ) is calculated using MATLAB code [93]:

$$\Lambda = \begin{bmatrix} & \mu & X_{\text{pp}} & N_{\text{fan}} \\ P_{\text{ev}} & 0.63409 & 0.30998 & 0.055922 \\ T_{\text{out,ev}} & 0.30368 & 0.82525 & -0.12894 \\ T_{\text{out},c} & 0.062223 & -0.13524 & 1.073 \end{bmatrix}. \tag{3.2}$$

The RGA matrix shows that it is diagonally dominant. It also abides by the summation property of a RGA matrix, *i.e.*, any row or column sums to one [20]. Using the rules mentioned earlier, it can be concluded that the opening of the valve (μ) has more interaction with the pressure at the evaporator (P_{ev}), while the capacity fraction of the pump (X_{pp}) has more interaction with the outlet temperature of the refrigerant at the evaporator $(T_{\text{out,ev}})$. By intuition and educated guess, it was expected for the speed of the fan (N_{fan}) to have the highest interaction with the outlet temperature of the condenser $(T_{\text{out,c}})$, and that is what the RGA matrix confirms. Therefore, the following pairs are established for the purpose of designing a SISO controller:

$$\mu \rightarrow P_{\text{ev}}$$

$$X_{\text{pp}} \rightarrow T_{\text{out,ev}}$$

$$N_{\text{fan}} \rightarrow T_{\text{out},c}$$

Interested readers can go through [93] to learn in details about RGA analysis.

3.3 Proportional, Integral, Derivative (PID) control

It is important to establish the conventional PID controller in order to evaluate the performance of other control schemes. The PID is broadly applicable as it can be implemented based on measured process variables only without having any knowledge of the concealed process behavior.

In PID, the proportional term accounts for the present error, the integral term accounts for the past error, and the derivative term accounts for the future error [11]. The PID control scheme is represented by the following summation equation of three individual terms:

$$u(t) = K_p e(t) + K_i \int_0^t e(\tau) d\tau + K_d \frac{d}{dt} e(t),$$

where u is the MV, error e is the difference between the set point (sp) and the CV, K_p, K_i, and K_d are control gains (tuning parameters) known as the proportional gain, integral gain and derivative gain respectively, t is the present time and τ takes on values from time 0 to t. Note that the above equation for PID is in its parallel form. Figure 3.6 shows a block diagram of a typical PID controller $C(s)$ implementation for a plant $G(s)$ trying to track a reference signal $R(s)$.

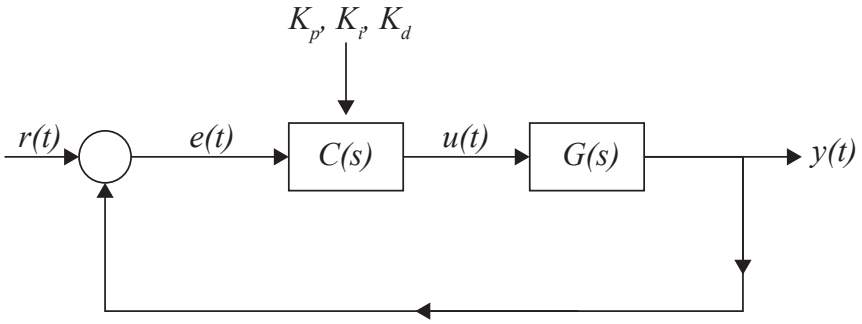

Figure 3.6: Closed-loop PID control

Several techniques have been established in order to calculate the control gains for a particular system. The most commonly used techniques are Ziegler-Nichols (ZN) and Internal Model Control (IMC). For this work IMC technique has been used. Using ZN technique for tuning PI controller for a heat exchanging processes is a poor choice and can be 18 times slower compared to the IMC

tuning technique [48]. It is important to note that some processes may require only one or two of the gains in order to yield a suitable control (setting the other gains to zero). Thus, a PID controller can be termed as PI, PD, or P controller in the absence of the respective control actions. Derivative terms are often avoided due to the sensitivity of the derivative term to measurement noise. The integral term eliminates steady-state error for stable controllers for a constant input. For this work, PI controllers are used.

From Table 3.1, it can be noted that the pairings $X_{\text{pp}} \rightarrow T_{\text{out,ev}}$, $\mu \rightarrow P_{\text{ev}}$ and $N_{\text{fan}} \rightarrow T_{\text{out,c}}$ exhibit first-order processes. Parameter tuning using IMC techniques for a first-order processes is utilized here [17].

3.3.1 IMC technique for first-order process

A first-order process is defined by the following

$$G(S) = \frac{k_p}{\tau_p S + 1}. \tag{3.3}$$

First, find the IMC controller transfer function $q(S)$

$$q(s) = G^{-1}(S) f(S) = \frac{\tau_p S + 1}{k_p} f(s), \tag{3.4}$$

where $f(S)$ is a filter to make $q(S)$ semi proper and is defined by

$$f(S) = \frac{1}{\lambda_f S + 1}, \tag{3.5}$$

where λ_f is a constant chosen to trade-off between performance and robustness.
Substituting equation (3.5) into equation (3.4) gives

$$q(S) = \frac{\tau_p S + 1}{k_p(\lambda_f S + 1)}. \tag{3.6}$$

The following transformation is suggested by [17] in order to find the equivalent standard feedback

controller

$$C(S) = \frac{q(S)}{1 - G(S)q(S)}. \tag{3.7}$$

Putting equation (3.3) and equation (3.6), equation (3.7) is simplified into

$$\begin{aligned} C(S) &= \frac{\tau_p S + 1}{k_p \lambda_f S} \\ \Rightarrow C(S) &= \frac{\tau_p}{\tau_p} \left(\frac{\tau_p S + 1}{k_p \lambda_f S} \right) \\ \Rightarrow C(S) &= \frac{\tau_p}{k_p \lambda_f} \left(\frac{\tau_p S + 1}{\tau_p S} \right). \end{aligned} \tag{3.8}$$

Now, the transfer function for a PI controller in its standard form is

$$C(S) = K_p \left(\frac{\tau_I S + 1}{\tau_I S} \right). \tag{3.9}$$

Equating equation (3.8) and equation (3.9),

$$K_p = \frac{\tau_p}{k_p \lambda_f} \tag{3.10}$$

$$\tau_I = \tau_p. \tag{3.11}$$

Therefore,

$$K_i = \frac{K_P}{\tau_I}. \tag{3.12}$$

The derivative gain K_d is set to zero, creating a PI controller. The proportional gain K_p and integral gain K_i are calculated for each of the established pairings (Table 3.3) using the first-order processes identified (Table 3.1).

	λ_f	K_p	K_i
$\mu \rightarrow P_{\text{ev}}$	0.5	-1.734×10^{-6}	-1.732×10^{-7}
$X_{\text{pp}} \rightarrow T_{\text{out,ev}}$	0.5	-0.1215	-0.0062
$N_{\text{fan}} \rightarrow T_{\text{out,c}}$	0.5	-7505	-118.5

Table 3.3: K_p and K_i for control pairings

λ_f is chosen such that the closed-loop PI step responses have as much low settling-time as possible. The closed-loop PI step responses can be seen in Figure 3.7. The responses show that the settling-times for all the three loops are slightly below 3 seconds, however, varying λ_f lower settling-times can be obtained, but under such tuning conditions, the manipulated variables ($0 \leqslant X_{\text{pp}} \leqslant 1$ and $0 \leqslant \mu \leqslant 1$) go beyond their bounds while trying to track the desired setpoints.

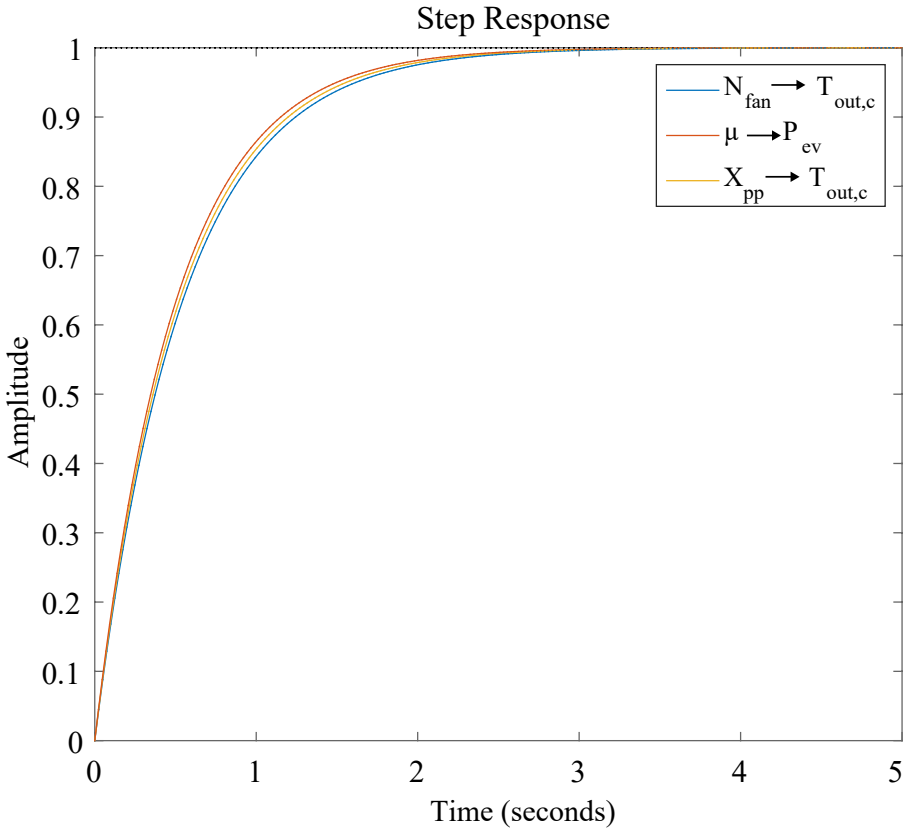

Figure 3.7: Closed-loop control response for each pairing

3.4 Cerebellar Model Articulation Controller (CMAC)

Nonlinear adaptive control schemes are effective in controlling nonlinear systems. Since a nonlinear approximator compensates for nonlinearities, these schemes do not require prior knowledge of the exact model. There are several types of Artificial Neural Networks (ANNs) that can serve as a nonlinear approximator. Radial Basis Function Networks (RBFN), can be used to approximate the nonlinearity using a weighted sum of basis functions (usually Gaussians). The RBFN works when there are few inputs, but suffers from the "*curse of dimensionality*" where the number of computations needed grows exponentially with the number of inputs. The Multilayer Perceptron (MLP) uses layers of sigmoidal basis functions, each of which takes a weighted sum of signals as an input and outputs a single value. MLP can handle a large number of inputs but takes a much longer time to train than RBFN. CMAC can train as fast as RBFN but does not suffer from the curse of dimensionality. (in practice CMAC is preferred over RBFN if number of inputs is greater than 3 or 4[72]). Thus, CMAC is chosen for the purpose of this work.

3.4.1 CMAC structure and methodology

The CMAC structure is comprised of m offset layers of lookup tables, each equally divided into Q quantizations with n number of inputs as seen in Figure 3.8.

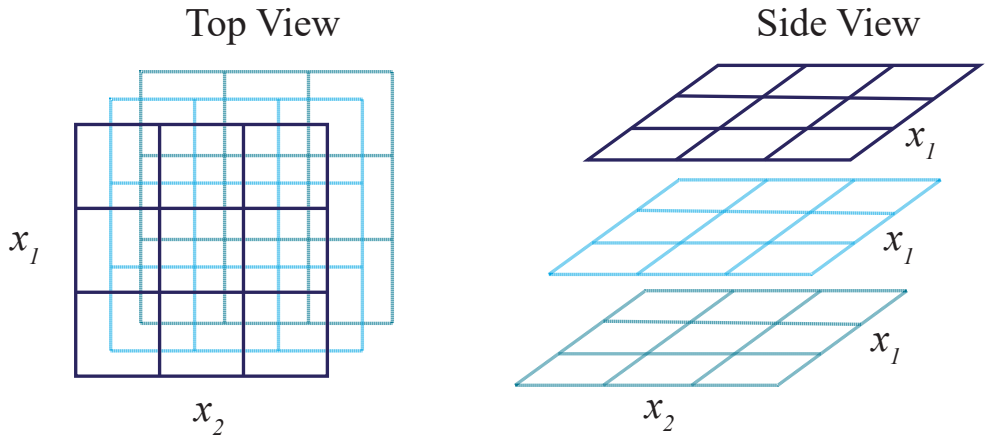

Figure 3.8: CMAC structure ($Q = 3$, $m = 3$, $n = 2$)

An input vector $x \in R^n$ is received by the CMAC which proceeds towards the offset layers. The total number of hypercube cells within the network is thus $N = mQ^n$. Each of these cells facilitates a space for a basis function - commonly these basis functions include binary (rectangular), triangular, and spline [72]:

$$Binary : \Gamma_i(x) = \begin{cases} 1 & \text{if } x \text{ is in cell } i \\ 0 & \text{otherwise} \end{cases}, \tag{3.13}$$

$$Triangular : \Gamma_i(x) = \begin{cases} \wedge & \text{if } x \text{ is in cell } i \\ 0 & \text{otherwise} \end{cases}, \tag{3.14}$$

$$Spline : \Gamma_i(x) = \begin{cases} \frown & \text{if } x \text{ is in cell } i \\ 0 & \text{otherwise} \end{cases}. \tag{3.15}$$

On each layer, the inputs received by the CMAC activate a hypercube cell and the basis function generates a value (Γ_i). Each of the generated values (Γ_i) are associated with individual weights (w_i). The weights in the CMAC begin at zero and are updated according to the training scheme. The output of the CMAC is the sum of the products of the basis functions and their associated weights:

$$\hat{f}(x) = \sum_{i=1}^{N} \Gamma_i(x) w_i. \tag{3.16}$$

The output can also be written in the following vector format

$$\hat{f}(x) = \Gamma(x) w, \tag{3.17}$$

where $\Gamma(x) \in R^{1\times m}$ is a row vector of associated basis functions and $\mathbf{w} \in R^{m\times 1}$ is a column vector of activated cell weights. The methodology of CMAC is explained with Figure 3.9, where two input variables $(x_1$ and $x_2)$ are quantized into three discrete regions on three different layers, *i.e.*

$Q = 3$ and $m = 3$. For this example, total number of hypercubes is $N = 27$ and the hypercubes are Aa, Ab, Ac, Ba, Bb, Bc, Ca, Cb, Cc, Da, Db, ... , Hi, Ig, Ih and Ii.. These hypercubes are numbered as Aa = 1, Ab = 2, ... , Ii = 27. Both the inputs range between 1 and 6. The inputs $x_1 = 4$ and $x_2 = 3$ are mapped in the memory locations of 5, 14 and 23, and they activate the weights associated with the hypercubes Bb in the first layer, Ee in the second layer and Hh in the third layer as shown in Figure 3.10.

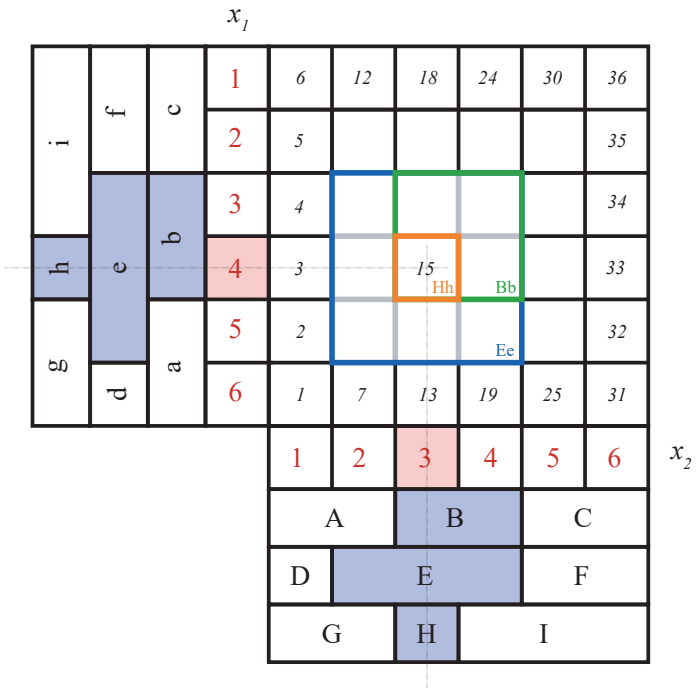

Figure 3.9: CMAC methodology with two input variables

Within the hypercubes Bb, Ee and Hh, the chosen basis function generates a single value as shown in Figure 3.11. A spline basis function is used for this work as shown in equation 3.18.

$$\Gamma_i(x) = \prod_{i=1}^{n} h_i^2 - 2h_i^3 + h_i^4, \tag{3.18}$$

where $0 < h_i < 1$ is the normalized position in the cell on input i.

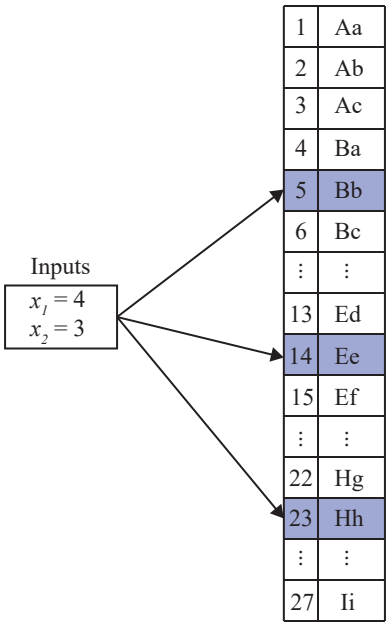

Figure 3.10: Mapping for CMAC with two-inputs

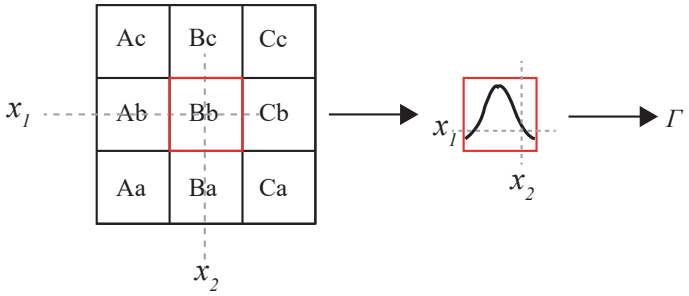

Figure 3.11: Basis function operating in hypercube for the first layer

For bigger values of n, N becomes too large to calculate in real time as well as to store in memory. The former problem is solved by keeping track of only m activated cells, i.e.,

$$\hat{f} = \sum_{i=1}^{m} \Gamma_{i,a}(x) w_{i,a} \tag{3.19}$$

where $\Gamma_{i,a}$ and $w_{i,a}$ are activated on layer i.

To tackle the storage problem, it should be noted that the large majority of the cells in the CMAC are never activated as trajectories move through a high-dimensional space, and hence the solution is to use random hash coding [7]. The hash coding can result in weights associated with

different cells mapped to the same physical memory location, which is referred to as a hash collision. By choosing the physical memory large enough, the errors due to the hash collisions become negligible with respect to the overall CMAC error.

The weights can be updated using offline training or online training. When trained online using the state error, the CMAC becomes an adaptive control, which is the case in this thesis.

It is essential that the weight update scheme be robust to disturbances. Standard robust techniques include projection [41], dead-zone [75][42], leakage [18] and *e*-modification [61][57][60]. All four can be shown to result in uniformly ultimately bounded signals using a standard Lyapunov analysis.

Projection, as shown in equation (3.20), requires knowledge of the maximum weight $(w_{\max})$ and the minimum weight $(w_{\min})$ of a system prior to implementation, thus prior training on the model is required.

$$\dot{\hat{w}} = \begin{cases} \mathbf{0} & \text{if } \Gamma^T z > 0 \text{and } \hat{w}_i > w_{i,\max} \\ \mathbf{0} & \text{if } \Gamma^T z < 0 \text{and } \hat{w}_i < w_{i,\max} \\ \beta \Gamma^T z & \text{otherwise} \end{cases}, \tag{3.20}$$

where constant $\beta > 0$ is the learning-rate of the CMAC.

Dead-zone, as shown in equation (3.21), requires knowledge of the bounds of the disturbance (d) and the control gain (G). But an exact idea of the bounds of the disturbance may not be available under all circumstances.

$$\dot{\hat{w}} = \begin{cases} \beta \Gamma^T z & \text{if } ||z|| > \frac{d_{\max}}{G_{\min}} \\ \mathbf{0} & \text{otherwise} \end{cases}. \tag{3.21}$$

Leakage uses

$$\dot{\hat{w}} = \beta(\Gamma^T z - \nu \hat{w}), \tag{3.22}$$

where ν is a positive constant. The *e*-modification method is similar to that of leakage, but results

in slightly better performance

$$\dot{\hat{w}} = \beta(\Gamma^T z - \nu||z||\hat{w}). \tag{3.23}$$

In [68], Dr. Macnab's proposed voting scheme for weight updates outperforms the *e*-modification weight update technique in a system that is prone to weight drift. However, the voting scheme is computationally complex and is required only when weight drift can be observed in the system. Adaptive CMAC control of TORC does not exhibit weight drift when *e*-modification is used.

3.4.2 CMAC adaptive control

In order to track a set-point, it is assumed that the nominal set-point (y_n) and the nominal control value (u_n) are known. The nominal operating condition is illustrated in Table 3.4. Using a decentralized model of the system for the control design, justified by the RGA analysis, gives

$$\dot{y}_i = f_i(x) - g_i u_i + D_i(T_{\text{sf},n}) + d_i(t), \text{ for } i = 1, 2, 3 \tag{3.24}$$

where each $f_i(x)$ represents the nonlinear terms, D_i represents a constant disturbance term due to a nominal value of the heat source, $d_i(t)$ represents bounded time-varying disturbances, and g_i is a positive constant. In reality, $g_i = g_i(x)$ but the variations are so small that it can be assumed a constant for control design purposes. The control required to drive the ORC system towards its desired working condition is

$$u_i = u_{i,n} + \Delta u_i, \tag{3.25}$$

where $\triangle u_i$ is the adaptive control given by

$$\triangle u_i = \Gamma_i(q)\hat{w}_i + K_i z_i. \tag{3.26}$$

where the inputs provided to the CMAC are

$$q = [P_{\text{ev}} \quad T_{\text{out,ev}} \quad T_{\text{out,c}} \quad P_c]^T \tag{3.27}$$

The output error is

$$z_i = y_i - y_{i,\text{sp}} \tag{3.28}$$

	Nominal value
Bulk temperature of heat source, T_{sf}	202°C
Evaporating pressure, $y_1 = P_{\text{ev}}$	4.986MPa
Temperature of R134a at outlet of evaporator, $y_2 = T_{\text{out,ev}}$	242°C
Temperature of R134a at outlet of condenser, $y_3 = T_{\text{out},c}$	36°C
Opening of valve, $u_1 = \mu$	0.45
Capacity fraction of pump, $u_2 = X_{\text{pp}}$	0.42
Condenser fan speed, $u_3 = N_{\text{fan}}$	300rpm

Table 3.4: Nominal operation condition

3.4.3 Stability Proof

To analyze a nonlinear control system, such as the adaptive CMAC used in this work, Lyapunov's direct method can used to determine stability [65]. Consider a direct adaptive control Lyapunov function

$$V_i = \frac{1}{2g_i} z_i^2 + \frac{1}{2\beta_i} \tilde{w}^T \tilde{w}, \tag{3.29}$$

where $\tilde{w}_i = w_i - \hat{w}_i$ is the weight estimation error in which w_i are the unknown ideal weights in the CMAC. For the rest of the stability analysis, the subscript $'i'$ is dropped without loss of generality.

For a non-linear system shown by equation (3.24), the error derivative is

$$\dot{z} = \dot{y} - \dot{y}_{\text{sp}}. \tag{3.30}$$

Assuming $\dot{y}_{\text{sp}} = 0$, substituting equation (3.24) into equation (3.30) gives

$$\dot{z} = f(x) - gu + D + d(t), \tag{3.31}$$

Now, time derivative of equation (3.29) gives the following

$$\dot{V} = \frac{1}{g} z^T \left[f(x) - g\left(u_n + \Delta u\right) + D + d(t) \right] - \frac{1}{\beta} \tilde{w}^T \dot{\hat{w}}. \tag{3.32}$$

Substituting equation (3.26) into equation (3.32) gives the following

$$\begin{aligned} \dot{V} =& \frac{1}{g} z^T \left[f(x) - g\left(u_n + \Delta u\right) + D + d(t) \right] - \frac{1}{\beta} \tilde{w}^T \dot{\hat{w}} \\ =& z \left(\frac{f(x) + D}{g} - u_n - \Gamma \hat{w} - Kz + d(t) \right) - \frac{1}{\beta} \tilde{w}^T \dot{\hat{w}}. \end{aligned} \tag{3.33}$$

The terms can be approximated by the CMAC neural network is

$$\frac{f(x) + D}{g} - u_n = \Gamma(q) w + \varepsilon(x), \tag{3.34}$$

with $\|\varepsilon(x)\| < \varepsilon_{\max} \forall x \in \mathscr{D}$ where $\varepsilon_{\max}$ is a positive constant bound on the approximation error and $\mathscr{D} \subset \Re^4$ is the region of approximation. Now, substituting equation (3.34) into equation (3.33) gives the following

$$\begin{aligned} \dot{V} =& z\left(\Gamma \tilde{w} + \varepsilon + d - Kz\right) - \frac{1}{\beta} \tilde{w}^T \dot{\hat{w}} \\ =& -Kz^2 + z(\varepsilon + d) + \tilde{w}^T \left(\Gamma^T z - \frac{\dot{\hat{w}}}{\beta} \right) \end{aligned} \tag{3.35}$$

Using the *e*-modification update law from equation (3.23) gives the following

$$\dot{V} = -Kz^2 + z(\varepsilon + d) + \nu |z| \tilde{w}^T w - \nu \tilde{w}^T \tilde{w} \tag{3.36}$$

$$\dot{V} < |z| \left(-K|z| + z d_{\max} + \nu \|\tilde{w}\| \|w\| - \nu \left\| \tilde{w}^2 \right\| \right), \tag{3.37}$$

where $d_{\max}$ is a positive constant that bounds $|\varepsilon + d|$. By completing the square in equation (3.37), it can be shown that $\dot{V} < 0$ when either $|z| > \delta_z$ or $\|\tilde{w}\| > \delta_w$ where

$$\delta_z = \frac{d_{\max}}{K} + \frac{\nu \|w\|^2}{4K} \tag{3.38}$$

$$\delta_w = \frac{\|w\|}{2} + \sqrt{\frac{d_{\max}}{\nu} + \frac{\|w\|^2}{4}}. \tag{3.39}$$

Thus, the signals are uniformly ultimately bounded with an ultimate bound given by the Lyapunov surface $V(z, \|w\|) = V(\delta_z, \delta_w)$.

It should be noted from equation (3.2) that despite the pairings chosen in Section 3.2, there are still interconnections between μ and $T_{\text{out,ev}}$, and X_{pp} and P_{ev}. If the interconnections are of higher order, i.e. anything above first order, an adaptive controller might not achieve stability [91]; the assumption that positive constant $d_{\max}$ exists may be violated. From Table 3.1, one can observe a second-order interconnection between μ and $T_{\text{out,ev}}$ while a first-order interconnection between X_{pp} and P_{ev} can be seen. Decentralized adaptive control can be made robust to interconnections [91], but the robust terms required may lead to unwanted control signal chatter. Therefore the adaptive control in equation (3.25) with the weight update law defined in equation (3.23) are used in this thesis for designing the decentralized adaptive CMAC.

3.5 Summary

The system was shown to be diagonally dominant using RGA analysis, and thus a decentralized control can be used with three separate control loops. A nonlinear adaptive control using CMAC has been designed for the ORC system. In addition to that, a PI controller is also designed using the IMC technique in order to compare with the performance of the CMAC.

Chapter 4

Results

To investigate the performance of the adaptive CMAC, a few tests were conducted based on the TORC process model. The state space system is solved in the MATLAB environment using the built-in solver ODE23t with a sampling period of 0.1s. The results are compared to a PI controller for the same tests with no change in control gains. The tests are described below.

4.1 Disturbance rejection

The heat source, for this thesis, industrial waste heat, in practice will not have a constant temperature (T_{sf}). Small changes (fluctuations) to the system should be followed by the controller to maximize net output power while keeping the process variables at their desired safety level. Such a variation in T_{sf} is shown in Figure 4.1, which is introduced to the TORC as disturbance.

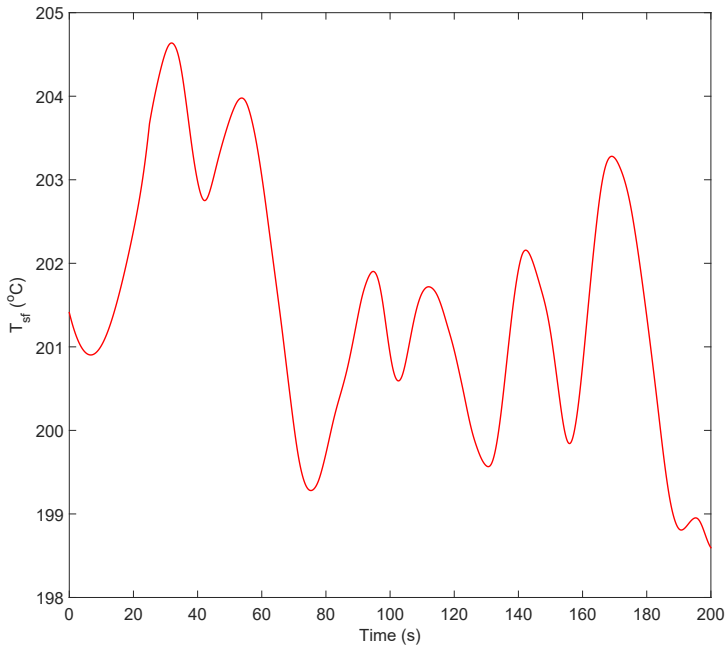

Figure 4.1: Variation in heat source temperature

The simulation result for the introduced disturbance to the system is shown in Figure 4.2 showing the performance of the adaptive CMAC and the PI controller. The changes in CVs are within an acceptable region for both the controllers. However, the CMAC has outperformed the PI controller in terms of tracking performance with much lower deviation from the set-points while converging faster as well. The variations in the MVs, as shown in Figure 4.3 are also within the allowable ranges regardless of the variation in T_{sf}. The adaptive CMAC was also able to achieve higher net power output with respect to variations in T_{sf} when compared to the PI as shown in Figure 4.4.

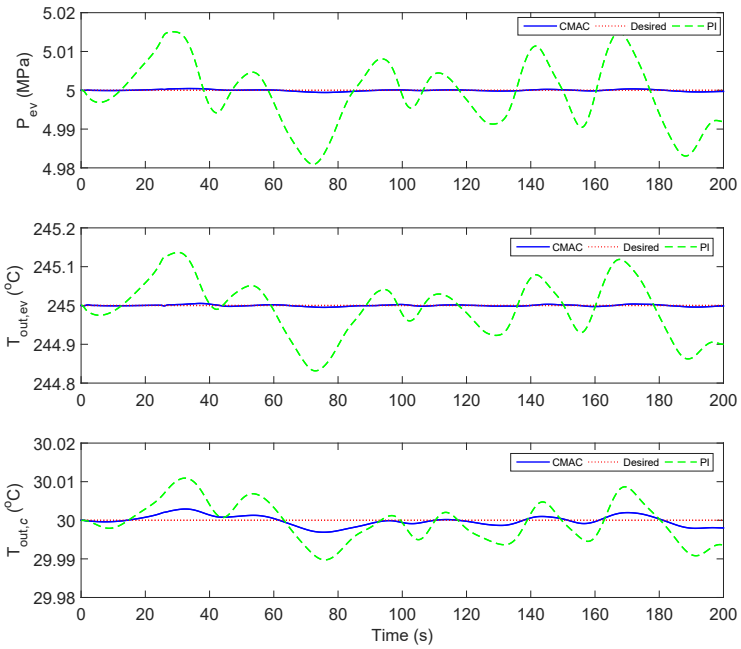

Figure 4.2: Set-point tracking under the influence of disturbance

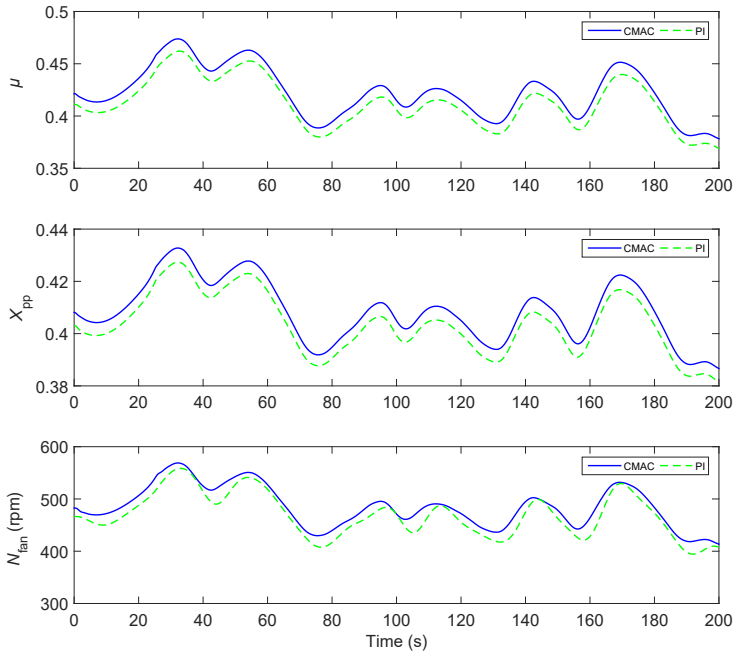

Figure 4.3: Variation in MVs under the influence of disturbance

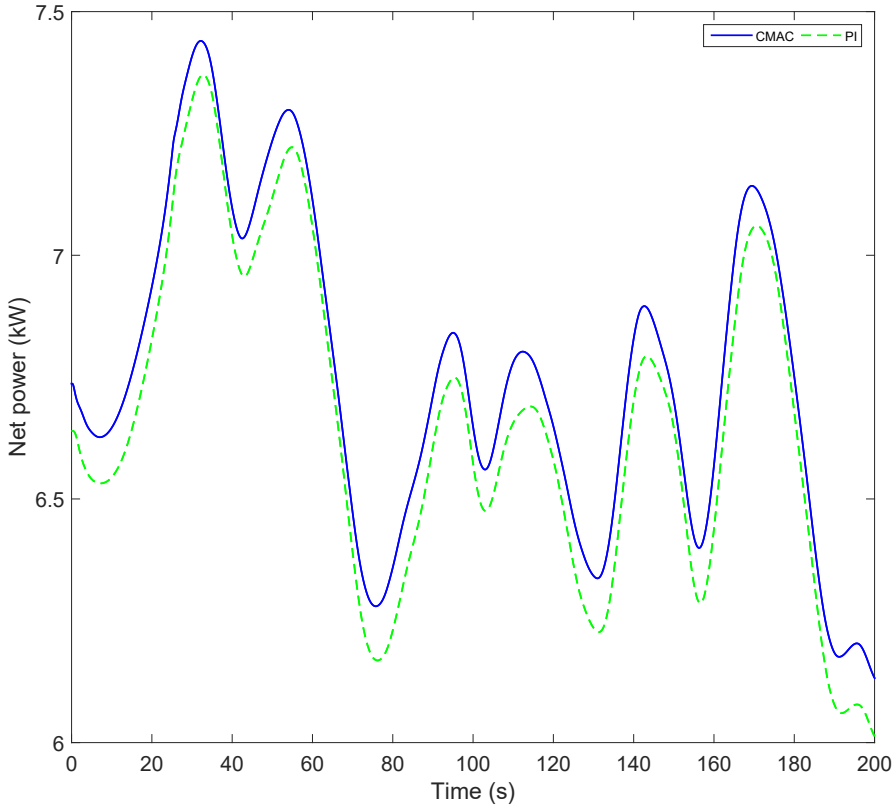

Figure 4.4: Net power output for disturbance rejection test

The previous results show the CMAC performance after 151 training trials, which is how long it takes the CMAC to converge for the disturbance rejection test (Figure 4.11). The weights also converge after this much training (Figure 4.6). The RMS error is calculated for all the three output channels together.

$$\text{RMS error } = \sqrt{\frac{1}{n}\sum_{k=1}^{n}(\hat{y}_k - y_k)}, \tag{4.1}$$

where y_k is the set-point for k^{th} observation and $\hat{y}_k$ is the actual output.

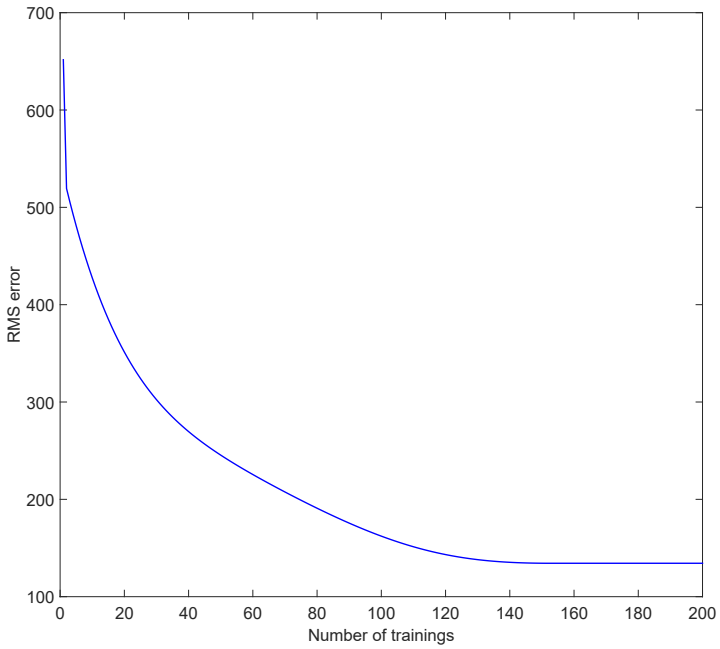

Figure 4.5: RMS error convergence for disturbance rejection test

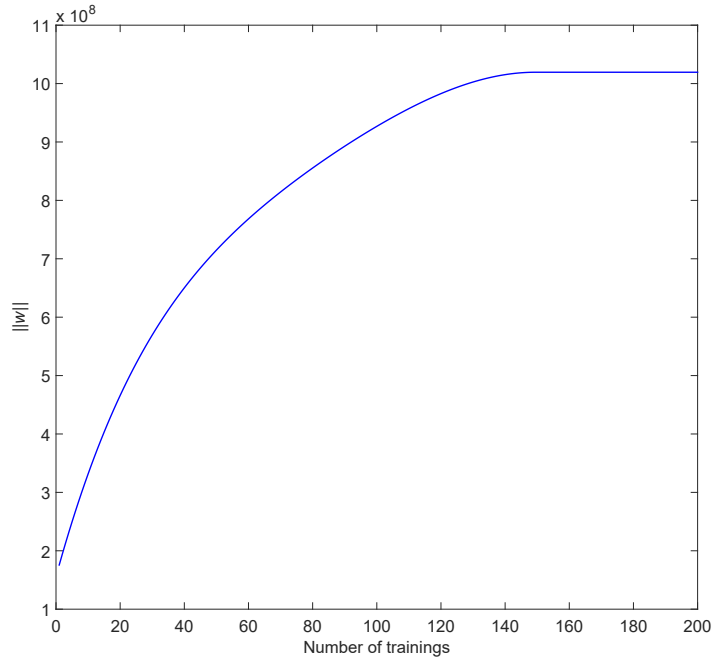

Figure 4.6: Behavior of weights in CMAC for disturbance rejection

4.2 Set-point tracking

In this section, in order to test the controller's tracking ability, set-points of evaporating pressure, outlet temperatures of working fluid at the evaporator and the condenser are changed (keeping $T_{\text{sf}} = 202^{\text{o}}\text{C}$ as constant). At $50s$, a ramp change of the set-point of the evaporating pressure is imposed from 5Mpa to 5.02MPa at a rate of 0.004MPa/s, and then the set-point is imposed back to 5MPa at $95s$ with the same rate. A ramp change of the set-point of the outlet temperature at the evaporator is imposed at $140s$ from 245^{o}C to 250^{o}C at a rate of $1^{\text{o}}\text{C}/s$, and then the set-point is imposed back to 245^{o}C at $185s$ with the same rate. Finally, a ramp change of the set-point of the outlet temperature at the condenser is imposed at $230s$ from 30^{o}C to 30.15^{o}C at a rate of $0.03^{\text{o}}\text{C}/s$, and then the set-point is imposed back to 30^{o}C at $275s$ with the same rate. The simulation results shown in Figure 4.7 demonstrate that the adaptive CMAC performs well in tracking for the channels $T_{\text{out,ev}}$ (see Figure 4.8 as well) and P_{ev}, however, for the $T_{\text{out,c}}$ channel, when the set-point is changed, the PI controller demonstrates better performance in tracking. The control effort by both the controllers are within an acceptable range (Figure 4.9). In Figure 4.10, it can be seen that the adaptive CMAC is capable of generating more net power compared to the PI controller despite changes in set-points.

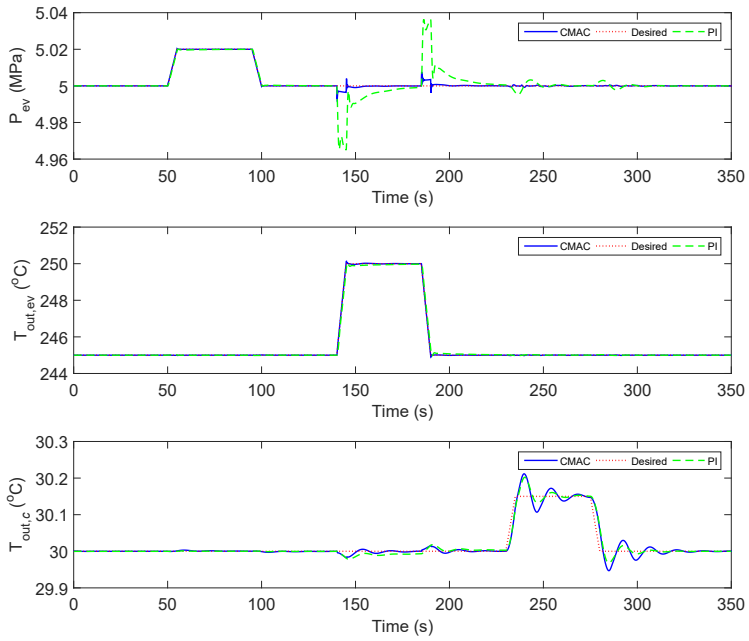

Figure 4.7: Change in set-points of the CVs

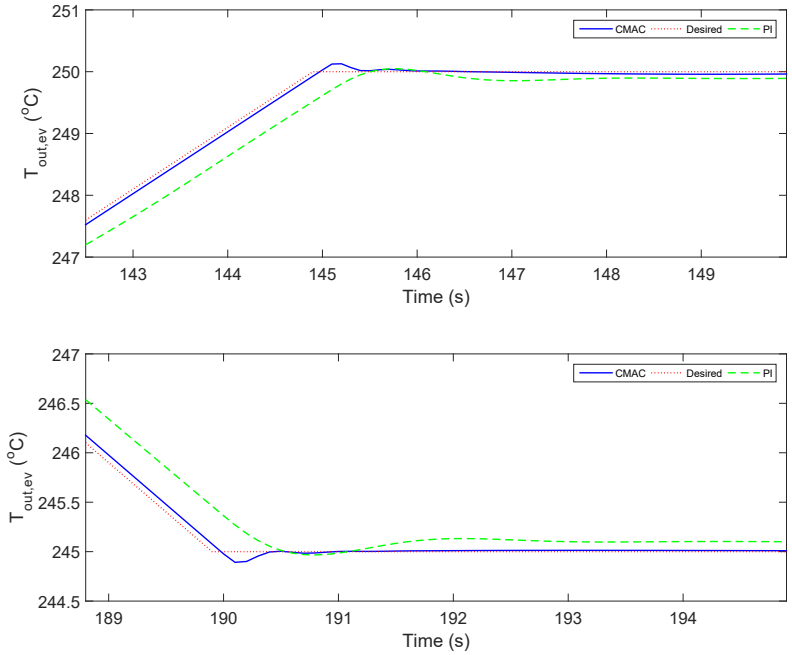

Figure 4.8: $T_{\text{out,ev}}$ channel zoomed

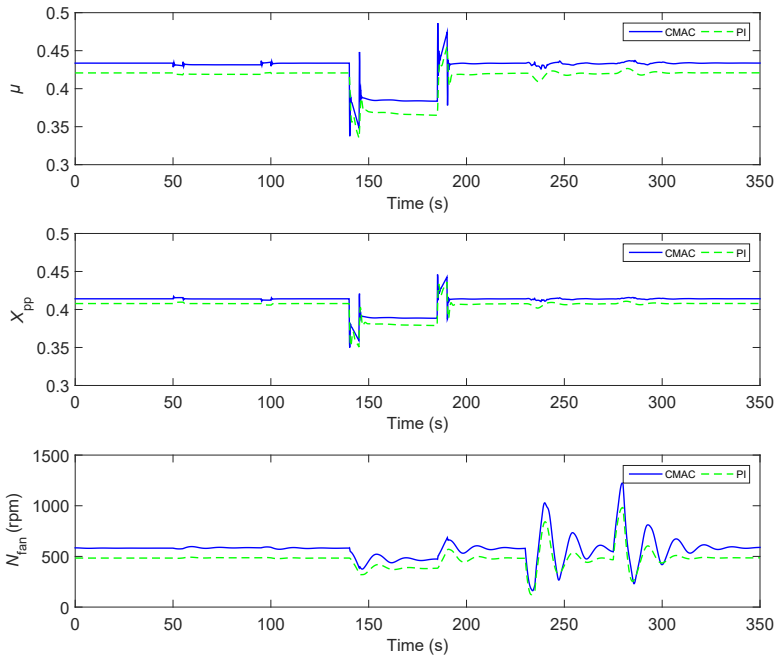

Figure 4.9: Variation in MVs for set-point tracking

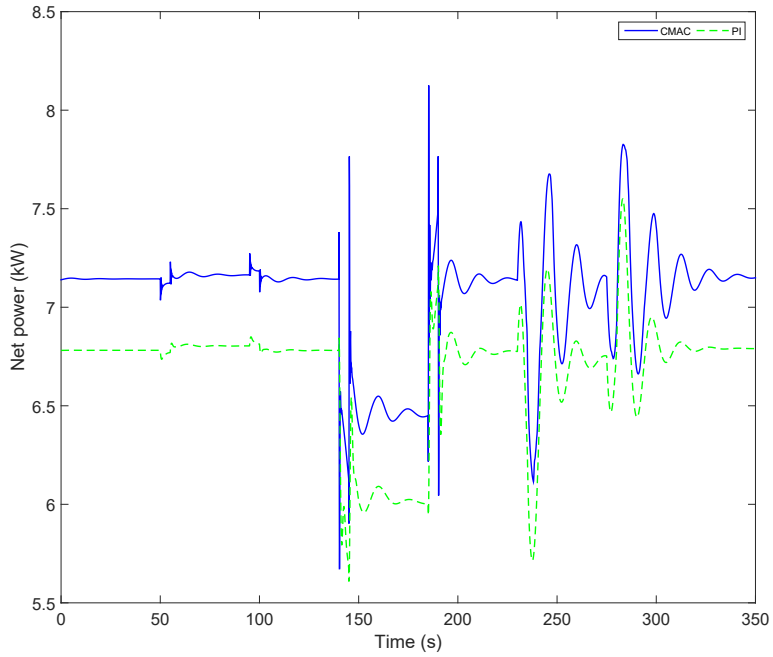

Figure 4.10: Net power for set-point tracking

The previous results show the CMAC performance after 26 training trials, which is how long it takes the CMAC to converge for the set-point tracking test (Figure 4.11). The weights also converge after this much training (Figure 4.12).

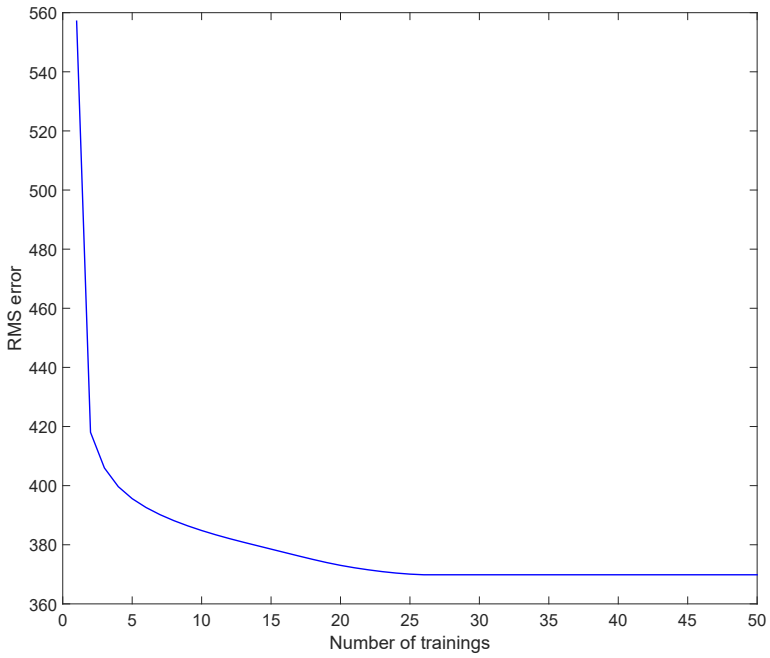

Figure 4.11: RMS error convergence for set-point tracking test

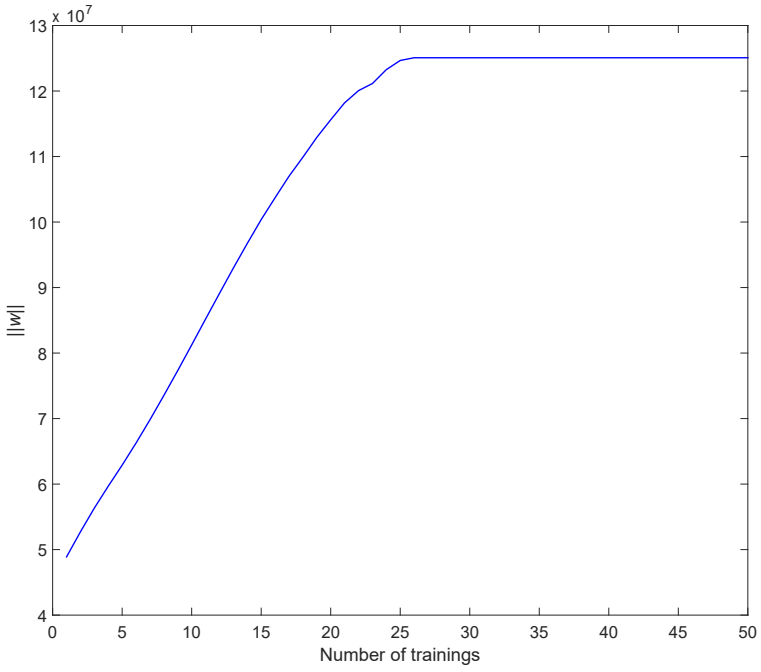

Figure 4.12: Behavior of weights in CMAC for the set-point tracking

4.3 Step-disturbance rejection

The heat source temperature(T_{sf}) may move away from its nominal value, but this shift in value may not last long and this shift can be simulated in the form of a step-disturbance. In such a scenario, the controller has to be effective in canceling the step change in T_{sf} by treating it as a disturbance, otherwise, this change will lead to a higher magnitude deviation from the set-point (bringing about safety concerns mainly due to a significant increase in pressure). Also, a significant decrease in pressure may result in a change in the region of the working fluid inside the evaporator, i.e. supercritical to subcritical. To test the effectiveness of the adaptive CMAC, a step disturbance is introduced, as shown in Figure 4.13, to the system and its performance is compared to a PI controller.

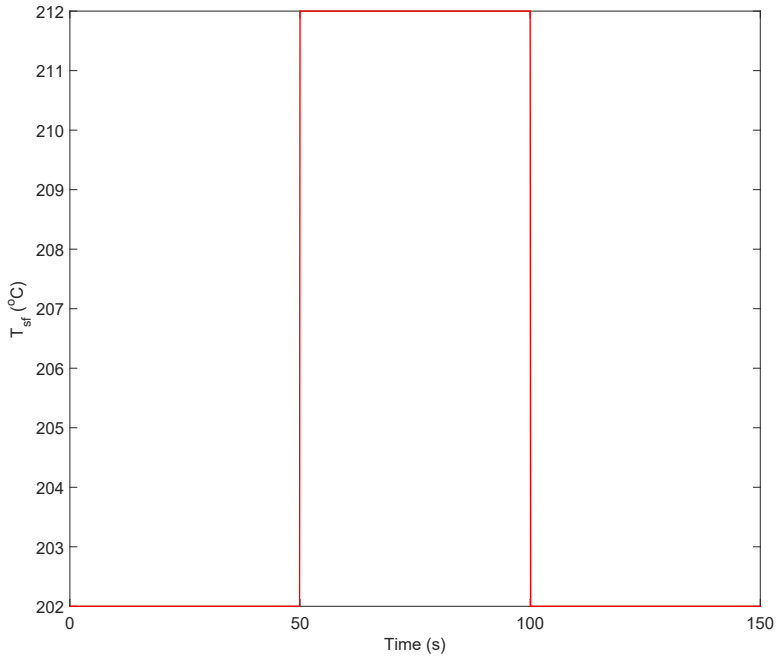

Figure 4.13: Step changes in T_{sf}

Figure 4.14 shows the performance of the two controllers trying to track the set-point under a step disturbance. The proposed CMAC controller has proven to be more effective than the PI controller in rejecting the step disturbance from the heat source temperature by converging to the set-point significantly faster while having lower-amplitude overshoots. To achieve this perfor-

mance, both the controllers generated control signals within acceptable limits and sharpness as shown in Figure 4.15. Net power, as can be seen from Figure 4.16, during the settling period is higher for the proposed CMAC compared to the PI controller.

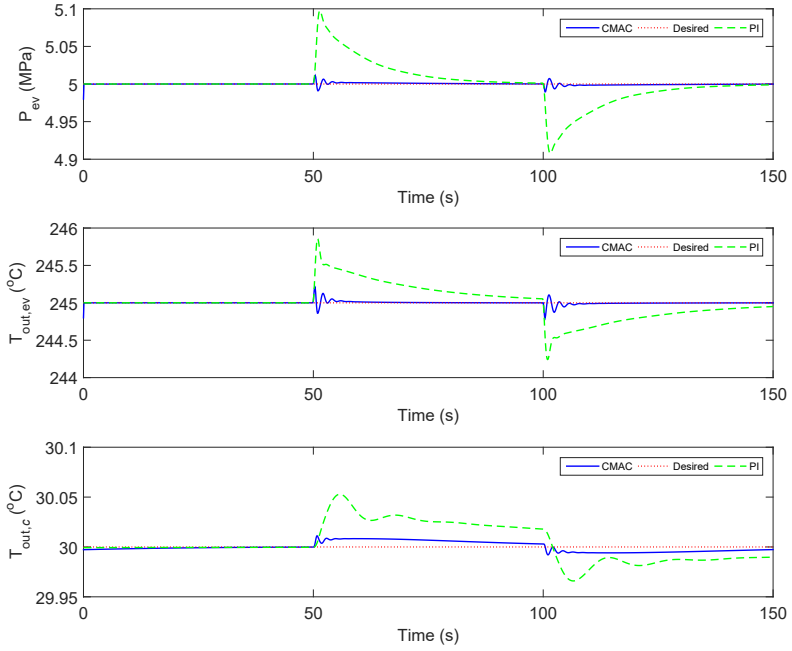

Figure 4.14: Set-point tracking under the influence of step disturbance

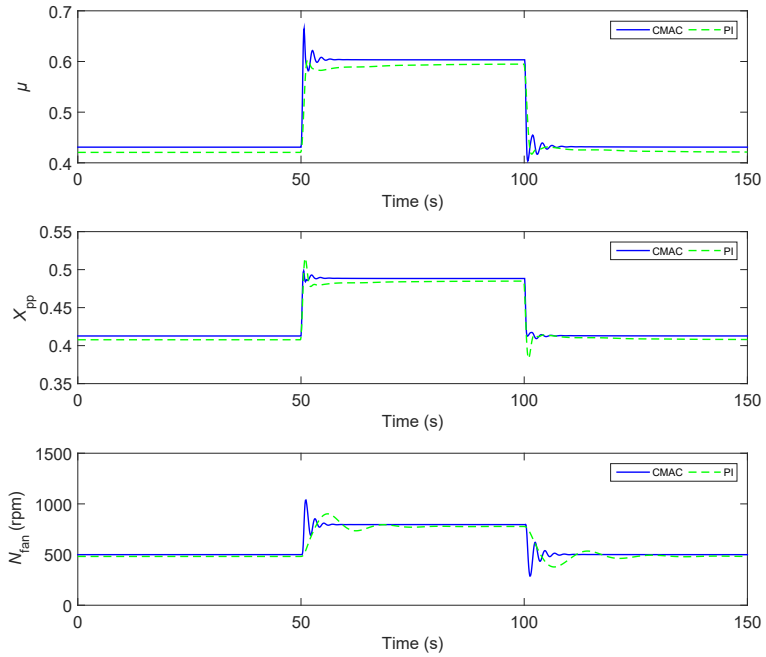

Figure 4.15: Variation in MVs under the influence of step disturbance

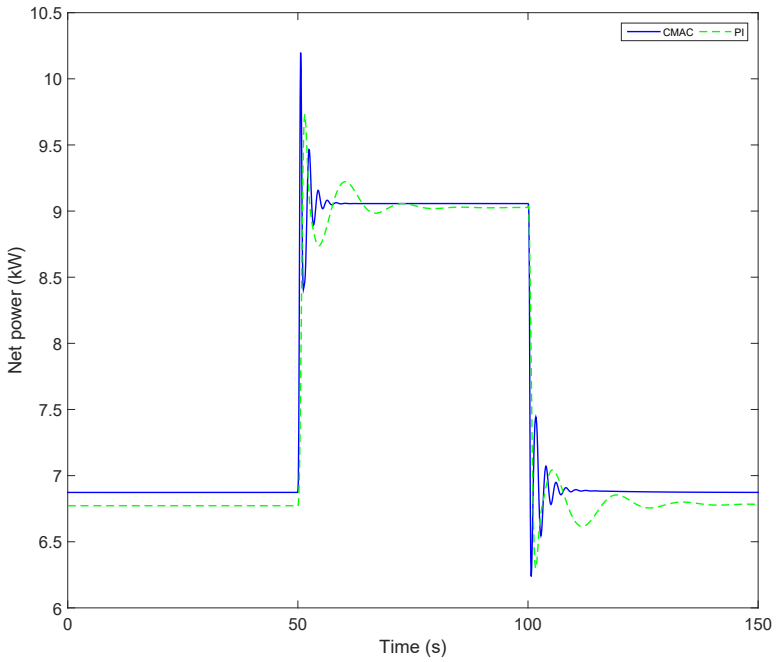

Figure 4.16: Net power for step-disturbance rejection

The previous results show the CMAC performance after 28 training trials, which is how long it takes the CMAC to converge for the step-disturbance rejection test (Figure 4.11). The weights also converge after this much training (Figure 4.12).

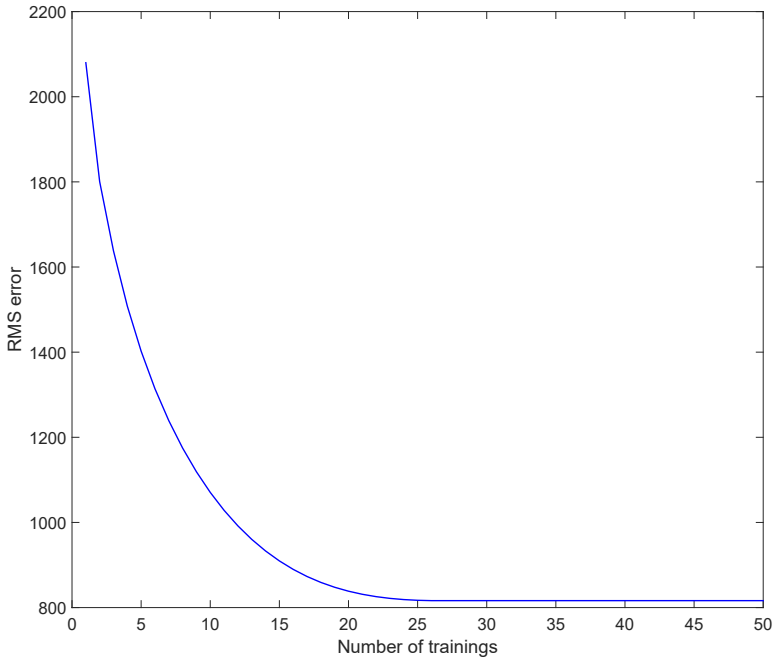

Figure 4.17: RMS error convergence for step-disturbance rejection test

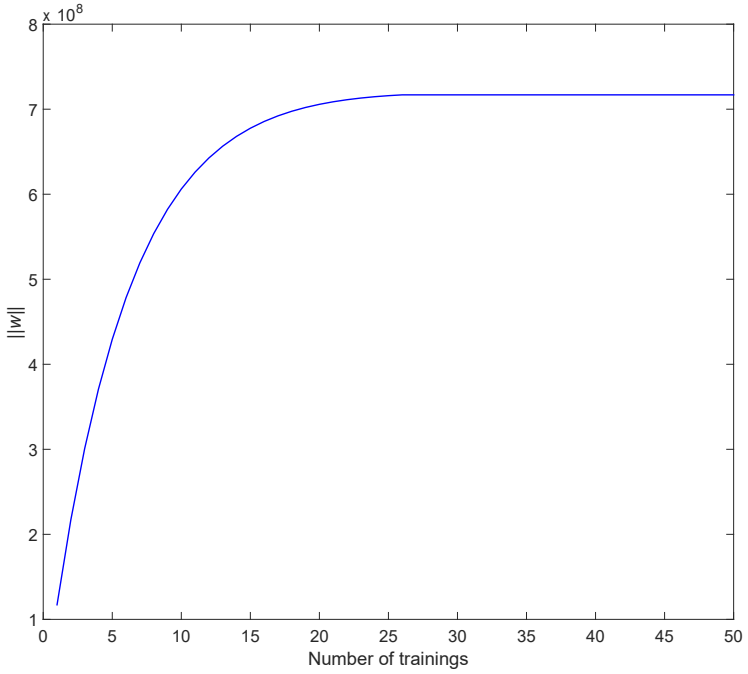

Figure 4.18: Behavior of weights in CMAC for the step-disturbance rejection

4.4 Summary

Except for set-point tracking test in $T_{\text{out},c}$ channel, the adaptive CMAC has outperformed the PI controller in all three tests showing its set-point tracking ability despite heat source temperature variations and set-point changes, summarized in Table 4.1, Table 4.2 and Table 4.3. It can be seen that the RMS errors for the PI controller, combining all the three channels, is quite high compared to the CMAC for all the three performed tests. The adaptive CMAC was also able to accumulate more net energy $\left(E_{net} = \int_0^{\text{totaltime}} \dot{W}_{\text{net}} dt\right)$ as output over the period of time for all the three tests (Table 4.4) which was the main objective of the controllers. In order to achieve the desired goals, the adaptive CMAC exhibited reasonable and feasible variations in MVs while making sure the CVs are well within proper changes.

	Disturbance rejection	Set-point tracking	Step disturbance
CMAC	230.61	640.5	1504.7
PI	8559	5939	17483

Table 4.1: RMS error for P_{ev} (Pa)

	Disturbance rejection	Set-point tracking	Step disturbance
CMAC	0.0021	0.0088	0.0226
PI	0.0735	0.0653	0.1594

Table 4.2: RMS error for $T_{\text{out,ev}}$($^{\text{o}}$C)

	Disturbance rejection	Set-point tracking	Step disturbance
CMAC	0.0014	0.0131	0.0047
PI	0.0052	0.0113	0.0164

Table 4.3: RMS error for $T_{\text{out},c}$ ($^{\text{o}}$C)

	Disturbance rejection	Set-point tracking	Step disturbance
CMAC	1.3502	2.4662	1.1407
PI	1.3312	2.3366	1.1295

Table 4.4: Net energy (MJ) comparison between adaptive CMAC and PI controller

Chapter 5

Conclusion

The goal of this thesis was two-fold - to first model a TORC and then design an adaptive control using a CMAC neural network (and compare its performance with traditional PI controller).

5.1 Conclusion

In this thesis, a control-oriented model for TORC is constructed and its primary control tasks are briefly outlined. The TORC model consists of a subcritical heat exchanger, i.e. the condenser, as well as a supercritical heat exchanger, i.e. the evaporator, with the addition of a recuperator (working in both subcritical region and supercritical region). To the best of this author's knowledge, no previous work has modelled a recuperated TORC (although the techniques used for the modelling are known). A validation of the modelled TORC was not carried out in this thesis. An adaptive CMAC is proposed to ensure efficient heat recovery and to maximize net power while keeping the process variables at their desired levels. Although the idea of an adaptive CMAC is not novel, the application is novel. The results of the CMAC were compared with a PI controller - the tuned PI parameters were obtained using the IMC technique based on first-order models which were identified (using MATLAB System Identification Toolbox) from the pairings of CVs and MVs suggested by the RGA analysis. Three different tests were performed on the controllers to evaluate the performance. In all three of the tests, the proposed CMAC controller outperformed the PI controller, despite variations in the heat source temperature and set-point. The deviations from

the set-point for the PI controller were especially large in the evaporating pressure (P_{ev}) channel compared to the adaptive CMAC, which is a safety concern. In all three tests the adaptive CMAC was able to generate more net power compared to the traditional PI controller while maintaining process variables within the safety margin.

5.2 Future work

From the modeling perspective, a validation of the model is absolutely necessary against an actual TORC in operation with actual parameters implemented in the model. Once the validation of the model is completed, from the control perspective, the next step will be to implement the adaptive CMAC and observe the feasibility of implementing a neural network in a TORC by comparing with the traditional PI controller in experiment as well. While weight drift was not observed in simulations in this thesis, this may not be the case in real-time operation due to several unknown external factors affecting the plant. In such a scenario, the adaptive CMAC algorithm will need to undergo further modification(s) in order to prevent weight drift.

In the modeling process, while the focus has been mainly on the dynamic modelling of the heat exchangers and static models of the other components, the effect of pipes in the system should be considered in the future since the pipes cause pressure changes in the working fluid due to friction and difference in heights, and also may affect the temperature in the working fluid due to radiation and heat transfer. The dynamics of the heat source were ignored, which can be an addition to the model in the future provided that prior knowledge of the heat source is available.

In terms of control strategy, the flow of the waste heat is a possible MV which has not been explored in this thesis, but it will be interesting to tap into this area to see if it can actually enhance the performance of the TORC. However, the cost of introducing an extra actuator should also be considered during the investigation.

For this thesis, only the heat source temperature was considered to be the disturbance, however, disturbances may occur in other forms as well - such as the mass flow rate of the heat source

or changes in the ambient temperature. The proposed controller should be able to reject such disturbances and should be put into future test to test the efficiency of the proposed controller.

Bibliography

[1] Canadian national geothermal database and provincial resource estimate maps - alberta geothermal favourability maps. Technical report, Canadian Geothermal Energy Association.

[2] *DOE FUNDAMENTALS HANDBOOK - THERMODYNAMICS, HEAT TRANSFER, AND FLUID FLOW*.

[3] World fossil fuel reserves and projected depletion. Technical report, The Colorado River Commission of Nevada, March 2002.

[4] Muhamad Iradat Achmad, Hanung Adinugroho, and Adhi Susanto. Cerebellar model articulation controller (cmac) for sequential images coding. pages 160–166, 2014.

[5] International Energy Agency. *Key world energy statistics*. International Energy Agency, 2015.

[6] James S Albus. Data storage in the cerebellar model articulation controller (cmac). *Journal of Dynamic Systems, Measurement, and Control*, 97(3):228–233, 1975.

[7] James S Albus. A new approach to manipulator control: The cerebellar model articulation controller (cmac). *Journal of Dynamic Systems, Measurement, and Control*, 97(3):220–227, 1975.

[8] James Sacra Albus. A model for memory in the brain. 1971.

[9] American Society of Heating, Refrigerating and Air-Conditioning Engineers, Inc. *ASHRAE STANDARD - Designation and Safety Classification of Refrigerants*, 2008.

[10] Santosh Ananthraman and Devendra P Garg. Training backpropagation and cmac neural networks for control of a scara robot. *Engineering Applications of Artificial Intelligence*, 6(2):105–115, 1993.

[11] Mituhiko Araki. Pid control. *Control systems, robotics and automation*, 2:1–23, 2002.

[12] Junjiang Bao and Li Zhao. A review of working fluid and expander selections for organic rankine cycle. *Renewable and Sustainable Energy Reviews*, 24:325–342, 2013.

[13] Arash Beirami and CJB Macnab. Direct neural-adaptive control of robotic manipulators using a forward dynamics approach. pages 363–367, 2006.

[14] Ian H. Bell, Jorrit Wronski, Sylvain Quoilin, and Vincent Lemort. Pure and pseudo-pure fluid thermophysical property evaluation and the open-source thermophysical property library coolprop. *Industrial & Engineering Chemistry Research*, 53(6):2498–2508, 2014.

[15] Satyam Bendapudi, James E Braun, and Eckhard A Groll. Dynamic model of a centrifugal chiller system–model development, numerical study, and validation. *ASHRAE Transactions*, 111(1), 2005.

[16] Satyam Bendapudi, James E Braun, and Eckhard A Groll. A comparison of moving-boundary and finite-volume formulations for transients in centrifugal chillers. *International Journal of Refrigeration*, 31(8):1437–1452, 2008.

[17] B Wayne Bequette. *Process control: modeling, design, and simulation*. Prentice Hall Professional, 2003.

[18] S Blazic, D Matko, and I Skrjanc. Adaptive law with a new leakage term. *IET control theory & applications*, 4(9):1533–1542, 2010.

[19] Lars J Brasz and William M Bilbow. Ranking of working fluids for organic rankine cycle applications. 2004.

[20] Edgar Bristol. On a new measure of interaction for multivariable process control. *Automatic Control, IEEE Transactions on*, 11(1):133–134, 1966.

[21] Ihsan Omur Bucak and Bekir Karlik. Detection of drinking water quality using cmac based artificial neural networks. *Ekoloji*, 20(78):75–81, 2011.

[22] David Butterworth and Design Council. Introduction to heat transfer, 1977.

[23] Natural Resources Canada. About renewable energy.

[24] Natural Resources Canada. Solar thermal.

[25] Gabriela Cembrano, Gordon Wells, Jesus Sardá, and Armando Ruggeri. Dynamic control of a robot arm using cmac neural networks. *Control engineering practice*, 5(4):485–492, 1997.

[26] Dan Chen and Dale E Seborg. Relative gain array analysis for uncertain process models. *AIChE journal*, 48(2):302–310, 2002.

[27] Huijuan Chen, D Yogi Goswami, Muhammad M Rahman, and Elias K Stefanakos. A supercritical rankine cycle using zeotropic mixture working fluids for the conversion of low-grade heat into power. *Energy*, 36(1):549–555, 2011.

[28] Huijuan Chen, D Yogi Goswami, and Elias K Stefanakos. A review of thermodynamic cycles and working fluids for the conversion of low-grade heat. *Renewable and sustainable energy reviews*, 14(9):3059–3067, 2010.

[29] Yang Chen, P Lundqvist, Anders Johansson, and P Platell. A comparative study of the carbon dioxide transcritical power cycle compared with an organic rankine cycle with r123 as working fluid in waste heat recovery. *Applied Thermal Engineering*, 26(17):2142–2147, 2006.

[30] S Commuri and Frank L Lewis. Cmac neural networks for control of nonlinear dynamical systems: structure, stability and passivity. *Automatica*, 33(4):635–641, 1997.

[31] J.M. Coulson, J.F. Richardson, J R Backhurst, and J H Harker. *Chemical Engineering: Fluid Flow, Heat Transfer and Mass Transfer (6th Edition)*. Butterworth Heinemann, 1999.

[32] Yiping Dai, Jiangfeng Wang, and Lin Gao. Parametric optimization and comparative study of organic rankine cycle (orc) for low grade waste heat recovery. *Energy Conversion and Management*, 50(3):576–582, 2009.

[33] Murat Darka. The control of a manipulator using cerebellar model articulation controllers. Master's thesis, İzmir Institute of Technology, 2003.

[34] Agustín M Delgado-Torres and Lourdes García-Rodríguez. Analysis and optimization of the low-temperature solar organic rankine cycle (orc). *Energy Conversion and Management*, 51(12):2846–2856, 2010.

[35] Adriano Desideri, Jorrit Wronski, Bertrand Dechesne, Martijn van den Broek, Sergei Gusev, Sylvain Quoilin, and Vincent Lemort. Comparison of moving boundary and finite-volume heat exchangers models in the modelica language. 2015.

[36] Ulli Drescher and Dieter Brüggemann. Fluid selection for the organic rankine cycle (orc) in biomass power and heat plants. *Applied Thermal Engineering*, 27(1):223–228, 2007.

[37] DuPont. *Thermodynamic Properties of HFC-134a*, 2004.

[38] Incorporated Energetics. Energy loss reduction and recovery in industrial energy systems. Technical report, U.S. Department of Energy, November 2004.

[39] Environment and Climate Change Canada. *Draft Environmental Code of Practice for Elimination of Fluorocarbon Emissions from Refrigeration and Air Conditioning Systems (Appendix 3)*.

[40] AB Etemoglu. Thermodynamic evaluation of geothermal power generation systems in turkey. *Energy Sources, Part A*, 30(10):905–916, 2008.

[41] Jay A Farrell and Marios M Polycarpou. *Adaptive approximation based control: unifying neural, fuzzy and traditional adaptive approximation approaches*, volume 48. John Wiley & Sons, 2006.

[42] Mark French, Csaba Szepesvari, and Eric Rogers. Uncertainty, performance, and model dependency in approximate adaptive nonlinear control. *IEEE Transactions on Automatic Control*, 45(2):353–358, 2000.

[43] Hong Gao, Chao Liu, Chao He, Xiaoxiao Xu, Shuangying Wu, and Yourong Li. Performance analysis and working fluid selection of a supercritical organic rankine cycle for low grade waste heat recovery. *Energies*, 5(9):3233–3247, 2012.

[44] Filson H Glanz, W Thomas Miller, and L Gordon Kraft. An overview of the cmac neural network. pages 301–308, 1991.

[45] S Glover, R Douglas, L Glover, G McCullough, and S McKenna. Automotive waste heat recovery: Working fluid selection and related boundary conditions. *International Journal of Automotive Technology*, 16(3):399–409, 2015.

[46] Allen D.M. Bell S. Chen Z. Ferguson G. Jessop A. Kelman M. Ko M. Majorowicz J. Moore M. Raymond J. Grasby, S.E. and R Therrien. *Geothermal Energy Resource Potential of Canada*. Geological Survey of Canada, 2012.

[47] Liu Guangbin, Z Yuanyang, L Yunxia, and L Liansheng. Simulation of the dynamic processes in a scroll expander generator used for small-scale organic rankine cycle system. *Proceedings of the Institution of Mechanical Engineers, Part A: Journal of Power and Energy*, 225(1):141–149, 2011.

[48] Control Guru. Ziegler-nichols tuning poor choice for production processes. http://controlguru.com/ziegler-nichols-tuning-poor-choice-for-production-processes, 2015. Accessed: 2016-07-27.

[49] Chao He, Chao Liu, Hong Gao, Hui Xie, Yourong Li, Shuangying Wu, and Jinliang Xu. The optimal evaporation temperature and working fluids for subcritical organic rankine cycle. *Energy*, 38(1):136–143, 2012.

[50] Xiang-Dong He. *Dynamic Modeling and Multivariable Control of Vapor Compression Cycles in Air Conditioning Systems*. PhD thesis, Massachusetts Institute of Technology, 1996.

[51] Xiang-Dong He, Sheng Liu, Harry H Asada, and Hiroyuki Itoh. Multivariable control of vapor compression systems. *HVAC&R Research*, 4(3):205–230, 1998.

[52] Frank Incropera and David DeWitt. Introduction to heat transfer. 1985.

[53] Arne Jakobsen. *Energy optimisation of refrigeration systems: the domestic refrigerator-a case study*. Refrigeration Laboratory, The Technical University of Denmark, 1995.

[54] Jakob Munch Jensen. *Dynamic Modeling of Thermo-Fluid Systems*. PhD thesis, Technical University of Denmark, 2003.

[55] Sotirios Karellas and Andreas Schuster. Supercritical fluid parameters in organic rankine cycle applications. *International Journal of Thermodynamics*, 11(3):101–108, 2008.

[56] Sotirios Karellas, Andreas Schuster, and Aris-Dimitrios Leontaritis. Influence of supercritical orc parameters on plate heat exchanger design. *Applied Thermal Engineering*, 33:70–76, 2012.

[57] Nakwan Kim and Anthony J Calise. Several extensions in methods for adaptive output feedback control. *IEEE transactions on neural networks*, 18(2):482–494, 2007.

[58] Young H Kim and Frank L Lewis. Optimal design of cmac neural-network controller for robot manipulators. *Systems, Man, and Cybernetics, Part C: Applications and Reviews, IEEE Transactions on*, 30(1):22–31, 2000.

[59] L Gordon Kraft and David P Campagna. A comparison between cmac neural network control and two traditional adaptive control systems. *Control Systems Magazine, IEEE*, 10(3):36–43, 1990.

[60] Ognjen Kuljaca, Nitin Swamy, Frank L Lewis, and Chiman M Kwan. Design and implementation of industrial neural network controller using backstepping. *IEEE Transactions on Industrial Electronics*, 50(1):193–201, 2003.

[61] Chiman Kwan and Frank L Lewis. Robust backstepping control of nonlinear systems using neural networks. *IEEE Transactions on Systems, Man, and Cybernetics-Part A: Systems and Humans*, 30(6):753–766, 2000.

[62] GA Larsen, S Cetinkunt, and A Donmez. Cmac neural network control for high precision motion control in the presence of large friction. *Journal of dynamic systems, measurement, and control*, 117(3):415–420, 1995.

[63] Chun-Shin Lin and Ching-Tsan Chiang. Learning convergence of cmac technique. *Neural Networks, IEEE Transactions on*, 8(6):1281–1292, 1997.

[64] Bo-Tau Liu, Kuo-Hsiang Chien, and Chi-Chuan Wang. Effect of working fluids on organic rankine cycle for waste heat recovery. *Energy*, 29(8):1207–1217, 2004.

[65] Aleksandr Mikhailovich Lyapunov. The general problem of the stability of motion. *International Journal of Control*, 55(3):531–534, 1992.

[66] J Ward MacArthur and Eric W Grald. Unsteady compressible two-phase flow model for predicting cyclic heat pump performance and a comparison with experimental data. *International Journal of refrigeration*, 12(1):29–41, 1989.

[67] C Macnab. Robust associative-memory adaptive control in the presence of persistent oscillations. *Neural Inf Process Lett Rev*, 10:277–287, 2006.

[68] CJB Macnab. Stable neural-adaptive control of activated sludge bioreactors. pages 2869–2874, 2014.

[69] Pedro J Mago, Louay M Chamra, Kalyan Srinivasan, and Chandramohan Somayaji. An examination of regenerative organic rankine cycles using dry fluids. *Applied thermal engineering*, 28(8):998–1007, 2008.

[70] V Maizza and A Maizza. Unconventional working fluids in organic rankine-cycles for waste energy recovery systems. *Applied thermal engineering*, 21(3):381–390, 2001.

[71] Amin Riad Maouche and Mokhtar Attari. Adaptive cerebellar model articulation controller–nonlinear control system for flexible link manipulator. *Journal of Vibration and Control*, 19(14):2109–2123, 2013.

[72] K Masaud and CJB Macnab. Preventing bursting in adaptive control using an introspective neural network algorithm. *Neurocomputing*, 136:300–314, 2014.

[73] Dariusz Mikielewicz and Jarosław Mikielewicz. A thermodynamic criterion for selection of working fluid for subcritical and supercritical domestic micro chp. *Applied Thermal Engineering*, 30(16):2357–2362, 2010.

[74] Jakob Munch Jensen and Hubertus Tummescheit. Moving boundary models for dynamic simulations of two-phase flows. *Modelica'2002 Proceedings*, pages 235–244, 2002.

[75] Jun Nakanishi and Stefan Schaal. Feedback error learning and nonlinear adaptive control. *Neural Networks*, 17(10):1453–1465, 2004.

[76] Antonis Papadourakis, Michael F Doherty, and James M Douglas. Relative gain array for units in plants with recycle. *Industrial & engineering chemistry research*, 26(6):1259–1262, 1987.

[77] PC Parks and J Militzer. A comparison of five algorithms for the training of cmac memories for learning control systems. *Automatica*, 28(5):1027–1035, 1992.

[78] British Petroleum. Bp statistical review of world energy, 2016.

[79] NBOL Pettit, M Willatzen, and L Ploug-Sørensen. A general dynamic simulation model for evaporators and condensers in refrigeration. part i and ii: simulation and control of an evaporator: Modèle général dynamique pour évaporateurs et condenseurs frigorifiques. partie ii: Simulation et régulation d'un évaporateur. *International Journal of Refrigeration*, 21(5):404–414, 1998.

[80] Sylvain Quoilin. Experimental study and modeling of a low temperature rankine cycle for small scale cogeneration. Master's thesis, University of Liege (Belgium), May 2007.

[81] Sylvain Quoilin. *Sustainable Energy Conversion Through the Use of Organic Rankine Cycles for Waste Heat Recovery and Solar Applications*. PhD thesis, University of Liege (Belgium), 2011.

[82] Sylvain Quoilin, Richard Aumann, Andreas Grill, Andreas Schuster, Vincent Lemort, and Hartmut Spliethoff. Dynamic modeling and optimal control strategy of waste heat recovery organic rankine cycles. *Applied Energy*, 88(6):2183–2190, 2011.

[83] Sylvain Quoilin, Vincent Lemort, and Jean Lebrun. Experimental study and modeling of an organic rankine cycle using scroll expander. *Applied energy*, 87(4):1260–1268, 2010.

[84] Sylvain Quoilin, Matthew Orosz, and Vincent Lemort. Modeling and experimental investigation of an organic rankine cycle using scroll expander for small scale solar applications. 2008.

[85] Jovana Radulovic and Nadia I Beleno Castaneda. On the potential of zeotropic mixtures in supercritical orc powered by geothermal energy source. *Energy Conversion and Management*, 88:365–371, 2014.

[86] Bryan P Rasmussen and Andrew G Alleyne. Control-oriented modeling of transcritical vapor compression systems. *Journal of dynamic systems, measurement, and control*, 126(1):54–64, 2004.

[87] Rui Ruivo, Alexandre Paiva, JPB Mota, and Pedro Simões. Dynamic model of a countercurrent packed column operating at high pressure conditions. *The Journal of supercritical fluids*, 32(1):183–192, 2004.

[88] A Schuster, S Karellas, and R Aumann. Efficiency optimization potential in supercritical organic rankine cycles. *Energy*, 35(2):1033–1039, 2010.

[89] R.K. Shah. *Heat Transfer Equipment Design*. Taylor & Francis, 1988.

[90] Jenifer M Shannon. An application of the cerebellar model articulation controller for a switched reluctance rotor position estimator. 1992.

[91] Lin Shi and Sunil K Singh. Decentralized adaptive controller design for large-scale systems with higher order interconnections. *IEEE Transactions on Automatic Control*, 37(8):1106–1118, 1992.

[92] Pedro C Simoes, Joao Fernandes, and Jose Paulo Mota. Dynamic model of a supercritical carbon dioxide heat exchanger. *The Journal of supercritical fluids*, 35(2):167–173, 2005.

[93] Sigurd Skogestad and Ian Postlethwaite. *Multivariable feedback control: analysis and design*, volume 2. Wiley New York, 2007.

[94] Jian Sun and Wenhua Li. Operation optimization of an organic rankine cycle (orc) heat recovery power plant. *Applied Thermal Engineering*, 31(11):2032–2041, 2011.

[95] Sanaz Mahmoodi Takaghaj, CJB Macnab, David Westwick, and Igor Boiko. Neural-adaptive control of waste-to-energy boilers. pages 5367–5373, 2012.

[96] B Fankam Tchanche, G Papadakis, Gr Lambrinos, and A Frangoudakis. Criteria for working fluids selection in low-temperature solar organic rankine cycles. pages 7–10, 2008.

[97] Steve Voss and Greg Gould. The rankine cycle: Workhorse of the coal-fired utility industry, techbriefs. *Burns & McDonnell*, (3):4–6, 2001.

[98] DY Wang, G Pei, J Li, YZ Li, and J Ji. Analysis of working fluid for organic rankine cycle. 1:109–114, 2011.

[99] EH Wang, HG Zhang, BY Fan, MG Ouyang, Y Zhao, and QH Mu. Study of working fluid selection of organic rankine cycle (orc) for engine waste heat recovery. *Energy*, 36(5):3406–3418, 2011.

[100] Jiangfeng Wang, Zhequan Yan, Man Wang, Maoqing Li, and Yiping Dai. Multi-objective optimization of an organic rankine cycle (orc) for low grade waste heat recovery using evolutionary algorithm. *Energy Conversion and Management*, 71:146–158, 2013.

[101] GL Wedekind, BL Bhatt, and BT Beck. A system mean void fraction model for predicting various transient phenomena associated with two-phase evaporating and condensing flows. *International Journal of Multiphase Flow*, 4(1):97–114, 1978.

[102] Donghong Wei, Xuesheng Lu, Zhen Lu, and Jianming Gu. Dynamic modeling and simulation of an organic rankine cycle (orc) system for waste heat recovery. *Applied Thermal Engineering*, 28(10):1216–1224, 2008.

[103] Peter B Whalley. Boiling, condensation, and gas-liquid flow. 1987.

[104] M Willatzen, NBOL Pettit, and L Ploug-Sørensen. A general dynamic simulation model for evaporators and condensers in refrigeration. part i: moving-boundary formulation of two-phase flows with heat exchange: Modèle général dynamique pour évaporateurs et condenseurs frigorifiques. partic i: Formulation des conditions aux limites variables de flux biphasiques avec échange de chaleur. *International Journal of refrigeration*, 21(5):398–403, 1998.

[105] Takahisa Yamamoto, Tomohiko Furuhata, Norio Arai, and Koichi Mori. Design and testing of the organic rankine cycle. *Energy*, 26(3):239–251, 2001.

[106] Jianhua Zhang, Wenfang Zhang, Guolian Hou, and Fang Fang. Dynamic modeling and multivariable control of organic rankine cycles in waste heat utilizing processes. *Computers & Mathematics with Applications*, 64(5):908–921, 2012.

[107] Jianhua Zhang, Yeli Zhou, Ying Li, Guolian Hou, and Fang Fang. Generalized predictive control applied in waste heat recovery power plants. *Applied energy*, 102:320–326, 2013.

[108] Jianhua Zhang, Yeli Zhou, Rui Wang, Jinliang Xu, and Fang Fang. Modeling and constrained multivariable predictive control for orc (organic rankine cycle) based waste heat energy conversion systems. *Energy*, 66:128–138, 2014.